The role of constitutive models on simulating the structural behaviour of masonry arch bridges

Dummy page

The role of constitutive models on simulating the structural behaviour of masonry arch bridges

By

Stijn Marnix Suardus van Breda

In partial fulfilment of the requirements for the degree of

Master of Science

in Civil Engineering

at the Delft University of Technology,

to be defended publicly on 27th October 2023, at 16:00

Supervisor:	W.L. Nobel	Witteveen+Bos
Thesis committee:	Dr. F. Messali	TU Delft
	Prof.dr.ir J.G. Rots	TU Delft
	Dr.ir. W. Broere	TU Delft

An electronic version of this thesis is available at https://repository.tudelft.nl/.

Preface

This report is submitted in partial fulfilment of the requirements for the degree of Master of Science in Civil Engineering, track Structural Engineering, specialisation Concrete Structures at the Technical University of Delft. The work has been performed at the company Witteveen+Bos, to gain more insight in numerical modelling of the structural behaviour of masonry arch bridges. In line with this, the research compares the applicability of different constitutive models that are currently implemented in the commercially available finite element software DIANA FEA.

I would like to thank all the members of my committee, Dr. F. Messali, Prof.dr.ir J.G. Rots, Dr.ir. W. Broere and specially W.L. Nobel who supervised, supported, challenged and encouraged me during the master thesis project. They were always willing to discuss the problems I encountered and help me in solving the problems. Finally, I am deeply grateful to my family, for their unconditioned love in difficult times and their support during my entire study.

Abstract

Masonry arch bridges have been around for centuries and are, in the Netherlands, mostly located in historical city centres. As the axle loads of vehicles passing these bridges have increased over the years, the need to re-evaluate the structural safety of these bridges has increases. To do so, different techniques have been developed. However, assumptions had to be made due to limited computational power and lack of knowledge regarding the actual behaviour of masonry. Over the years, the computational power has increased, making it possible to perform more advanced analysis and describe the behaviour of complex materials. Despite this increase, a conservative approach is still used to determine the safety of masonry arch bridges. When it is not sure whether the bridge is safe enough, the bridge is immediately strengthened or a weight restriction is applied, without calculations of the bridges actual capacity. As these interventions could be costly or cause issues with the supply of goods to the city, it is needed to find a better approach and understanding of the actual behaviour of masonry arch bridges. Therefore this study addresses the following research question:

What is the role of constitutive models on simulating the structural behaviour of masonry arch bridges?

In order to formulate an answer to the question, the behaviour of masonry, masonry arch bridges and soils have been investigated first. The investigation shows which function each part of a masonry arch bridge fulfils and which failure modes are expected to occur. When a masonry arch bridge is loaded, the backfill spreads the load and transfers this to the masonry arch. Due to this load, the arch will deform. This deformation is, however, restricted by the backfill. This interaction between the backfill and the masonry arch makes the behaviour of these types of structures a complex structural-geotechnical problem.

For masonry arch bridges, the most common failure mode is the formation of a four hinge mechanism, therefore this study focusses on modelling the behaviour of the masonry arch. Alongside the behaviour of the materials, the development in numerical tools is investigated as well. Doing so, it can be determined what assumptions have been made in the past and what the shortcomings of the approaches are. With the combined knowledge, it is possible to select different material models that can be used for masonry arch bridges. Three different models were created, two macro models and a micro model. The two macro models are both total-strain based models, where one is described by an isotropic - and one with an anisotropic material model, the so called “Total strain crack” and “Engineering masonry” model, respectively. The macro models consider the masonry as a continuum, whereas the micro model distinguishes between units and joints.

To validate the numerical models, test results are needed. As the study focuses on modelling the masonry arch, the different models are first compared to the results of a test on just a masonry arch. The chosen test was performed at the University of Minho in Portugal; a masonry arch was created and, in a displacement control manner, loaded until failure. Prior to performing the tests, the materials were first tested and their properties accurately reported, which is very useful when making a numerical model. After creating and comparing the results of the models and tests, it was found that the Engineering masonry and micro model show a similar shape of the force-displacement curve, while the isotropic “total strain crack” model does not. The engineering masonry and micro model are able to show the brittle failure of the arch, which was also obtained with the tests. However, this failure occurred when only two hinges were formed, where, in the test, a four hinge mechanism was formed. The numerical results do show that cracks are starting to form, however, this does not mean that it also is a hinge. Besides that, the test results show that there is still some redistribution of forces after the peak load. This is not possible when four hinges are already formed. It is expected that the, by the

researchers defined, hinges are not actually hinges, but, are the points where cracks start to form. Despite this difference in hinge formation, the resulting force-displacement curves of the models are very close to those of the tests, therefore it can be stated that the used models are suitable to represent the behaviour of masonry arches.

After validating the effectiveness of the masonry material models, the modelling of the problem was extended by adding backfill. Again test results were needed to determine whether the models are also suitable to simulate the extended problem. This test was performed at the University of Salford in the United Kingdom and has been used by Wittenveen+Bos to validate other numerical programs in the past. The bridge was tested in a specially designed chamber, in such a way that plain strain conditions hold, and the load was applied at quarter span in a displacement controlled manner. The results were obtained by loading the arch beyond the peak load, with the applied force being reduced while the displacement continued to increase, which was, according to the research, when a four hinge mechanism was formed.

A negative consequence of plain strain conditions is that the engineering masonry material model was not available to be used, therefore only the “total strain crack” model and the micro model were compared. The initial results of the numerical model resulted in local failure of the soil just below the point load, which did not occur in reality. In order to eliminate this local failure, a small area below the load had to be given linear elastic properties. Although this local failure now doesn’t happen, the results still show that plastic strains develop in the backfill, as well as cracks in the masonry arch. A parametric study was conducted to determine the sensitivity of the models to small changes in material properties. This study showed that the models are most sensitive to changes in soil properties, specifically the internal friction angle. For the micro model, it even appeared that only changes in the soil properties affect the behaviour of the structure, meaning that the sliding failure in the backfill is the governing failure mechanism. In the isotropic “total strain crack” model, a lower tensile strength caused the behaviour of the structure to change drastically. It is found that this is due to Poisson’s ratio and the isotropic nature of the material model. The compressive stresses cause small lateral strains which, due to Poisson’s ratio, cause longitudinal strains. Due to the isotropic nature of the material model, a low tensile strength is assigned in this longitudinal direction, causing the arch to form an unrealistic crack or failure pattern. While in reality the tensile strength in this longitudinal direction, the brick tensile strength, is larger compared to the assigned the brick-mortar bond strength.

Eventually, it could be concluded that it is possible to model the behaviour of masonry arch bridges with great detail. However, in this study the behaviour of the backfill governed the behaviour of the structure, making it difficult to state which modelling approach should be used for the masonry arch. What can be said, is that a micro modelling approach is currently preferred. The study shows that this model is capable of mimicking the behaviour of just a masonry arch, and is less sensitive to changes is masonry properties when backfill is added compared to the isotropic “total strain crack” material model. The anisotropic “engineering masonry” model would be a good alternative, but cannot be used in plain strain conditions, yet. Further research is needed to investigate other modelling options, as a three-dimensional model. However, to fully understand the behaviour, more tests are needed. These tests should not only be focussed on the behaviour of the arch, but also on the behaviour of the backfill; and these material properties should be tested and reported extensively.

Table of Contents

List of Figures

List of tables

1. Introduction

In the Netherlands are a lot of masonry arch bridges that were constructed over 100 years ago, of which many are located in historical city centres. Municipalities are obligated to supervise these bridges and if necessary take action. This often includes strengthening of the bridge or restricting heavy vehicles to pass the bridge. These actions are costly or could make the supply of goods to the city centre more difficult. For this reason, a good insight into the behaviour of the masonry bridge is necessary to decide whether the mentioned drastic measures are needed.

The actual bearing capacity of these bridges are often unknown. They were constructed years ago and the design calculations of them are lost or not even made. By performing tests on redundant bridges, more knowledge is gained on the behaviour and bearing capacity of the bridges. As a large portion of road and railway systems in the United Kingdom (UK) consists of masonry arch bridges, most data concerning the destructive tests is obtained here.

By using finite element analysis (FEA) a prediction of the capacity could be made, but the models can be very large, time consuming and therefore computationally very expensive. The models can even be too large to be calculated at all, to this end simplifications have been made to reduce the computational power needed and still get some information. These simplifications could however lead to unreliable results and unnecessary actions by municipalities. During the past years computational power increased a lot, making it possible to analyse models without simplifications. This could lead to a better representation of actual structure and materials.

1.1. Problem statement

In the coming years many masonry arch bridges in The Netherlands have to be evaluated and, if necessary, be strengthened or even replaced. The actual ultimate limit state (ULS) load can only be found by performing a destructive test. This is unwanted because then a new bridge has to be constructed, while the safety evaluation of the existing bridge was the goal. Using finite element analysis, the behaviour in both ULS and serviceability limit state (SLS) of bridges can be approximated.

The Dutch company Witteveen+Bos (W+B), among others, was asked by the municipality of Den Bosch to evaluate the safety of forty bridges in the city centre. To do so they made models in multiple finite element programs, these programs were LimitState Ring, Plaxis and SCIA Engineer. Prior to analysing the bridges in Den Bosch, the finite element programs were compared and validated making use of laboratory tests. The main focus was on the maximum bearing capacity of the bridges, the ultimate limit state (ULS), as this is eventually the point of interest for the bridges. The investigation showed that SCIA Engineer was not able to model the behaviour of the masonry arch bridges.

Predictions regarding the safety of the masonry arch bridges in Den Bosch could now be made, making use of LimitState Ring and Plaxis. To be able to check whether these predictions are realistic, data regarding the actual behaviour of the bridge is needed. Therefore, a non-destructive test was performed on one of the bridges. LimitState Ring is a program that only reports the bearing capacity of the bridge, meaning that the results cannot be compared to those obtained in the non-destructive test. Plaxis is a program that is mainly used by geotechnical engineers, it has many options to model soil behaviour, but has less options to model for instance masonry. A Comparison of the result for the Plaxis model and the test results showed that the displacements of the abutments were different, while the displacements of the crown were similar.

Differences between model and reality can have consequences regarding the safety evaluation, a bridge can be considered “safe”, while it isn’t, or “not safe”, while it is. Both scenarios are not wanted, as they could result in accidents or unnecessary improvements. The difference between the Plaxis model and the test can be caused by various assumptions made by the engineer. In this case, a macro modelling technique was used and the masonry was assumed to be homogeneous isotropic. The impact of these choices has not been investigated into depth. Next to that, Plaxis is mainly used for geotechnical applications, whereas DIANA FEA is a program mainly used by structural engineers. This program has more options to represent the behaviour of masonry. To be able to make a detailed representation of the behaviour of masonry arch bridges, more knowledge regarding the impact of these choices is therefore needed.

1.2. Objective

The main goal if this study is to investigate how the behaviour of masonry arch bridges should be modelled. To this end it is important to investigate the impact of different modelling techniques on the accuracy of the numerical simulation. This study focuses on the masonry arch, by investigating differences between isotropic and an-isotropic material models. Next to that, the difference between macro- and micro models will be investigated also. To be able to investigate this, it is important to find representative tests that could count as benchmarks.

In order to determine what impact these different choices have on the accuracy of the masonry arch bridge as a whole, a number of steps are required.

As the main focus of this study is on modelling the masonry, it is first needed to simplify the masonry arch bridge. To this end the behaviour of just a masonry arch will be investigated, by creating and comparing three distinct models. The first two models will follow a macro modelling technique, where one makes use of isotropic elements and one uses anisotropic elements. The third model will be a micro model in which all bricks and joints will be modelled as individual elements. After the models are compared and validated to test results, the problem will be extended. Adding backfill to the arch will increase the complexity of the problem, due to added the influence of soil-structure interaction and soil behaviour. Again the three models will be created and validated to a benchmark test.

1.3. Research questions

In order to achieve this objective, the following main research question is formulated:

What is the role of constitutive models on simulating the structural behaviour of masonry arch bridges?

This question is answered by making use of the following sub questions:

- *SQ1. Can the constitutive models, implemented in a commercial finite element analysis software, accurately simulate the behaviour of an isolated masonry arch?*
- *SQ2. Does the accuracy change when backfill is added to the model?*
- *SQ3. What is the impact of isotropy on the model accuracy?*
- *SQ4. How much accuracy is added when a micro modelling technique is used?*
- *SQ5. Which modelling approach has to be used for masonry arch bridges?*

2. Review of the literature

This chapter provides a wide range of literature review and is needed to have a basic understanding of the behaviour masonry arch bridges. First a general description of masonry in general will be given to understand the failure modes on micro scale. Next, the different components of a masonry arch bridge will be brought to light explaining their function in the structure. Finally, different modelling techniques and available material models will be discussed.

2.1. Masonry general

The building material masonry has been used in construction for a long time. It is a combination of a stone like material that is “glued” together using a mortar. Historically masonry was constructed with natural stones and mortar, however due to the different shapes and sizes of the stones people felt the urge to develop a building material with similar shapes and sizes. This led to the invention of clay bricks, making masonry construction more homogeneous and faster. What the developers did not realise at that time, that it was now possible to do calculations regarding the strength of the masonry construction. In the following sections the general mechanical properties of masonry will be described.

2.1.1. Mechanical properties of unit and mortar

The mechanical properties of the unit and mortar determine the mechanical properties of the masonry. Many researchers have tried to find the strength, stiffness and deformation capacity of masonry by performing various tests. The researchers McNary and Abrams developed in 1985 a relatively simple theory to represent the mechanics of clay-unit masonry in compression. The response of a stack of bricks bonded with mortar was investigated (Figure 2.1). It was found that the mortar expands laterally more than the brick, causing shear stresses in the unit-mortar interface. In the bricks bilateral tension and in the mortar layer a triaxial compression was found. Based on these findings, it was decided to perform biaxial tests of bricks, triaxial compressions tests of mortar and uniaxial compression tests of stack-bond prisms.

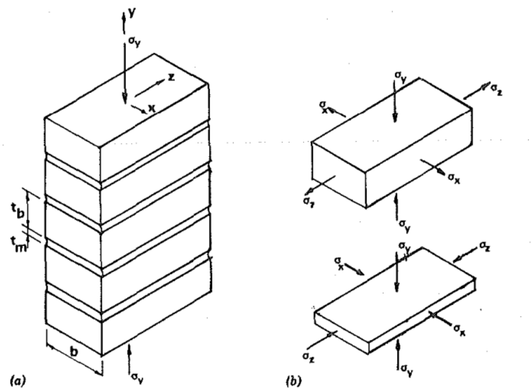

Figure 2.1: (a) Prism subjected to compression; (b) Stress states for brick and mortar (McNary & Abrams, 1985)

The results of the tests showed that the stress-strain behaviour of the mortar had a non-linear shape. Next to that, the tests of the bricks subjected to lateral tension and axial compression showed that the relation between the compressive strength and the biaxial tension stress could be best described as:

$$\frac{C}{f_b} = 1 - (\frac{T}{f_{bt}})^{0.58} \qquad 2.1$$

In which C is the compressive stress in the brick, f_b the uniaxial compressive strength, T the tensile stress in the brick and f_{bt} the direct tensile strength of the brick (McNary & Abrams, 1985).

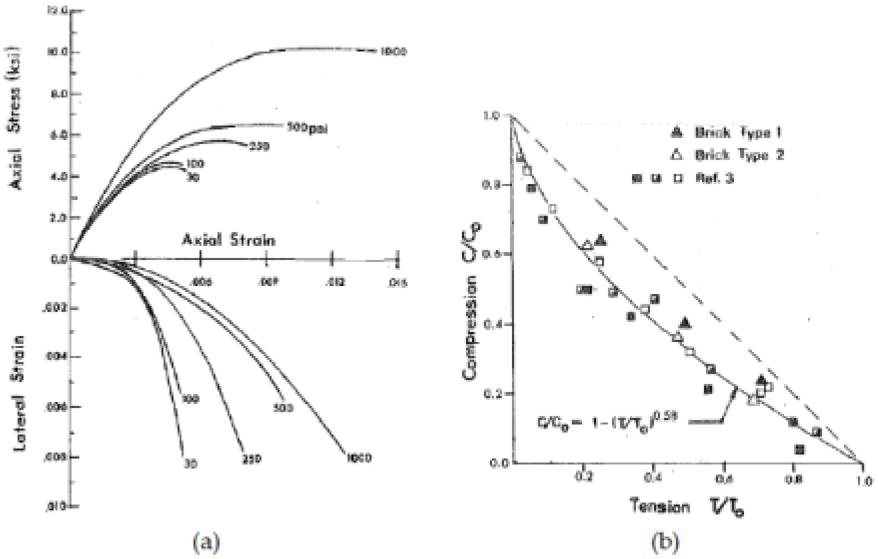

Figure 2.2: (a) Measured properties of mortar under different confining stress; (b) Biaxial interaction diagram for bricks (McNary & Abrams, 1985)

2.1.2. Failure modes

The weakest part in masonry is located at the unit-mortar interface. Understanding the bond between the units and mortar is therefore important to understand the behaviour of the masonry. As mentioned before, the non-linear response of the joints, controlled by the unit-mortar interface, is one of the driving factors in masonry behaviour. At the interface two different failure modes are observed, one related to tension normal to the interface (Mode I: Opening) and one related to shear along the interface (Mode II: In-plane shear) (Loarenço, 1996).

2.1.2.1. Mode I: Opening

Mode I failure is determined by the tensile strength of the joint. The chemical bond between the unit and mortar controls the tensile strength of the bond. The energy needed to break the bond and create a unitary area of a crack along the interface is called the Mode I fracture energy, G_f^I. In 1992, Van der Pluijm carried out a series of tests and found that the relation between the tensile bond strength and crack width had a exponential nature (Pluijm, 1992). Next to that, the observed fracture energies were low, ranging from 0.005 to 0.02 MPa for tensile bond strengths between 0.3 to 0.9 MPa (Loarenço, 1996).

Another important result was found by analysing the cracked specimens. It was observed that the bond area was smaller than the cross sectional area. The bond area was concentrated in the inner part of the cross section and was on average only 35% of the initial cross section.

2.1.2.2. Mode II: In-plane shear

Mode II failure is determined by the shear strength of the joint. This shear strength is achieved by both the chemical bond and the friction between the unit and mortar surfaces. Experiments showed an exponential shear softening diagram with a residual dry friction level (Pluijm, 1993). The area defined by the stress-displacement diagram and the residual dry friction is called the Mode II fracture energy, G_f^{II}. The value of this fracture energy is highly dependent on the confining, compressive, stress. The relation between the confining stress, peak strength and residual dry friction can be obtained using the Mohr-Coulomb friction model. This model describes the material parameters as the initial internal friction angle ϕ_0, the initial cohesion c and the residual internal friction angle ϕ_r. After reaching the peak strength the cohesion disappears, causing the residual dry friction to be only influenced by the residual internal friction angle.

2.2. Masonry arch bridges

2.2.1. Arch bridge history

It is believed that the oldest arch bridge is located in Greece and was built between 1300-1190 BC. So human kind have been constructing these arch bridges for over 3000 years. During this period people have been investigating these structures in order to gain more knowledge about the arches and the mechanics behind it. Nowadays there are still some unknowns in the assessment and evaluation of arch bridges. As mankind gained more knowledge about different materials, the materials used in arch bridges can also be different. Starting from only large stones to the point where combinations of different materials are used. Masonry is one of the most widely used materials in current historical arch bridges and is therefore considered in this thesis.

2.2.2. Arch bridge geometry and components

Arch bridges can be very complex and fulfil various functions, but can basically be divided into two main categories: Single span - and Multi span bridges. Single span arch bridges have, as mentioned in the name, only one arch barrel, whereas multi-span bridges contain more arch barrels. It can be expected that single-span arch bridges are less complex than the multi span bridges. Understanding the behaviour of a single span bridge is therefore needed to understand multi span arches.

Before going into depth, it has to be known what the different components are in a masonry arch bridge and what their function is within the structure. In Figure 2.3 the basic components of an arch bridge are shown. Simplified it consists of an arch spanning between two abutments, backfilled with a material that is held in place by spandrel walls.

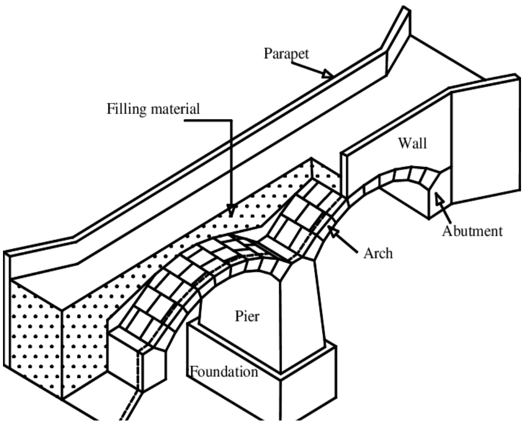

Figure 2.3: Arch bridge components (Rota, Bolognini, Pecker, & Pinho, 2005)

2.2.2.1. The arch

It is clear that the arch transfers the load acting on the bridge deck to the abutments. With this in mind, the design of the arch is the starting point for these type of bridges. As almost every arch has to overcome a different span or fulfil a different function, various shapes of the arch itself have been constructed. In Figure 2.4 the three main groups are shown: Parabolic, semi-circular and segmental.

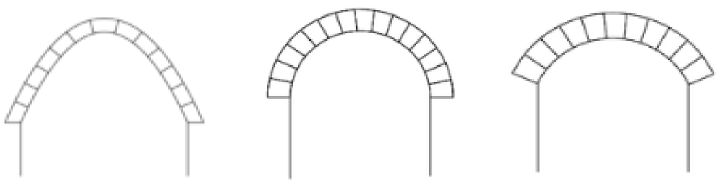

Figure 2.4: Possible arch shapes

2.2.2.2. Masonry arch

Historically, arches were build using large natural stones an rocks, as this was the only available building material. Due to increasing knowledge about materials and the invention of clay bricks, more different materials were used to construct arches. As most historical arch bridges in The Netherlands are masonry arch bridges, this will be the focus of this thesis.

Next to the shape of the arch, there are also different ways to build up the masonry arch ring itself. Different patterns exist in masonry and are shown in the figure below, starting with the single-ring voussoir arch, followed by the header-bonded arch and the multi-ring arch (Ahmad, 2017).

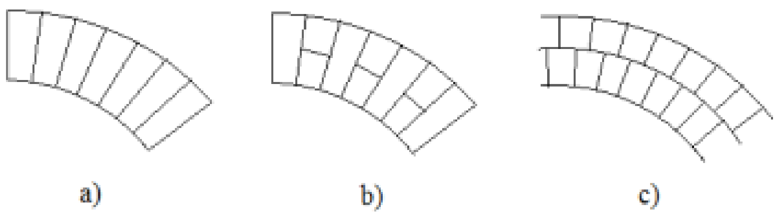

Figure 2.5: Execution of masonry; a) Single-ring voussoir arch; b) Header-bonded arch; c) Multi-ring arch (Ahmad, 2017)

These different configurations also have different properties. With the multi-ring arch (from c) for instance a thicker arch could be constructed. Although the thrust line now has a wide range, it might be possible for the rings to separate due to shear or loss of cohesion. This is caused by the constant mortar layer between the two rings. For the header-bonded arch (from b) this layer does not exist and therefore behaves more as a single-ring arch. The header-bonded arch also provides interlocking in the transverse direction, across the width of the bridge, making it a more stable configuration compared to the single-ring voussoir arch (from a) (Casas, 2011).

2.2.2.3. Abutments

The abutments of the arch bridge are supporting the arch and distribute the loads to the subsoil. As these parts are mostly made from reinforced concrete, the compressive strength of the abutments is greater then the arch. The biggest problem regarding the abutments is horizontal translation, this can cause the bridge to fail. The amount of translation is depending on the subsoil that is present at the site of the bridge, this can be very different for all bridges.

2.2.2.4. Backfill material

Fill material has an important function in the stability of the bridge system, it adds dead weight to the masonry arch, creates a smooth surface and spreads live loads. As known from geotechnical studies, all types of soil behave differently and are therefore distributing loads and deforming differently. Next to the difference in soil type behaviour, within these soil types there are also differences. For instance, the response to an arbitrary load will be different for a compacted soil to a loose soil. As the behaviour of soil is quite complex and important for the stability of the system, extra attention will be paid to this behaviour in section 2.3.

2.2.2.5. Spandrel walls

In order for the backfill material to be in place, there needs to be something keeping it in place. For masonry arch bridges this is done using spandrel walls. The walls do not carry loads to the subsoil but are stabilizing the system as a whole. In this thesis only two dimensional models will be made and the influence of these walls will be disregarded.

2.2.3. The flow of forces

Arches can have various shapes, as shown in Figure 2.4 . However, regardless of the shape of the arch, the arch transfers the forces in the same manner using compression. Taking for instance the parabolic arch, the idea behind this mechanism was found by Robert Hooke (1635-1703). He described the relationship between a hanging chain and an arch, by inverting the chain a perfect compressive arch was created (Hooke, 1676). Later others expanded this concept to be used in equilibrium analysis and came up with the “line of thrust”, this line represents the resultants of compressive forces through the arch. The idea behind this was, for a compressive structure to be in equilibrium with the applied loads, there must be a line of trust that lies completely within the cross section (Heyman, 1966). In other words, if the thrust line is outside the cross section, the structure will collapse and hinges will be formed where the line hits the boundaries of this section. A simplified representation of this mechanism is shown in Figure 2.6.

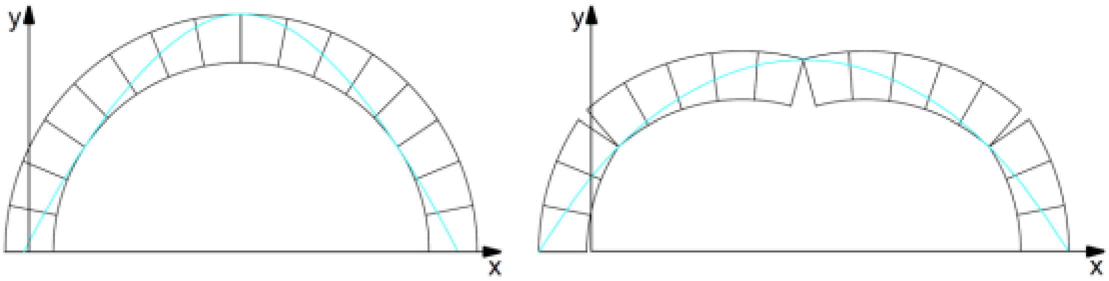

Figure 2.6: Line of thrust for hinge formation (Zampieri, Cavalagli, Gusella, & Pellegrino, 2018)

As mentioned in section 2.2.2.4, the backfill also has an influence on the stability of the structure. When the live load is present on the bridge, the load is spread by the backfill. The width of this spread depends on the type of backfill material used. The load causes the arch to deform, but due to the backfill the arch is not free to deform. The backfill provides this horizontal stability, which is called passive restraint (Callaway, Gilbert, & Smith, 2012). In Figure 2.7 the forces on the arch, caused by the spread and passive restraint are shown.

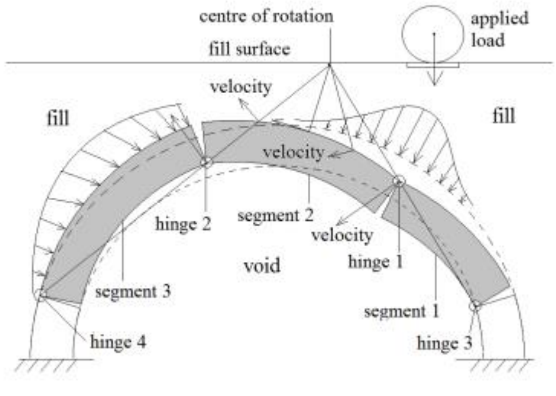

Figure 2.7: Flow of forces and deformed shape for a four hinge mechanism (Ahmad, 2017)

2.2.4. Failure modes

Low tensile - and shear strength between masonry and mortar is what causes masonry arch bridges to fail. For single-span arches, a four-hinge mechanism is (usually) the critical failure mechanism, this can also be seen in Figure 2.7. Flexural cracks are formed at the locations of the hinges, when these become large enough, the system will fail (Pippard & Ashby, 1939).

Other failure modes that could occur are shear failure, compressive failure and ring separation. The first two modes are not likely to occur as the critical loads are above those of the hinge mechanism. Shear failure, sliding, is not expected when the bridge is loaded by live load on the bridge deck, but can occur due to seismic loads. These loads act horizontally on the structure and could cause mortar joints to open, making it possible for the bricks slide downwards.

Ring separation and crushing are failures mode that could happen due to live loads. However, in this study only single-ring masonry arches are considered, making ring separation not possible to occur. Since no building material is incompressible, crushing can always occur. In most cases crushing of mortar will happen at the locations of the hinge, but the overall failure mechanism still remains a four-hinge mechanism.

2.3. Soil behaviour

Soil is a material that behaves non-linearly and shows anisotropic and times dependant behaviour when subjected to stresses. In the past many researches have tried to construct constitutive models to capture the behaviour. Before going into depth on these models, some aspects influencing the soil behaviour are explained first after which some constitutive models will be explained.

2.3.1. Aspects of soil behaviour

The real behaviour of a soil is characterized by various aspects, one of which is the influence of water. Total stresses in the soil can be divided into effective stresses and pore pressures. The mechanical behaviour of the soil is determined by the effective stresses, making it very important to know the pore pressure distribution next to the total stress state. A change in pore pressure distribution, without a change in external loading, causes a change in effective stiffness and therefore influences the deformations.

An other aspect is the fact that the soil stiffness is not a constant. The stiffness is influenced by the stress level, stress path, strain level, time, density, permeability, over-consolidation and the directions. A higher stiffness is found for a larger confining stress, smaller strain level, more dense soil, undrained saturated soil or over-consolidated soil. On the other hand, smaller stiffnesses are found when the shear stress level is higher.

The third aspect relates to irreversible deformations due to loading. Most soils only have a small elastic region, causing irreversible deformation almost from the offset of loading. This is one of the main aspects that makes modelling of soils more complex.

Soil strength is also an important aspect, which is usually expressed in terms of shear strength. Due to the nature of soil, a frictional material, the shear strength depends on the confining effective stress level. Next to that, the shear strength is also influenced by the loading speed, time, density, undrained behaviour and over-consolidation. Next to the shear strength, most soils show hardly any or even no tensile strength at all.

A fifth aspect relates to the time-dependency of soil behaviour. Next to the above mentioned influence on stiffness and strength, time can also play a role when the loading conditions remain unchanged. These time dependent phenomena are also know as creep, relaxation and swelling (Brinkgreve, 2005).

2.3.2. Mohr-Coulomb model

The Mohr-Coulomb model is often used to model the behaviour of soil in general. It is an elastic perfectly-plastic model which is formed by combining Hooke’s law and the generalized form of coulomb’s failure criterion. The model is capable of representing the failure behaviour, but the stiffness behaviour before reaching the local shear strength is poorly modelled. According to Hooke’s law, the stiffness behaviour below the failure contour is assumed to be linear elastic, reducing the accuracy of the model to predict the deformation behaviour before failure. However, due to the simplicity of the model, it could be used to get a first estimate of deformations as order of magnitude (Brinkgreve, 2005).

Contrary to the stiffness, the model preforms better regarding the strength behaviour. The hexagonal shape of the Mohr-Coulomb failure contour, Figure 2.8 , was proven to be quite accurate (Goldscheider, 1984). This makes the model suitable to analyse the stability of geotechnical structures as dams, slopes, embankments, etc..

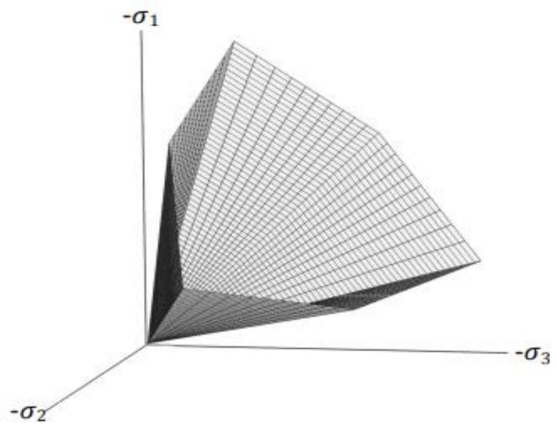

Figure 2.8: Mohr-Coulomb failure contour (Brinkgreve, 2005)

The Mohr-Coulomb model has some limitations, as it assumes that the material is homogeneous and isotropic, and it does not take into account the effect of particle size distribution, particle shape, and other factors that can affect the behaviour of granular materials. Nonetheless, it remains a useful tool for modelling the behaviour of soils and rocks in many engineering applications.

2.3.3. The Hardening soil model

The hardening soil model, also known as the modified Mohr-Coulomb model, is a second order model that can be used for any type of application (Brinkgreve, 2005). It is based on elastoplastic formulation and can capture the basic properties of soil materials, such as the pressure dependant shear strength, irrecoverable compaction and nonlinear elastic unloading. In contrast to the Mohr-Coulomb model, the yield surface is not fixed but can expand due to plastic straining.

The model involves two types of hardening, shear hardening to model the plastic shear strain in deviatoric loading and compressive hardening to model the plastic volumetric strain in primary compression. Due to these types of hardening, the model is accurate for problems involving a reduction of mean effective stress and at the same time mobilisation of shear strength.

The stiffness behaviour is modelled using a power law formulation for the stress-dependent stiffness. When simulating a standard drained triaxial test, the relationship between the axial strain and the deviatoric stress can be approximated by a hyperbola. This relationship was first described by Duncan and Chang (1970) and formed the basis of the hyperbolic model (Duncan & Chang, 1970). Although the same hyperbola is used in both models, the hardening soil model describes the stiffness behaviour more accurately. This is due to the fact that the theory of plasticity is used instead of the theory of elasticity. Next to that, the HSM includes dilatancy and a yield cap.

Failure is defined by means of the Mohr-Coulomb failure criterion, but now modified to include the shear hardening and the yield cap. The yield contour for this model is shown in Figure 2.9.

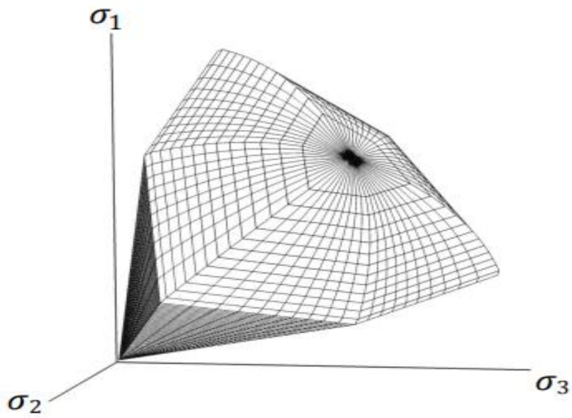

Figure 2.9: Hardening Soil Model Yield contour (Brinkgreve, 2005)

Just as for the Mohr-Coulomb model, the HSM also has some limitations. One of the main limitations is the complexity of the model, as it makes use of many parameters that need to be found using laboratory tests. The tests are well known and do not form a problem, however, for older problems, these tests are most of the times absent and assumptions need to be made. Next to the complexity, the model does not account for anisotropic behaviour or strain rate effects (Schanz, Vermeer, & Bonnier, 1999).

2.4. Modelling approaches for masonry arch bridges

Modelling masonry arch bridges requires insight into the different components and materials and their interaction with each other. Due to the nature of the materials, non-linear and anisotropic, it has taken a lot of effort to formulate methods to predict the bearing capacity of the bridges. Next to this effort, the increase in computational power made it possible to model the behaviour of structures with even more precision. This resulted in three main methods for the evaluation of masonry arch bridges, semi-empirical models, equilibrium-based models and numerical models.

2.4.1. Semi-empirical models

The most known semi-empirical method was found by the Military Engineering Experimental Establishment and is better known as the MEXE method. This method is based on the elastic theory and makes use of assumptions, concerning the shape and materials, to be able to perform the analysis. For instance, the arch has to be parabolic and have a span-to-rise ratio of 4, which already eliminates the use of this method for bridges that do not meet the requirements. Next to this, the method can only predict the bearing capacity and not the deflections.

2.4.2. Equilibrium-based models

Equilibrium based models make use of a limit state analysis method and assume that the structure is near total collapse. In this limit state four hinges are formed in the arch, making it a mechanism that is statically determined. Using static equilibrium equations the forces on the abutments are then calculated resulting in the bearing capacity. The assumptions in this method are that the arch has no tensile strength, infinite compressive strength and that sliding cannot occur. Using this as basis, a rigid block model was developed, applying the upper-bound theorem of the theory of plasticity to determine the collapse load. With linear programming techniques this solution procedure is implemented in LimitState: Ring. But again the method only reports the bearing capacity.

2.4.3. Numerical models

Using numerical methods a more detailed description of the behaviour of masonry arch bridges could be obtained. The finite element method (FEM) is a complex method, which uses incremental solution schemes and is able to take into account non-linearity. There are multiple FE software packages available, but developed for different purposes. The most known are LimitState Ring, Plaxis and DIANA. Choosing a program depends on the goal of the research. With LimitState Ring, the bearing capacity, ultimate limit state (ULS), and failure mechanism could be obtained but the behaviour of the arch before failure, serviceability limit state (SLS), is not possible to analyse (LimitState, 2020). Plaxis and DIANA could both model the behaviour before failure, SLS, and the bearing capacity, ULS, but have a different field of application. In Plaxis there a more possibilities in modelling the soil-structure behaviour, whereas in DIANA there are more options in modelling the masonry. In this paper use will be made of the program DIANA, since the point of interest is modelling the masonry and it is assumed that the program contains enough capacity to model the behaviour of the soil.

Within finite element modelling there are different options in modelling the structure. It is possible to model every component of the bridge with great precision, but these models can grow too large to even be evaluated at all. To this end simplifications have been adopted in order to reduce the computational power needed and still get some insight into the behaviour. One of these simplifications is the use of a macro modelling approach rather than a micro modelling approach. Figure 2.10 shows the differences between the approaches (Lourenço, Rots, & Blaauwendraad, 1995).

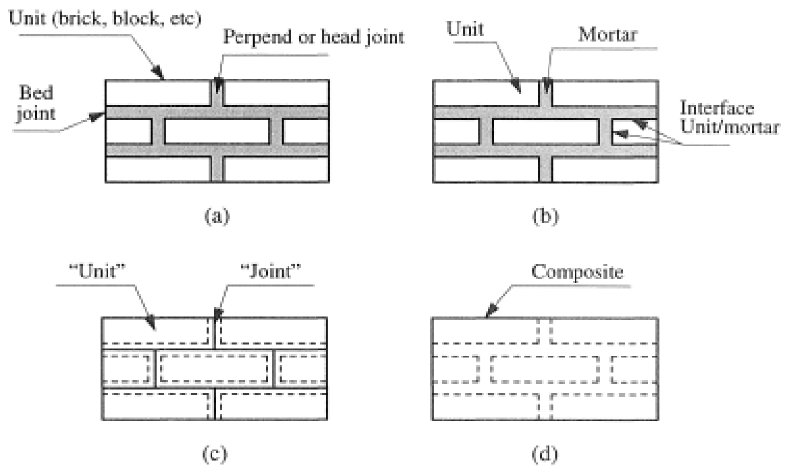

Figure 2.10: Modelling strategies for masonry structures: (a) Masonry sample; (b) Detailed micro-modelling; (c) Simplified micro modelling; (d) Macro-modelling (Lourenço et al., 1995)

2.4.3.1. Micro modelling

Micro models are models where the bricks, joints and imperfections of the masonry are modelled separately. The bricks and the mortar are modelled with continuum elements and there interaction with each other is modelled using discontinuous elements. The Young's modulus, Poisson's ratio and inelastic properties are taken into account for both brick and mortar separately. The discontinuous elements represent the potential crack or slip plane with an initial dummy stiffness. This makes it possible to study the behaviour of masonry with great precision. However, the computers need a large storage capacity and power. When bigger structures are analysed, it could very well be that the computer is not capable of doing so or that it will take a lot of time.

The interface elements allow discontinuities in the displacement field, their behaviour is described in terms of the relation between the tractions and relative displacement across the interface. When the normal traction exceeds the tensile bond strength, a crack will be formed and the element stiffness changes. For masonry, softening models are used to ensure that the shear and tensile stresses decrease gradually as the crack opening is increasing, instead of dropping to zero instantly.

2.4.3.2. Marco modelling

As mentioned before, macro models reduce the computational power needed to calculate the models. In these type of models, the bricks, joints and imperfections are smeared over the geometry of the bridge. Macro models are handy for quick calculations, however these type of models cannot report crack widths and do not account for the actual execution of the brickwork. This can be a cause for differences between model and reality, making their results not reliable.

To be able to calculate the model, the element needs to be given properties. This is done by selecting a material model and testing parts of the masonry. What material model needs to be used, depends on the material that is investigated. However, in current practice masonry is modelled using a concrete material model that is adapted to masonry properties. It sounds reasonable, however masonry and concrete are fundamentally different. Concrete is isotropic and masonry is anisotropic, meaning that concrete has the same stiffness in all directions and masonry does not. This can also be a cause for differences between the model and reality. The program DIANA FEA offers also a material model for masonry, in this study the concrete model and the engineering masonry model will be investigated.

3. Adopted modelling approach

3.1. Modelling basics

Finite element programs can help in analysing difficult physical problems, they are capable of performing complex calculations to provide insight in the behaviour of the structure. To be able to get reliable results, the programmer needs to make a well justified idealization of the physical problem that can be put into the program. When this idealization isn't accurate, the program will still give results, but don't say anything about the physical problem. In other words, the program does not find idealization errors and is just as good as the programmers input.

In general the programmer needs to idealize the physical problem to a mechanical model, after which the mechanical model has to be discretized to a finite element model. The program can now calculate the problem and give results. These result now still need to be checked by the programmer by answering questions as: "Are the results in line with the expectations? Do they match test results? What could be the cause for differences? Etc."

Finite elements can be visualised as a small piece of a structure, for which the relationship between displacements, strains, stress and forces is known. In each finite element a field quantity, displacements, can only have a simple spatial variability. In the nodes of an element, the solution for the displacement field gives exact values. In between the nodes, the displacements are approximated using an interpolation function and depend only on the displacements of the nodes. This function can have two shapes, linear and quadratic, shown in Figure 3.1 (Esposito, Hendriks, & Rots, 2022)[1].

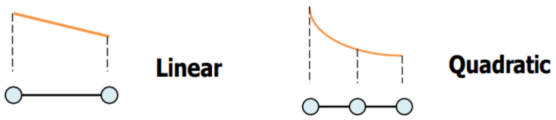

Figure 3.1: Basic interpolation functions (Esposito et al., 2022)[1]

A finite element has nodes and integration points (IPs). As mentioned the displacements are exact in the nodes. In the IPs the strains are calculated by interpolation and differentiation from the nodes to the IPs. By assigning a material and defining the constitutive law, the stresses can now be calculated in the IPs. After integration of these stresses, the internal forces are calculated in the nodes. Using these forces it can now be checked whether equilibrium is achieved with connected elements and/or external forces (Esposito et al., 2022)[1]. Summarizing the displacements and internal forces are evaluated in the nodes and the strains and stresses in the IPs.

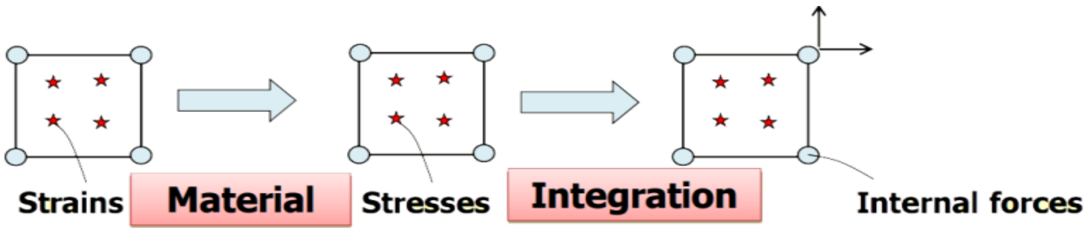

Figure 3.2: Basic element description (Esposito et al., 2022)[1]

Considering problems in structural mechanics, the main unknowns are displacements and rotations. These unknowns are called degrees of freedom (DOFs) and govern the spatial variation of the field. DIANA offers a big variety of elements that can be used for different purposes. In order to make select element it is therefore important to know what type of model can be built with what element, what assumptions are made for the displacement, stress and strain field, and what DOFs does the element have.

[1] Source from Brightspace TUD (not publicly accessible).

3.2. Nonlinear modelling

Finite element programs are capable of performing non-linear analysis by performing an iterative solutions procedure to find equilibrium. As mentioned, the initial solution is obtained by guessing a displacement field at the nodes, calculating the strain and stress in the IPs and integrating these to find the internal forces, after which it is checked whether equilibrium is achieved. When this is not the case, a different displacement field is assumed and the solutions procedure is repeated over and over until equilibrium is achieved (Esposito et al., 2022)[2].

3.2.1. Sources of nonlinearity

There are three distinct sources that can cause nonlinearity, material -, geometric - and contact nonlinearity. Material nonlinearity is considered when the material properties are functions of the state of stress or strain, deformation history, time, temperature, maturity, etc.. For instance nonlinear elasticity and plasticity are material nonlinearities, shown in Figure 3.3.

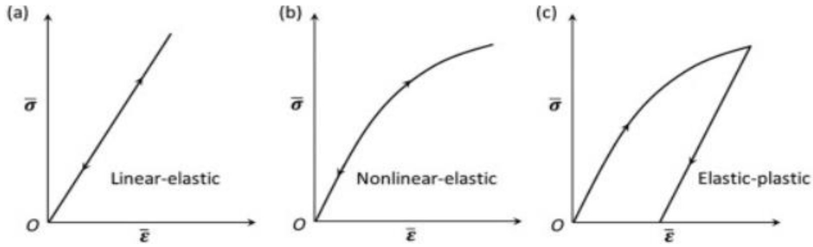

Figure 3.3: Nonlinear elasticity and plasticity (Esposito et al., 2022)[2]

Geometric nonlinearity is considered when the deformations of the structure/element is large enough, so that the equilibrium equations have to be written with respect to the deformed structural geometry. Due to the deformed shape, the loads may change direction or magnitude. This phenomenon could occur when analysing for instance slender structures or tensile structures as cables.

The last source of nonlinearity is contact nonlinearity, which describes the relationship between two elements. For instance, gaps that open or close, a change in contact area or possible sliding with frictional forces. However, in practice, many contact problems could be simplified by using interface elements with no-tension behaviour (material nonlinearity).

3.2.2. Equilibrium path

The response of a nonlinear physical problem can be characterized by a so called equilibrium path. This path is a graphical representation of the load-displacement curve which characterized the overall behaviour of the problem. Each point on the path represents an equilibrium point or configuration. The unstressed and undeformed configuration from which the loads and deflections are measured is called the reference state. The path connecting the reference state and the critical point is called the fundamental path, the behaviour of the structure after this critical point is called the secondary path (Figure 3.4). The equilibrium path is found in an incremental-iterative solution procedure, the load is applied in small steps (increments), for every step an iterative procedure is followed to balance the external and internal forces (Figure 3.4).

[2] Source from Brightspace TUD (not publicly accessible).

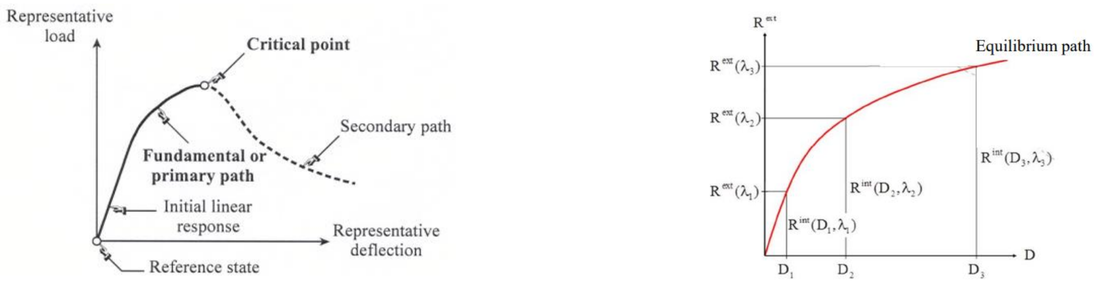

Figure 3.4: Equilibrium path and path finding (Esposito et al., 2022)[3]

Multiple choices can be made concerning the iterative solution procedure, starting with the solution procedure itself. The most common used solution procedure is the Full Newton-Raphson method, shown in Figure 3.5. For every increment and iteration, this solution procedure updates the stiffness matrix. This requires a large amount of computational power but, reduces the amount of iterations. It can also be chosen to use the modified Newton-Rapson method or the initial stiffness method, where the stiffness matrix is only updated in the first iteration of every load increment or the initial stiffness is used for every iteration respectively. These last two methods might use over stiff matrices which will lead to more iterations. However, the total analysis time might still be shorter, due to the less computational power needed to update the stiffness matrices (Esposito et al., 2022)[3]. The three solution methods are shown in Figure 3.5 below.

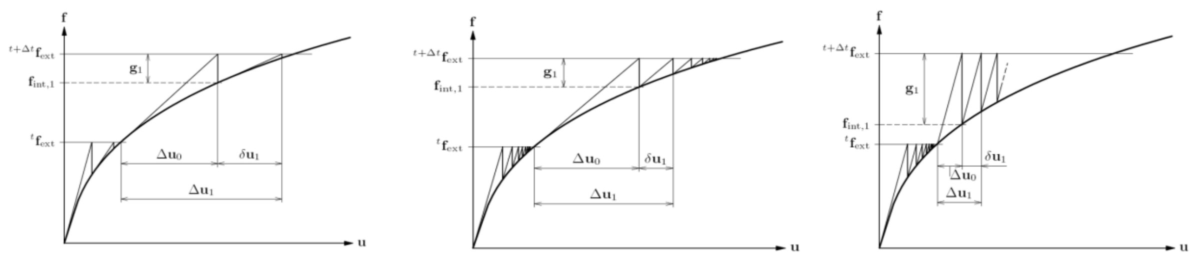

Figure 3.5: Iterative solution procedures, Full Newton-Raphson, Modified Newton-Raphson and Initial stiffness (Esposito et al., 2022)[3]

The iterative procedure continues to the next load step once convergence is reached in the previous step. In order to reach convergence, some criteria have to be defined that measure how well the obtained solution satisfies the equilibrium. There are three different convergence norms that can be used, force-based, displacement-based and energy based norms. The force based convergence norm is puts a restriction on the force imbalance that is allowed. For the displacement based convergence norm describes how big the last update of the displacement increment may be, compared to the initial displacement increment. In the energy-based convergence norm, the last update of the stored energy is a small fraction of the initial stored energy. This actually is a combination of the force and displacement norm. When convergence criteria and tolerances are chosen to be too loose, inaccurate results are obtained. On the other hand, when they are set to be too tight, this could lead to time consuming analysis and unnecessary accuracy. For non-linear finite element analysis, a combination of multiple convergence norms is usually set (Esposito et al., 2022)[3].

3.2.3. Loading conditions

Next to the solution method an convergence criteria, it is also important to think about the information you want to find and how to find this. The load can be applied to the structure in two different manners, force controlled and displacement controlled. Both manners are straight forward, either increasing the load in small steps, or increasing the displacement in small steps. Force controlled

[3] Source from Brightspace TUD (not publicly accessible).

analysis can only construct the fundamental equilibrium path, after the limit point is reached, it is not possible to find an equilibrium with greater forces (Figure 3.6). In the displacement controlled analysis, this point limit point can be passed, making it able to construct the secondary equilibrium path. However, displacement controlled analysis cannot overcome turning points (Figure 3.6).

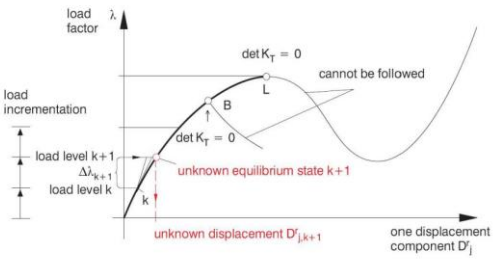

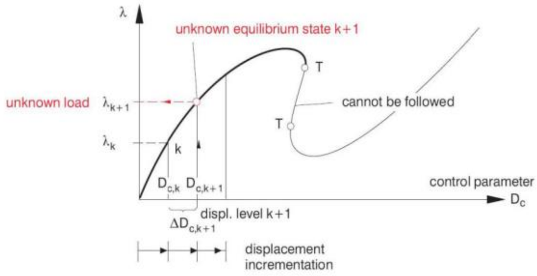

Figure 3.6: Loading conditions, force controlled ; displacement controlled (Esposito et al., 2022)[4]

3.3. Finite elements

As mentioned before, there are many element types available in DIANA FEA. Selecting appropriate elements is very important to capture the properties of the physical problem and its behaviour. The programmer first need to think about the shape - and topological dimensions. The choices that can be made regarding shape dimensions are: 0D for a point mass, 1D for a straight line, 2D for a flat shell or 3D for a wedge, curved shell or double curved line. Topological dimensions relate to a point mass in 0D, a straight or curved line in 1D, quadrilateral or triangular in 2D and brick or wedge in 3D. Next to these choices, thought has to be put into the assumptions that are made for the displacement, stress and strain field, as well as the DOFs needed in each node and the interpolation scheme between these nodes (Esposito et al., 2022)[4]. After all these choices are made, an appropriate element can be selected. In the next subsections special attention will be given to plane stress, plane strain and interface elements.

3.3.1. Plane stress elements

Plane stress elements are suitable for modelling 2D shapes, with 2D topological dimensions. They have to be “plane”, i.e. the coordinates of the element nodes must be in one flat plane (xy-plane). The elements must be thin, the thickness of the element must be small compared to the dimensions in the plane of the element. Also the loading has to act in the plane of the element. These type of elements are characterized by the fact that the stress components perpendicular to the face are zero, $\sigma_{zz} = 0$ (DIANA FEA, 2022).

In the nodes there are two DOFs, these are translations in the x and y plane. From these deformations DIANA is able to derive the Green-Lagrange strains, given by:

$$\varepsilon = \begin{Bmatrix} \varepsilon_{xx} \\ \varepsilon_{yy} \\ \varepsilon_{zz} \\ \gamma_{xy} \end{Bmatrix} \qquad 3.1$$

For isotropic elements this results in:

$$\varepsilon_{xx} = \frac{\partial u_x}{\partial x}; \varepsilon_{yy} = \frac{\partial u_y}{\partial y}; \varepsilon_{zz} = \frac{v(\varepsilon_{xx} + \varepsilon_{yy})}{1 - v}; \gamma_{xy} = \frac{\partial u_x}{\partial y} + \frac{\partial u_y}{\partial x} \qquad 3.2$$

[4] Source from Brightspace TUD (not publicly accessible).

From these strains DIANA derives the Cauchy stresses, by integrating these stresses over the element thickness the normal and shear forces are calculated. In Figure 3.7 the positive directions of these stresses and forces are shown.

$$\sigma = \begin{Bmatrix} \sigma_{xx} \\ \sigma_{yy} \\ \sigma_{zz} = 0 \\ \sigma_{xy} = \sigma_{yx} \end{Bmatrix} ; n = \begin{Bmatrix} n_{xx} \\ n_{yy} \\ n_{xy} = n_{yx} \end{Bmatrix} \qquad 3.3$$

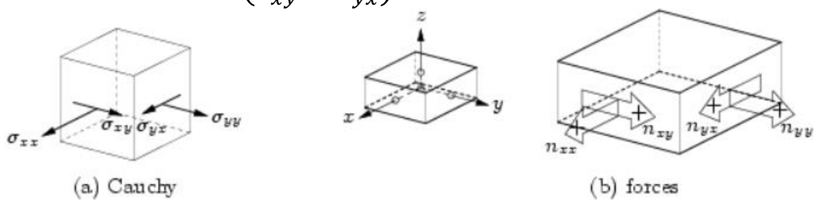

Figure 3.7: Plane stress elements, positive directions (DIANA FEA, 2022)

A regular plane stress element in DIANA is the CQ16M element, shown in Figure 3.8. This is an eight-node quadrilateral isoperimetric plane stress element, based on quadratic interpolation schemes and Gauss integration. The displacements u_x and u_y can be expressed with the polynomial from Eq. 3.4. Typically, this polynomial yields a strain ε_{xx} which varies linearly in x-direction and quadratically in y-direction, a strain ε_{yy} quadratically in x-direction and linearly in y-direction and a shear strain γ_{xy} quadratically in both directions (DIANA FEA, 2022).

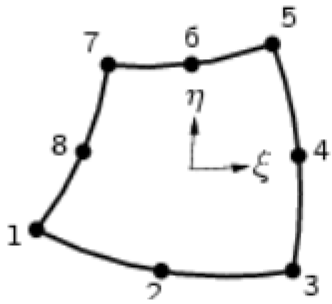

Figure 3.8: Plane stress element, CQ16M (DIANA FEA, 2022)

$$u_i(\xi,\eta) = a_0 + a_1\xi + a_2\eta + a_3\xi\eta + a_4\xi^2 + a_5\eta^2 + a_6\xi^2\eta + a_7\xi\eta^2 \qquad 3.4$$

3.3.2. Plane strain elements

Plane strain elements are suitable for modelling two-dimensional, with two-dimensional topological dimensions. Just as for plane stress elements, plane strain elements have to be positioned in the xy-plane and the loading must act in the plane of the element. The biggest difference between the two types is that for plane stress elements the stress component perpendicular to the element face were zero, whereas for plane strain elements the strain perpendicular to the element face is zero (DIANA FEA, 2022).

Similar to the plane stress elements, there are two DOFs in the nodes, translation in x- and y- direction, which are used to calculate the strains. Due to the nature of the element, these strains will be different compared to the plane stress element and are given by:

$$\varepsilon_{xx} = \frac{\partial u_x}{\partial x} \; ; \; \varepsilon_{yy} = \frac{\partial u_y}{\partial y} \; ; \; \varepsilon_{zz} = 0 \; ; \; \gamma_{xy} = \frac{\partial u_x}{\partial y} + \frac{\partial u_y}{\partial x} \qquad 3.5$$

From these strain equations DIANA is able to derive the stresses, for which the positive directions are shown in Figure 3.9.

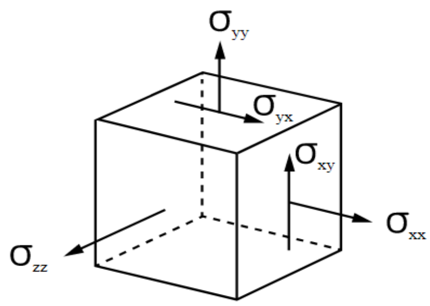

Figure 3.9: Plane strain elements, positive directions (DIANA FEA, 2022)

A regular plane stress element in DIANA is the CQ16E element, shown in Figure 3.10. This is an eight-node quadrilateral isoperimetric plane strain element, based on quadratic interpolation schemes and Gauss integration. The displacements u_x and u_y can be expressed with the polynomial from 3.6. Typically, this polynomial yields a strain ε_{xx} which varies linearly in x-direction and quadratically in y-direction, a strain ε_{yy} quadratically in x-direction and linearly in y-direction and a shear strain γ_{xy} quadratically in both directions. This is actually similar to the CQ16M element used in plane stress conditions, but the differences perpendicular to the face of the element are included (DIANA FEA, 2022).

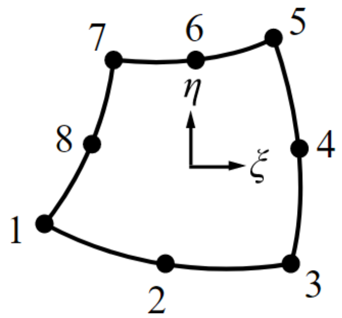

Figure 3.10: Plane strain element, CQ16E (DIANA FEA, 2022)

$$u_i(\xi,\eta) = a_0 + a_1\xi + a_2\eta + a_3\xi\eta + a_4\xi^2 + a_5\eta^2 + a_6\xi^2\eta + a_7\xi\eta^2 \qquad 3.6$$

3.3.3. Structural interface elements

Structural interface elements can be used to model the discontinuous behaviour of a structure, for example discrete cracking and crushing, the formation of plastic hinges and actually all other types of joint behaviour. These type of elements set a linear of nonlinear relation between the normal and shear tractions and the normal and shear relative displacements to describe the behaviour of the interface. During the analysis, the connectivity of the elements does not change, making them not applicable for models with large slip. In DIANA FEA there are six main types of structural interface elements that can be used namely: “Node interface elements, Two dimensional line interface elements, three-dimensional line interface elements, line interfaces to shell elements, line-solid connection interface elements and plane interface elements”. From these six types, only the two-dimensional line interfaces are considered, as the created models in this study will be in the two-dimensional plane (DIANA FEA, 2022).

Two-dimensional line interface elements can be used in both plane stress and plane strain conditions, the used configuration has to be specified on forehand. When a plane stress configuration is considered, the thickness of the interface element has to be defined, which thickness is equal to the out-of-plane thickness. In plane strain conditions, it is not necessary to define the thickness as DIANA automatically evaluates the thickness (DIANA FEA, 2022).

The variables of two-dimensional structural line interfaces are oriented in the local xy-plane. DIANA determines the direction of the local plane automatically. The normal traction (t_{ny}) is perpendicular to the interface and the shear traction (t_{sx}) is tangential to the interface, shown in Figure 3.11.

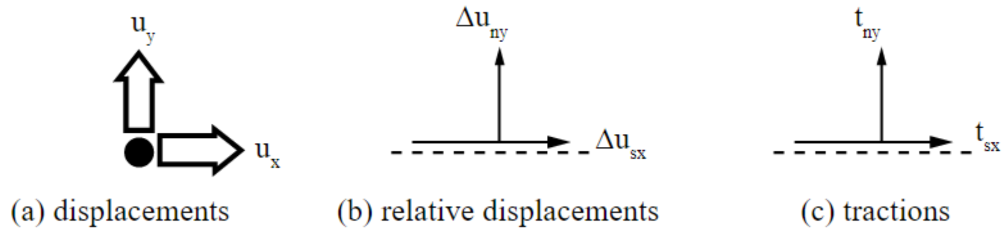

Figure 3.11: Two-dimensional line interfaces, variables (DIANA FEA, 2022)

A typical two-dimensional structural line interface element in DIANA is the CL12I element, shown in Figure 3.12. The local xy-axis for displacements are evaluated in the first node, with the x-axis from node 1 to node 2. This element uses a quadratic interpolation scheme and can therefore be used in combination with the CQ16M plane stress elements from the previous section (DIANA FEA, 2022).

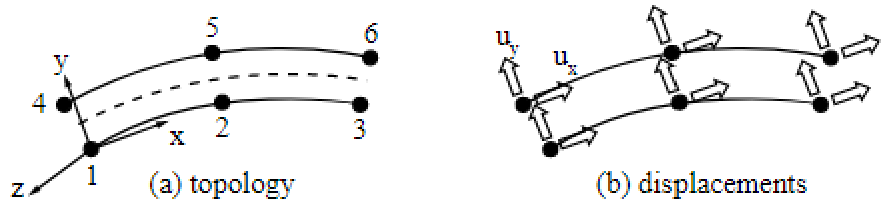

Figure 3.12: Interface element, CL12I (DIANA FEA, 2022)

Within the two-dimensional structural line interfaces multiple models exist for defining the behaviour of the interface. In total there are eight different models available, these models are coupled with the occurring failure mechanisms on micro scale. As is well know, some failure mechanisms are more complex compared to others. For instance, the description for an interface element based on linear elasticity is less complex compared to an interface element for combined cracking-shearing-crushing. It is not only the failure mechanism that determines the choice of a material model, but also the level of complexity needed to capture the problem. In section 3.4 some of the interface material models are explained.

3.4. Material models

In general, there is a wide variety of materials. How materials respond to a load is not equal for all materials. For instance, as mentioned before, masonry behaves different compared to concrete. Over the time, many studies were performed to determine the behaviour of various materials. Next to the different materials, the behaviour also depends on the failure mechanism and the loading conditions that are present. In the following sections different material models for modelling masonry arch bridges described.

3.4.1. Isotropic Total strain crack models

This constitutive model, based on total strain, was developed along the lines of the Modified Compression Field Theory and follows a smeared approach for the fracture energy. The basic concept of the total strain crack models is that the stress is evaluated in the directions which are given by the crack directions. A commonly used approach is the coaxial stress-strain concept, in which the stress-strain relations are evaluated in the principal directions of the strain vector. This is approach is also known as the rotating crack model, which is commonly used for modelling of concrete structures.

However, due to the nature of masonry, it is more appealing to make use of the fixed stress-strain concept. Here the stress-strain relations are evaluated in a fixed coordinate system, which is fixed upon cracking (DIANA FEA, 2022).

During loading and unloading the masonry is subjected to both tensile and compressive stress, which can result in cracking and crushing of the material. In a fixed stress-strain concept the shear behaviour is modelled explicitly with a relation between the shear stress and the shear strain. The deterioration of the material due to cracking and crushing is monitored with six internal damage variables (α_k) collected in the vector α. It is assumed that damage recovery is not possible, which implies that the internal damage variables are increasing. The loading-unloading-reloading condition is monitored with additional unloading constraints, r_k, which are determined for both tension and compression to account for the degradation in tension and compression separately. Figure 3.13 shows the loading-unloading relations adopted in the model (DIANA FEA, 2022).

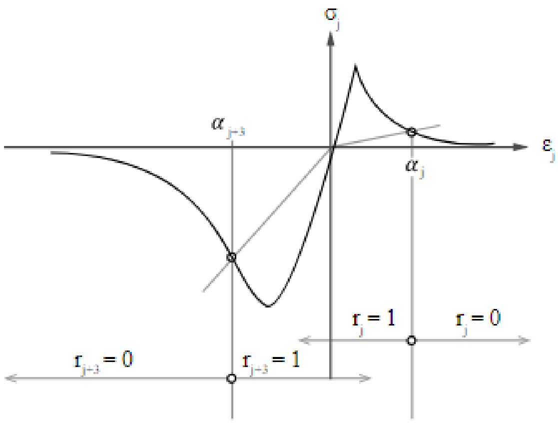

Figure 3.13:Total strain crack models, Loading-unloading relation (DIANA FEA, 2022)

In an incremental-iterative solution scheme, equilibrium between internal force vector and external load vector is achieved with, for instance, the Newton-Raphson iterative procedure. Consequently, the constitutive models should also define the stiffness matrix which is used to achieve equilibrium. Two approaches exist, a secant stiffness matrix and a tangent stiffness matrix. The secant stiffness matrix is commonly used in reinforced concrete structures with extensive cracking, whereas the tangent stiffness matrix is used when localized cracking and crack propagation are the most important phenomena (DIANA FEA, 2022).

The tensile and compressive behaviour can be modelled using different approaches. By performing compressive tests and tensile tests on the used material, a stress-strain curve can be obtained. Comparing this curve to the available curves, a choice can be made which curve captures the real behaviour of the material and needs to be used in the numerical model.

Next to the tensile and compressive behaviour, the shear behaviour can also be modelled. In total strain crack models, this is only necessary in a fixed and rotating to fixed crack concepts. It is expected that after cracking the shear stiffness is reduced, which can be described with different shear retention functions.

3.4.2. Engineering masonry (EM)

The engineering masonry model is a material model based on the general concept of smeared cracking. This model was developed in 2016 and can be used with regular plane stress elements and curved shell elements (DIANA FEA, 2022).

During unloading, the engineering masonry model describes the behaviour with a strong stress decay with the original stiffness. Which is more realistic compared to the secant unloading relation adopted in the total strain crack models. Next to this, a shear failure mechanism, based on standard coulomb friction, is included in the model.

The model includes anisotropy of the masonry by defining a different stiffness for the bed and head joints. The element x-direction is aligned with the bed joints and is normal to the head joints. There are four predefined cracks in the plane of the element, in the direction of the bed joint, the head joint and two diagonals. When the diagonal cracks are not checked or active, the model assumes that there is no coupling between stiffness of the normal components and the in-plane shear component. This makes the model behave as an orthotropic material with Poisson's ratio equal to zero (DIANA FEA, 2022).

The tensile behaviour of the model is given in Figure 3.14, it shows that the softening curve is assumed to be linear. Cracking is assessed either in the directions normal to the bed joints or to the head joints.

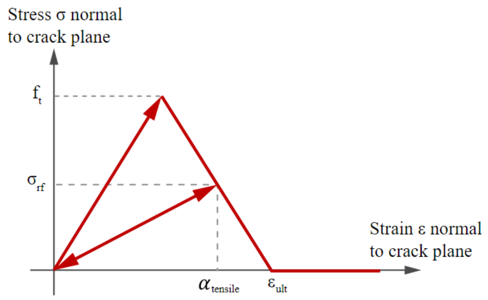

Figure 3.14: Engineering Masonry model, cracking behaviour (DIANA FEA, 2022)

Crushing is also assessed in the directions normal to the bed joints and the head joints. The adopted compressive stress-strain curve is defined by the Young's modulus, compressive strength and compressive crack energy, shown in Figure 3.15. The curve is assumed to be parabolic up to the compressive strength and a linear softening curve until a residual stress of 10% of the compressive strength is reached. The ultimate compressive strain is defined as the strain for which the linear softening curve would have reached the zero stress level.

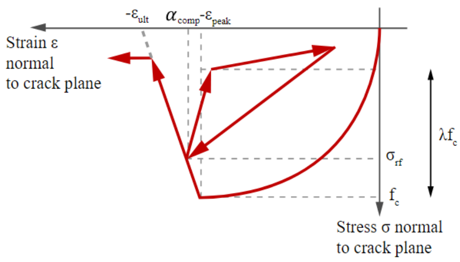

Figure 3.15: Engineering Masonry model, crushing behaviour (DIANA FEA, 2022)

The in-plane shear stress, τ, is defined by the in-plane shear strain, γ, and the stress σ_{yy} in the direction normal to the horizontal joint. This stress is limited by a maximum friction stress, which is defined by coulomb friction (DIANA FEA, 2022). The shear behaviour is shown in Figure 3.16.

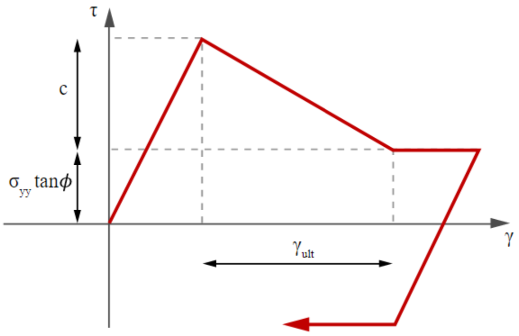

Figure 3.16: Engineering Masonry model, shear behaviour (DIANA FEA, 2022)

3.4.3. Discrete cracking (DC)

This is a material model that can be assigned to two-dimensional structural line interfaces. As mentioned before, the choice of a material model depends on the occurring failure mechanism and the level of complexity needed to capture the problem. The constitutive law for discrete cracking in DIANA is based on the total deformation theory. This theory expresses the tractions as a function of the total relative displacements, the crack width (Δu_n) and the crack slip ($\mathrm{d}t$). It is assumed that both the relations between normal traction and crack width and between shear traction and slip are expressed with nonlinear functions (DIANA FEA, 2022). Next to that, it is assumed that the interface wont fail in compression, so that the relation is linear elastic.

The normal traction (t_n) is, in general, governed by a tension softening relation. In DIANA, there are multiple options to model this tension softening behaviour shown in Figure 3.17. Brittle behaviour is characterized by the full reduction of strength after the criterion has been violated. Linear tension softening relates the ultimate crack strain to the crack energy and tensile strength, $\Delta u_{n,ult} = 2\frac{G_f^I}{f_t}$. The nonlinear tension softening curve was proposed by Hordijk as an expression for the softening behaviour of concrete. This model can be expanded to the hysteresis model, where in both unloading and reloading different paths are followed. It is also possible to define a multilinear tension softening diagram, paired values of traction and relative displacement have to be used as input. This model is mostly used when extensive testing of this behaviour is studied in the tests. The last model is found by the Japan Society of Civil Engineers (JSCE), it is a bilinear curve with a breaking point at $(\frac{0.75G_f}{f_t}\ ; 0.25f_t)$ and is zero at $\frac{5G_f}{f_t}$ (DIANA FEA, 2022).

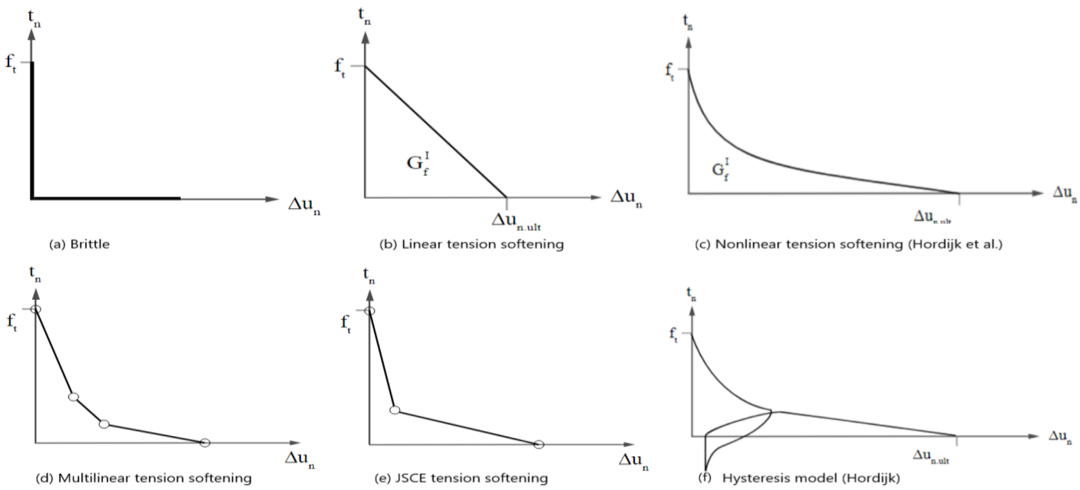

Figure 3.17: Discrete cracking, tension softening behaviour (DIANA FEA, 2022)

3.4.4. Combined cracking-shearing-crushing (CSC)

The combined cracking-shearing-crushing (CSC) interface model is also known as the Composite interface models. This model can simulate fracture, frictional slip and crushing among a material interface, such as masonry at joints in masonry. The model is based on multi-surface plasticity, comprising a Coulomb friction model combined with a tension cut-off and an elliptical compression cap (DIANA FEA, 2022).

Shear slipping is described by a Coulomb friction yield initiation criterion, in which both adhesive - and friction softening are captured. A strain hypothesis is employed, where softening is governed by shear slipping. In tension, the strength is assumed to be softening exponentially. In compression the surface hardens by a parabolic curve, followed by a parabolic or exponential softening curve, as shown in Figure 3.18.

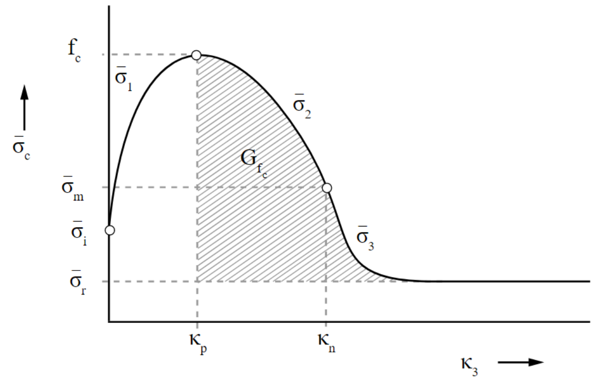

Figure 3.18: Combined Cracking-Shearing-Crushing, Hardening-softening law for compressive cap (DIANA FEA, 2022)

3.4.5. Mohr-Coulomb (MC)

The Mohr-Coulomb model is, as described in section 2.3.2, is a “simple” material model used to describe the behaviour of various soil types. The yield surface of this model can be expressed in the principal stress space as:

$$f(\sigma,\kappa) = \frac{1}{2}(\sigma_1 - \sigma_3) + \frac{1}{2}(\sigma_1 + \sigma_3)\sin\big(\phi(\kappa)\big) - \bar{c}(\kappa)\cos(\phi_0) \qquad 3.7$$

With $\bar{c}(\kappa)$ the cohesion as a function of internal state variable κ, and $\phi(\kappa)$ the angle of internal friction also a function of κ.

For the Mohr-Coulomb yield condition, only strain hardening is considered. This hardening hypothesis determines the relation between the internal state variable, κ, and the plastic process. In the principal space this relation becomes:

$$\kappa = \sqrt{\frac{2}{3}(\dot{\varepsilon}_1^P\dot{\varepsilon}_1^P + \dot{\varepsilon}_2^P\dot{\varepsilon}_2^P + \dot{\varepsilon}_3^P\dot{\varepsilon}_3^P)} \qquad 3.8$$

In DIANA there are two options to consider the tension cut-off, in principle stress space (p-q) or based on the mean stress (σ-τ), shown in Figure 3.19. In principal stress space, the intersection between the tension cut-off and the Mohr-Coulomb yield surface will form an irregular hexagon with six corners. Returning to a corner would involve three active yield zones, two regular and the cut-off, which is a complex situation. By approximating the boundary of the intersection using a smooth elliptical function that goes through all corners, the complex situation is avoided (DIANA FEA, 2022).

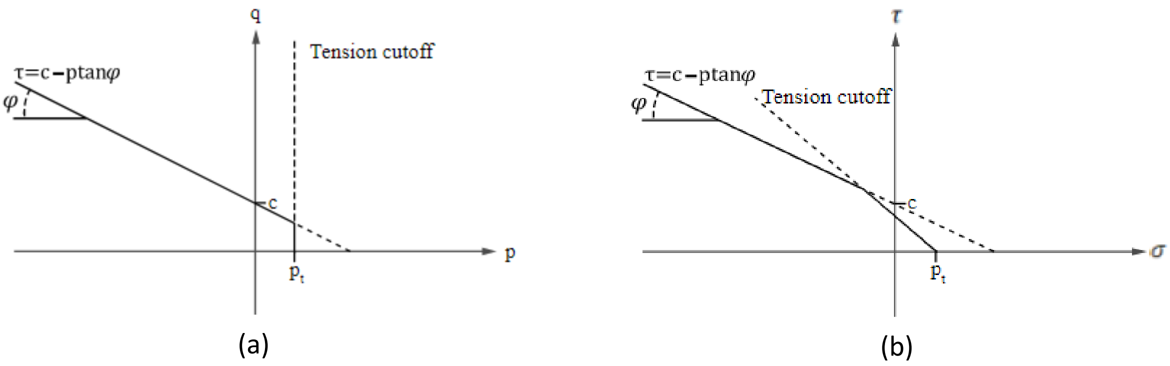

Figure 3.19: Mohr-Coulomb, tension cut-off: (a) in principal directions; (b) bason on mean stress (DIANA FEA, 2022)

3.4.6. Hardening soil model (HS)

The hardening soil model, as described in section 2.3.3, is an advanced material model used to describe the behaviour of soils. The hardening soil model is actually a combination of a nonlinear elastic and a plasticity model, both the volumetric strain (ε_v) and the deviatoric strain (γ) can be decomposed in both an elastic and a plastic part. The hydrostatic pressure (p') is defined in terms of effective stress as:

$$p' = -\frac{1}{3}\left(\sigma'_{xx} + \sigma'_{yy} + \sigma'_{zz}\right) \qquad 3.9$$

To deal with the nonlinear behaviour, DIANA considers the following relation:

$$dp' = -K_t d\varepsilon_v^e \qquad 3.10$$

In which the pressure dependent tangent bulk modulus (K_t) is introduced. To describe this pressure dependency, two different formulations are available, namely the Power law (3.11) or exponential nonlinear elasticity (3.12). In order to use these equations, first the parameters need to be defined based on either a triaxial test or an oedometer test (DIANA FEA, 2022).

$$\mathrm{K_t} = \mathrm{K_{ref}}\left(\frac{\mathrm{p'}}{\mathrm{p'_{ref}}}\right)^{1-\mathrm{m}} \qquad 3.11$$

$$\mathrm{K_t} = \frac{1+\mathrm{e}}{\kappa}\mathrm{p'} \qquad 3.12$$

The parameters for the Power Law nonlinear elasticity model can be found using a drained triaxial test. From such a test, Ohde introduced an equation for the stress dependent stiffness for elastic unloading/reloading (Ohde, 1939). Using this equation, an incremental relationship, the hydrostatic pressure increment ($\mathrm{d}p'$) and the volumetric elastic strain increment ($\mathrm{d}\varepsilon_v^e$), the parameter for the Power Law nonlinear elasticity is defined as given in 3.13. With E_{ref}^{ur} the reference Young's modulus for unloading/reloading, v_{ur} the unloading/reloading poisons ratio and K_{NC} the initial stress ratio.

$$K_{ref} = \frac{E_{ref}^{ur}}{3(1-2v_{ur})}\left(\frac{3K_{NC}}{1+2K_{NC}}\right)^{\beta} \;\; ; \; m = 1-\beta \qquad 3.13$$

When using the Exponential nonlinear elastic model, the parameters can be found using the results of an oedometer test, i.e. one-dimensional unloading. In the case of one-dimensional unloading, the definition for the one-dimensional swelling index, C_s, can be combined with the general relations for an oedometer test. After some rewriting, the parameter for the Exponential nonlinear elastic model is defined according to 3.14.

$$\kappa = (1+2K_{NC})\frac{(1-v_{ur})}{(1+v_{ur})}\frac{C_s}{\ln 10} \qquad 3.14$$

Hardening of the cap yield surface can be modelled using two different hardening laws, namely the Power Law hardening law (3.15) and the Exponential hardening law (3.16). Just as for the nonlinear behaviour, the parameters have to be found making use of tests.

$$\dot{\varepsilon}_v^p = -\Gamma\left(\frac{p_c'}{p_{ref}'}\right)^{m-1}\frac{\dot{p}_c'}{p_{ref}'} \tag{3.15}$$

$$\dot{\varepsilon}_v^p = -\frac{\gamma}{1+e}\frac{\dot{p}_c'}{p_c'} \tag{3.16}$$

Contrary to the nonlinear behaviour, the parameters for the Power Law cap hardening law are found making use of the oedometer test. From such a test, Janbu proposed a relation for the pressure dependence of the oedometer modulus which is similar to the relation that is supposed to describe the nonlinear elastic behaviour (Janbu, 1963). Using these relations combined with general relations for the oedometer test, it was found that parameters can be obtained according to 3.17 (DIANA FEA, 2022).

$$\Gamma = p_{ref}'\left(\sqrt{1+\alpha\eta_{NC}^2}\right)^{\beta-1}\left(\frac{1}{E_{ref}^{oed}}\left(\frac{3}{1+2K_{NC}}\right)^{1-\beta} - \frac{3(1-2v_{ur})}{E_{ref}^{ur}}\frac{1+2K_{NC}}{3K_{NC}}\right); m = 1-\beta \tag{3.17}$$

The exponential hardening law is considered when it is possible to use the one-dimensional compression index, C_c. The parameter γ is found using similar approach to that used for the nonlinear elastic model and given in 3.18.

$$\gamma = \frac{1}{\ln 10}\left(C_c - \frac{(1+2K_{NC})(1-v_{ur})}{(1+v_{ur})}C_s\right) \tag{3.18}$$

3.5. Selected modelling approach

As can be noted from the previous sections, there are multiple choices that have to be made while creating a numerical model, which could influence the accuracy and reliability of the created model. It is therefore important that the engineer has sufficient engineering judgement to make these choices. This judgement is however not only needed to make the choices in the finite element program, but also when selecting appropriate tests. One should keep in mind what the objective of the study is and what is needed to reach that objective. In the following sections, the modelling approach used in this study for both macro and micro models will be given.

3.5.1. Masonry modelling

Recalling from section 2.4.3, there are different modelling strategies that can be followed, micro and macro modelling. The main options how to discretize the masonry structure are shown in Figure 3.20. It is chosen to create a simplified micro model (Figure 3.20(c)) and a macro model (Figure 3.20(d)).

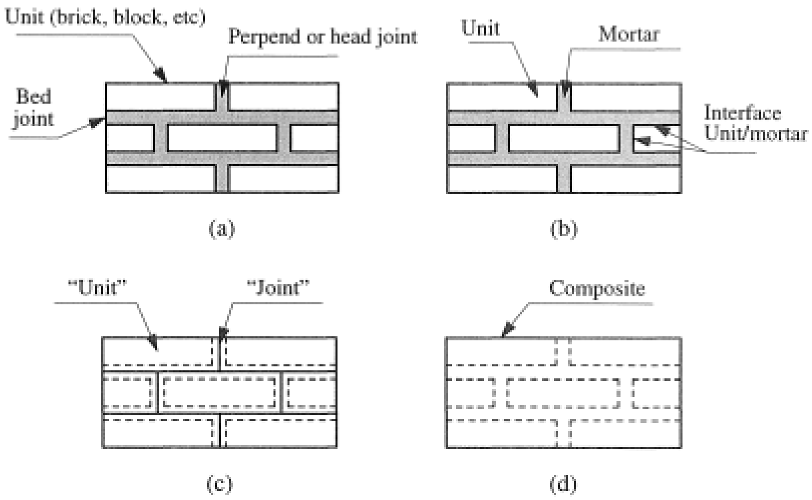

Figure 3.20: Modelling strategies for masonry structures: (a) Masonry sample; (b) Detailed micro-modelling; (c) Simplified micro modelling; (d) Macro-modelling (Lourenço et al., 1995)

In macro models, As explained in Section 2.4.3.2, the units, joints and imperfections are smeared over the geometry. By doing so, the structure is represented as one composite element. Instead of the element being one specific material, like a brick or mortar, the element now represents a composite material and extra attention need to be paid to the properties used for this element.

In the simplified micro model, the area of the bricks is expanded with half the joint thickness in all directions. By doing so, composite elements are created, just as for the macro model. The difference between the models is that in the micro models the joints between the elements are modelled, indicating the potential crack planes. As mentioned in section 2.4.3.1, the units will be modelled making use of continuum elements and the interfaces with discontinuous elements.

3.5.1.1. Macro model - Total strain crack

It is expected that the crack will form in the mortar between the bricks and grows in this plane, meaning a rotation of the crack is not expected. For this reason, the crack orientation is set to be fixed. The tensile behaviour is modelled using the exponential option and the compressive behaviour as parabolic, creating the material model shown in Figure 3.21 (Loarenço, 1996). After this model is evaluated, the impact of a change in material properties is investigated.

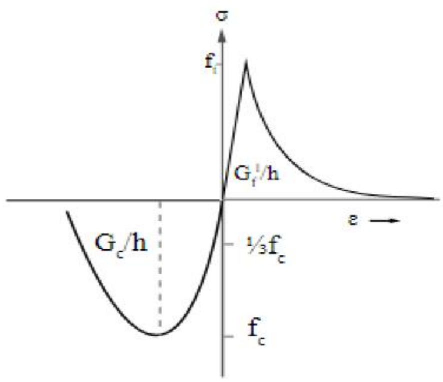

Figure 3.21: Total strain based crack material

3.5.1.2. Macro model - Engineering Masonry

Next to the above mentioned model, a macro model will be created using the engineering masonry material model, described in Section 3.4.2. This is, as explained, an orthotropic material model which should represent the actual behaviour of the masonry better. It is however a material model that could only be used with plane stress elements and is therefore only applicable to the test for just the masonry arch without backfill.

3.5.1.3. Micro model

The micro model will be created, as mentioned, with continuum elements representing the units and discontinuous elements for the interfaces. In micro modelling all discontinuities are "lumped" into the interfaces, as it is assumed cracks will only appear here. With this knowledge, the units will be modelled with a basic linear elastic material model. It is obvious that the description of the interface elements is the crucial part of this model.

As mentioned in Section 2.2.4, a four hinge mechanism is (usually) the critical failure mechanism of the masonry arch. This mechanism is obtained due to the formation of cracks in the mortar-brick interface. It is therefore chosen to make use of the discrete cracking material model with nonlinear tension softening (Figure 3.17(c)), described in Section 3.4.2, to be used to represent the interfaces.

The discrete cracking interface model assumes that the masonry arch could only fail in tension and wont fail in shear or compression. For just a masonry arch this is indeed expected, however, when backfill is added, the shear and crushing failure should be taken into account as well. By selecting the cracking-shearing-crushing material model this can be done

3.5.1.4. Mechanical properties

The properties of materials can be found using various tests, depending on the material that is under investigation and what properties are actually needed. As mentioned in section 2.2.2.1, the force transfer through the masonry arch is mainly compression. Knowing the properties of the materials in compression is therefore of most importance to create a basis for a reliable model. By performing compressive tests on the bricks, mortar and masonry these properties can be found. The properties of the compressive test on the masonry can be assigned to the composite element. However, in absence of this compressive test, the elastic properties for the composite element can also be calculated from the brick and mortar properties using Eq. 3.19, where E_u and E_m are the Young's moduli, Φ_u and Φ_m are the volume fractions and v_u and v_m the Poisson ratios for the units and mortar, respectively (Liu, Feng, & Zhang, 2009).

$$\mathrm{E_{eq}} = \frac{\mathrm{E_u E_m}}{\Phi_\mathrm{u}\mathrm{E_u} + \Phi_\mathrm{m}\mathrm{E_m} - \frac{2\Phi_\mathrm{u}\Phi_\mathrm{m}(\mathrm{v_u E_m} - \mathrm{v_m E_u})^2}{(1-\mathrm{v_u})\Phi_\mathrm{m}\mathrm{E_m} + (1-\mathrm{v_m})\Phi_\mathrm{u} E_\mathrm{u}}} \qquad 3.19$$

For the micro model, the properties of the unit-mortar interface also need to be defined. As described in section 3.3.3, structural interface elements describe a relation between tractions and relative displacement. This relation is modelled using linear material properties, normal and shear stiffness modulus, and nonlinear properties. How the non-linear relation is described depends on the chosen material model, but, the linear material properties are for all material models equal. These stiffness properties are calculated using Eq. 3.20, where G_u and G_m are the shear moduli for the units and mortar, respectively, and h_m the actual thickness of the joint (Lourenço et al., 1995) (CUR, 1994).

$$k_n = \frac{E_u E_m}{h_m(E_u - E_m)} \;\; and \; k_s = \frac{G_u G_m}{h_m(G_u - G_m)} \qquad 3.20$$

There also exists the possibility that the properties of the masonry are either not tested or poorly reported. In this case, average values for masonry can be used reported in Dutch practice guidelines (NPR 9998:2020, 2020). In this guideline difference is made between four types of masonry: “bricks used before 1945; bricks used after 1945; sand-lime bricks with mortar used after 1960; sand-lime bricks with adhesive mortar used after 1985”. Although this is very useful, it is preferred to use properties reported in the tests.

3.5.2. Backfill modelling

The backfill will, and can only be, modelled using a macro material model. There are two different material models available for modelling soils, the Mohr-Coulomb model, described in section 2.3.2, and the hardening soil model, described in section 2.3.3. The hardening soil model is expected to represent the behaviour of the soil better compared to the Mohr-Coulomb model. However, for the HS model more parameters need to be defined making the model more complex and, increasing the computational power needed.

In this study, the effect of changes in material properties will be investigated, increasing the number of analysis that have to be calculated. As it is, yet, unknown whether a change in material properties also changes the response, it is useful to have a relatively “quick” model. For this reason, the backfill will be first modelled making use of the Mohr-Coulomb material model. When the critical parameters are found, the model will also be calculated using the Hardening soil material model and compared to the Mohr-Coulomb model.

3.5.2.1. Mechanical properties

Similar to the masonry properties, the properties of the backfill can be determined with various tests. Next to that, there has been significantly more research performed on different soil types and their properties. As a result, sophisticated material models (Sections 3.4.5 & 3.4.6) and mean values exist that can be used for these models (DIANA FEA, 2022). Although this is handy, the properties of soils vary based on the compaction, porosity, saturation, etc., making it necessary to report soil properties for every test that is performed. With this knowledge, it is expected that the soil properties can be taken from the to be investigated test.

Special attention needs to be given to the soil-structure interaction. Just as for the unit-mortar interface, interface elements can be used to describe this interaction. It is usually the case that the interaction is given with a reduction factor, R_{inter}. This reduction factor relates the properties of the soil to the properties of the interface according to Eq. 3.21 (Bentley, 2023), where c_i and c_{soil} are the cohesion and φ_i and φ_{soil} the friction angle of the interface and soil, respectively.

$$\begin{gathered} c_i = R_{Inter} * c_{soil} \\ \tan(\varphi_i) = R_{inter} * \tan(\varphi_{soil}) \end{gathered} \tag{3.21}$$

3.5.3. The analysis

There are multiple analysis that can be performed in DIANA, just as for basically all features. It is chosen to run a phased structural nonlinear analysis. In the first phase, the structure is created and the dead weight is added. In the second phase the structure is subjected to a displacement controlled load to overcome the turning point. This phased analysis is performed to ensure that the self weight is fully present during loading, as the self weight helps to balance the system. In order to do so, in the second phase a so called “start step” needs to be added which uses the load of the previous phase.

In the analysis both physical and geometric nonlinear effects are considered, as described in section 3.2.1. Equilibrium is reached using the modified Newton-Raphson iterative solution scheme, while satisfying both the energy and displacement based convergence norms, as explained in section 3.2.2.

4. Validation against isolated masonry arch, Minho test

At the university of Minho in Portugal a series of tests were performed to investigate the performance of arched masonry structures strengthened using composite materials. Various tests were performed to determine properties of the masonry and the composite materials used for strengthening. Using these experimentally determined properties, numerical models were made and their results were compared to the tests results. In order to quantify the strengthening method, unreinforced arches were constructed and tested first (Basilio Sánchez, 2007). This first part is used in this study.

The study performed at the university of Minho is selected for two reasons. Firstly, due to the absence of backfill, these tests form a good opportunity for the comparison of micro- and macro modelling strategies. Differences in the output of the models can be related directly to the chosen strategy. Secondly, most of the physical and mechanical properties used in numerical models were determined using, well reported, laboratory tests. Therefore, less assumptions have to be made. In the following sections the mechanical properties, test setup, test results and numerical model will be discussed.

4.1. Mechanical properties

The properties of the masonry were experimentally found. The bricks, mortar and masonry were tested separately to find the compressive strength and Youngs modulus. Next to these compressive tests, bond tests were also performed to find the bond strength of the mortar. Other values needed for the numerical modelling were taken from mean values of previous works (Lourenço P. , 1994) (Liberatore, Marotta, & Sorrentino, 2014).

4.1.1. Brick properties

The compressive strength (f_b) is one of the fundamental properties of the bricks, for this reason two sets of five compressive tests were performed. The first set of tests was carried out without strain gauges and had the purpose of finding the average compressive strength, for the second set strain gauges were applied per specimen in order to find the Young's modulus.

4.1.1.1. Test setup

The test setup consisted of a steel frame which supports a servo-controlled testing machine with a load cell with a maximum capacity under compression of $25\ kN$, shown in Figure 4.1(a). In the second series, the strain gauge was fixed to the central piece in the loading direction to find the Young's modulus. Next to this, three linear variable displacement transducers (LVDTs) were used to compute the deformability of the specimens, shown in Figure 4.1(b).

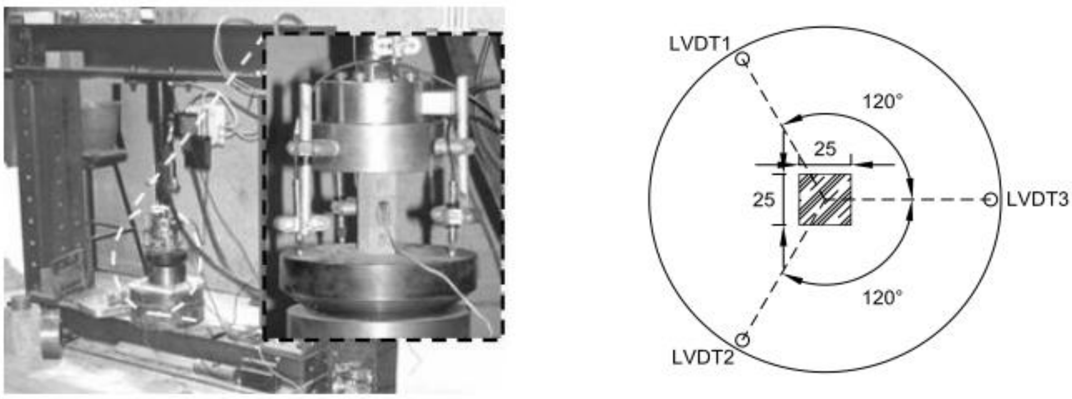

(a) (b)

Figure 4.1: Compressive material test setup and location of LVDTs

4.1.1.2. Test results

The results of the tests are shown in Table 4-1. Considering the compressive strength, the results of both series show a high scattering. Compressive strengths determined by the strain gauges are higher compared to the results without the strain gauges. Next to that, results regarding the Young's modulus are also dependent on the data source used. Young's modulus calculated from strain gauges gives a higher value compared to the calculation from the LVDTs. These differences can be result of several issues, mainly regarding the porosity and the resin used to glue the strain gauge to the specimen. In fact the pores are filled with the glue used to fix the strain gauges, causing a significant increase in local stiffness and making the results less reliable compared to the results obtained by the LVDTs.

Table 4-1: Bricks compressive mechanical characterization

Specimen	Compressive stress σ_b(MPa)	Young's modulus (GPa)	
		E_{sq}	E_{LVDT}
1 - 1	7.1	-	-
1 - 2	7.3	-	-
1 - 3	7.1	-	-
1 - 4	5.8	-	-
1 - 5	5.3	-	-
2 - 1	15.5	5.30	3.19
2 - 2	10.6	3.38	1.65
2 - 3	10.2	4.10	1.10
2 - 4	9.2	6.05	1.87
2 - 5	9.1	5.63	1.34
Average	8.7	4.89	1.83
C.V. (%)	34.1	22.8	44.5

Figure 4.2(a) presents a typical compressive stress strain curve, where Figure 4.2b shows the range of variation of all tests carried out and reported in Table 4-1.

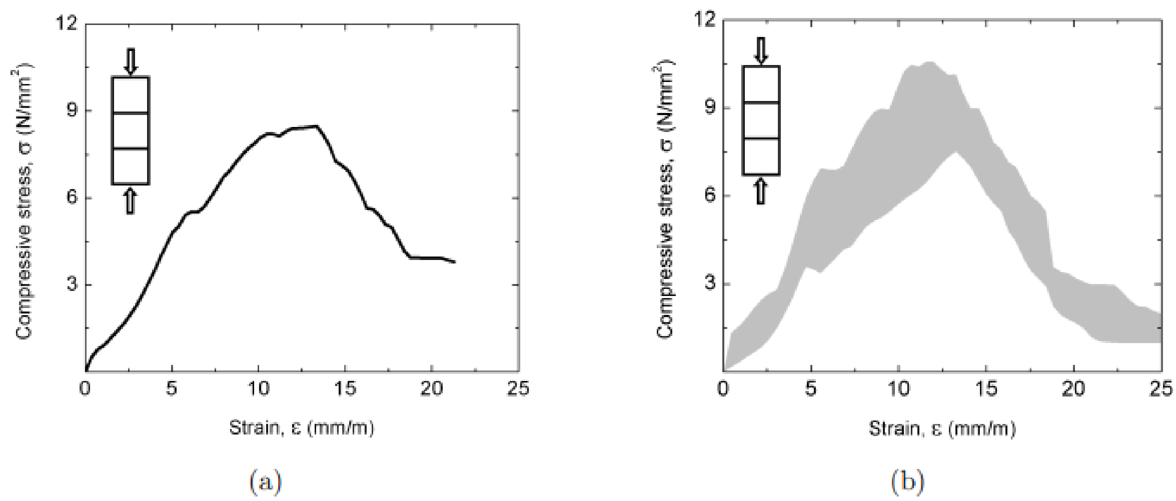

Figure 4.2: Brick compressive test (a) Typical compressive stress-strain curve and (b) compressive envelope of test results

4.1.2. Mortar properties

The mortar that is used in for the construction of the masonry arches was purchased from on of the biggest producers for chemical products in the building industry (MAPEI). The selected mortar was developed for the repair of historic masonry constructions, called Mapei-Antique MC. It is a premixed light-coloured cement-free powder mortar based on special hydraulic binder with pozzolanic action, natural sand, special additives and synthetic fibres and can be defined as based on hydraulic lime binder. The manufacturer provided technical information for the mortar, shown in Table 4-2. Despite of this information, it was chosen to perform tests on the mortar to determine the properties.

Table 4-2: Mortar, technical information by manufacturer

Mechanical properties	*Cure period of testing (days)*	
	7	28
Compressive strength σ (MPa)	2-4	4-6
Young's modulus E (GPa)	3-4	4-6

4.1.2.1. Test setup

To obtain the mortar properties, a test similar to that used for the brick specimens was used. Again two series were considered, one to find the compressive strength and one to find the Young's modulus. The specimens were poured and tested on day 15. The test setup is shown in Figure 4.1(a), again the deformability was measure using three LVDTs shown in Figure 4.1(b).

4.1.2.2. Test results

The results of the two test series are shown in Table 4-3. Comparing the results of the tests with those provided by the manufacturer, it can be noticed that the average compressive stress in the tests was higher and the average found Young's modulus is lower. This can be the cause of differences in used water quantity and humidity during the curing process.

Table 4-3: Mortar, mechanical characterization

Specimen	*Compressive stress σ (MPa)*	*Young's modulus E (GPa)*
1 - 1	6.4	-
1 - 2	7.3	-
1 - 3	7.1	-
1 - 4	6.7	-
2 - 1	7.7	1.37
2 - 2	7.6	1.67
2 - 3	8.0	2.79
2 - 4	7.9	1.37
Average	7.3	1.80
C.V. (%)	7.8	37.5

Figure 4.3: Mortar compressive test (a) Typical compressive stress-strain curve and (b) compressive envelope of test results

a below shows a typical compressive stress-strain curve, as well as the range of variation of all tests reported in Table 4-3. From Figure 4.3(b) it can be seen that the post peak behaviour of the mortar is characterized by a smooth decrease in strength.

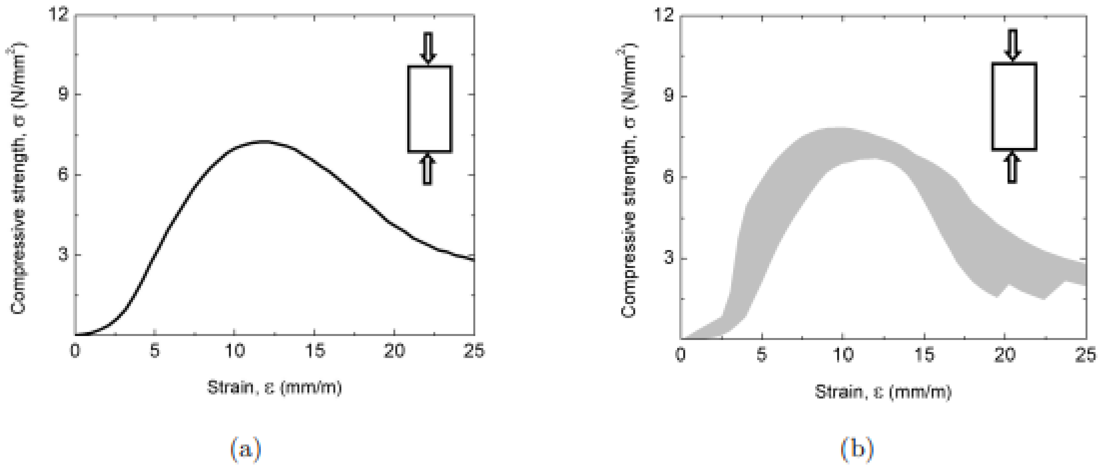

Figure 4.3: Mortar compressive test (a) Typical compressive stress-strain curve and (b) compressive envelope of test results

4.1.3. Masonry properties

As mentioned, next to the properties of the individual components, the properties of the masonry were tested also. Again the goal was finding the compressive strength and young's modulus.

4.1.3.1. Tests setup

Again compressive tests were carried out by means of a servo-controlled machine, with a load cell with a maximum capacity of 200 kN. The same procedure as for the individual bricks and mortar was used, two series of tests and using LVDTs to measure the deformability of the specimens (Figure 4.1).

The specimens were created from 5 bricks with mortar layers of approximately 10 mm in between them (Figure 4.4). To promote better contact and uniform stress distribution, the top and bottom surface of the brick were regularized with a grinding machine to obtain a flat surface. After a curing period of two weeks, the prisms were tested.

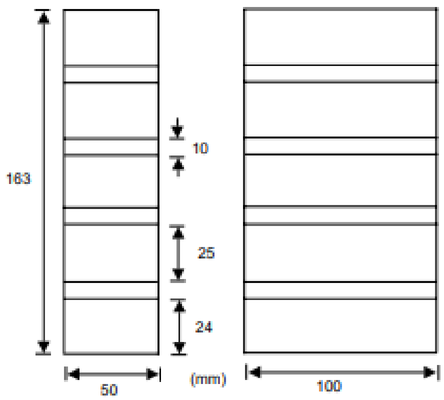

Figure 4.4: Masonry, Specimen and dimensions

4.1.3.2. Test results

The results of both test series are shown in Table 4-4. A slightly higher compressive strength and Young's modulus was found for the masonry compared to the individual components, these are however quite close.

Table 4-4: Masonry, mechanical characterization

Specimen	Compressive stress σ (MPa)	Young's modulus E (GPa)
1 - 1	8.39	-
1 - 2	9.11	-
1 - 3	8.53	-
1 - 4	7.07	-
1 -5	7.98	-
2 - 1	7.7	3.05
2 - 2	10.9	1.32
2 - 3	9.3	1.62
2 - 4	11.4	1.79
2 - 5	10.3	2.41
Average	9.1	2.04
C.V. (%)	15.7	33.9

Again the typical stress-strain curve and the range of variation of all tests is shown in Figure 4.5. A wide variation in Young's modulus is observed within the stress range of 30% to 60%of the peak load. The specimens showed a low ductility.

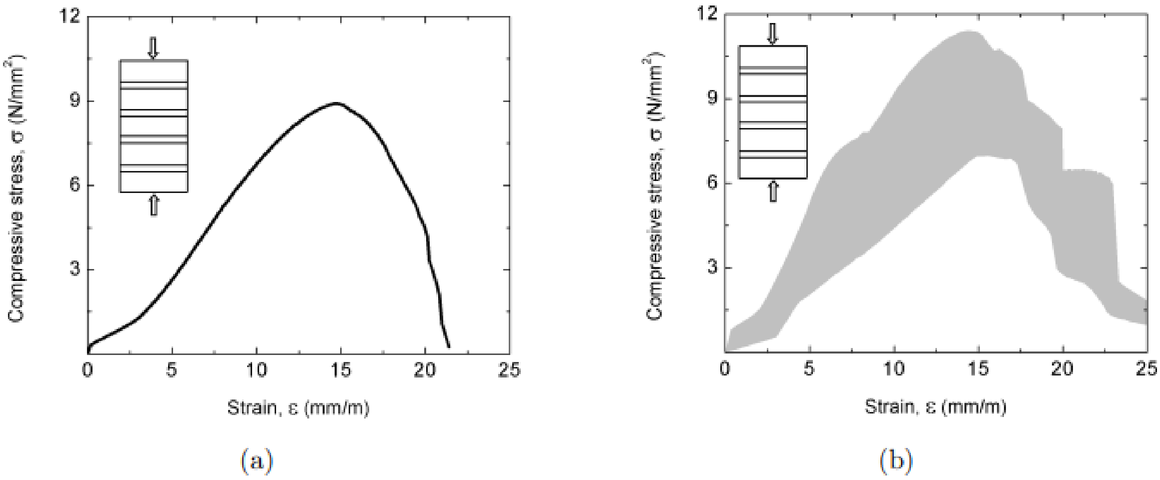

Figure 4.5: Masonry compressive test (a) Typical compressive stress-strain curve and (b) compressive envelope of test results

To gain more insight in the masonry behaviour, the average curves of the brick, mortar and masonry are shown in one graph (Figure 4.6). It can be noticed, that after the seating effect of the masonry, a similar stiffness and strength can be found for the masonry and bricks.

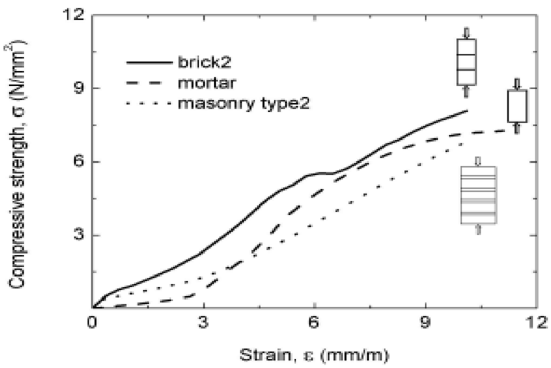

Figure 4.6: stress-strain curve brick, mortar and masonry

4.2. Test setup

The arch geometry and test set-up are shown in the figures below, numerical values are given in the Table 4-5 below.

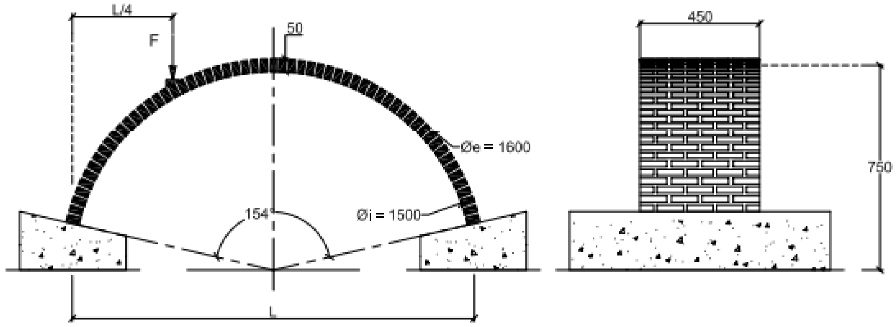

Figure 4.7: Minho test, arch geometry

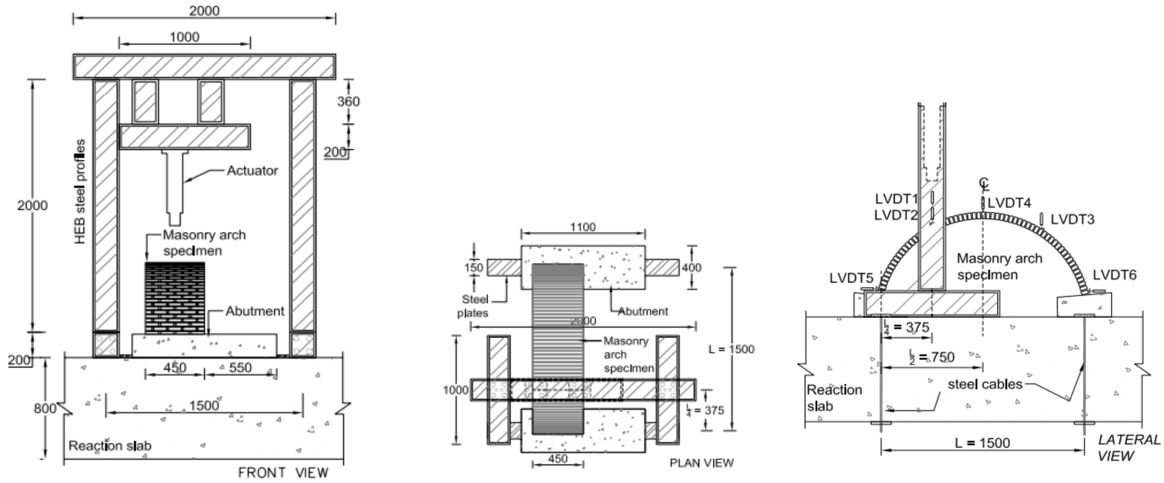

Figure 4.8: Minho test, test setup and data acquisition

Table 4-5: Minho test, arch dimensions

Shape	semicircular		
Span	1462 mm	Abutment angle	13°
n_{bricks}	59	Brick dimensions	100*50*25 mm^3
Internal diameter, θ_i	1500 mm	External diameter, θ_e	1600 mm
Arch thickness	50 mm	Arch depth	450 mm
Arch height	750 mm		

As can be seen from Figure 4.7, the shape of the arch is semi-circular. The abutments were made from concrete cast on rectangular steel plates fixed to the reaction laboratory slab, preventing horizontal displacement.

The load was applied at quarter using the actuator, positioned at the middle of the width of the arch to reach an uniform transversal loading. A triangular bar made from wood was glued to the extrados of the arch, this functioned as a platform for a rectangular rigid steel bar in order to guarantee a uniform loading. The load was applied in a displacement controlled manner, with a rate of 3 µm/s.

The deformation of the arch was monitored using six linear variable displacement transducers (LVDTs) fixed to relevant locations to record the deformation. LVDT-1 to LVDT-4 were used to record the vertical displacements at both quarter spans and the crown. LVDT-5 and LVDT-6 were used to record the horizontal displacement of the arch springing.

4.3. Test results

Test results were given as a load-displacement curve below the loaded section, so at quarter span. Next to this, the locations of the hinges and their sequence of appearance were found by visual inspection of the structure. Together these result give a clear view of the behaviour of the arch.

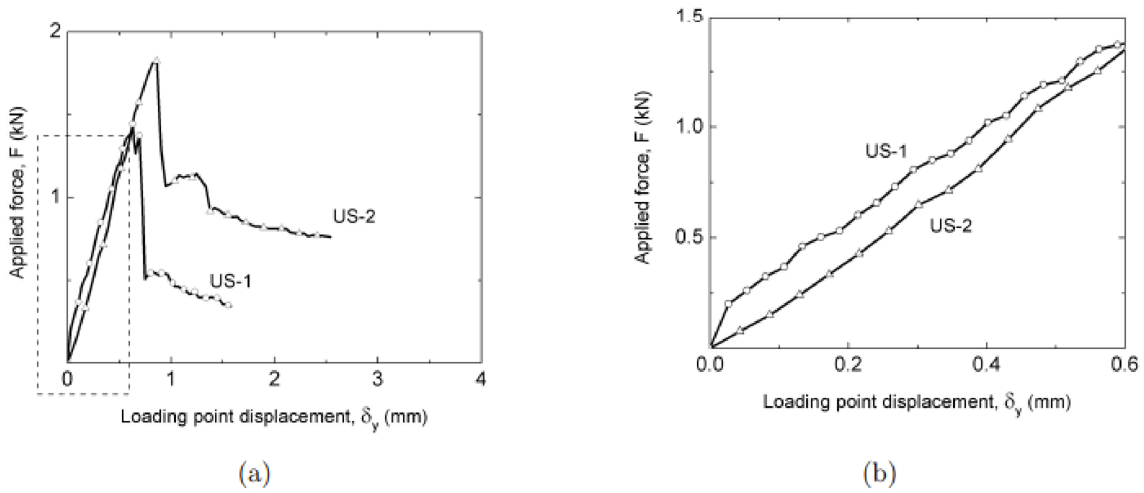

Figure 4.9: Minho test results, force-displacement curve: (a) full path; (b) zoom of squared dashed line

As can be seen from Figure 4.9(a), a sudden drop in load-bearing capacity was found after reaching the peak load. Failure was characterized by brittle behaviour. It can also be noted that the initial stiffness of both specimens are close, however the peak load of US-1 is lower than US-2. This could be caused by differences in the craftmanship in both specimens.

Both specimens collapsed due to the formation of a four hinge mechanism, which were formed before the peak load was reached. The appearance of a four hinge mechanism was also expected to be the governing failure mode. In Figure 4.10, the sequence of hinge formation is shown, with H1 the first hinge and H4 the fourth hinge that was found. Corresponding to the formation of hinges, Table 4-6 reports the load at which the hinges are formed.

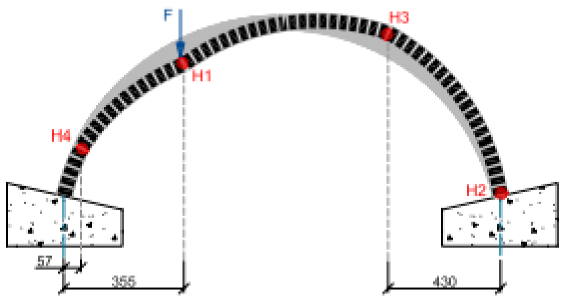

Figure 4.10: Hinge formation sequence

Table 4-6: Minho test results, numerical relationship between hinge formation sequence and applied force (in kN)

	1^{st}	2^{nd}	3^{rd}	4^{th}
US-1	0.6	1.0	1.2	1.4
US-2	0.7	1.1	1.4	1.8

4.4. Numerical model

4.4.1. Model description

The study performed at the university of Minho aimed at finding strengthening methods for masonry arches. To do so, a numerical model was created and compared to test results. This model was used to identify critical locations in the masonry arch and find the optimal location for strengthening operations. A micro modelling approach was followed, defining the units and unit-mortar interface separately (Figure 4.11). The masonry units were modelled using eight-noded plane stress elements described Section 3.3.1 and unit-mortar interface was modelled using six-noded interface elements described in Section 3.3.3.

In this micro modelling approach, the units (i.e. bricks) behave in linear fashion and the interfaces contain the non-linear properties. A composite interface model formulated within the framework of plasticity was used. This model includes a tension cut-off for mode I failure (G_F^I), the Coulomb friction envelope for mode II failure and a cap mode for compressive failure.

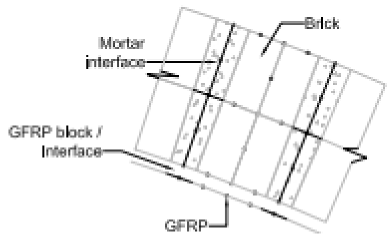

Figure 4.11: Model representation

The properties used in the models were both experimentally found and obtained from mean values of previous works. Table 4-7 and Table 4-8 report the elastic and inelastic properties adopted in the models.

Table 4-7: Elastic properties for brick and interface

Element	E MPa	v -	k_n N/mm^3	k_s N/mm^3
Brick	5000	0.2	-	-
Interface$_{masonry}$	-	-	24	10

Table 4-8: Inelastic interface properties

	tension		*Shear*				*Compression*		
	f_t MPa	G_f^I J/m^2	c MPa	$\tan\phi$ -	$\tan\varphi$ -	G_f^{II} J/m^2	f_m MPa	G_{fc} J/m^2	κ_p -
Masonry	0.18	0.03	0.3	0.75	0.0	0.1	7.8	90	10

4.4.2. Numerical results

Results of the numerical model together with the results of the tests are shown in Figure 4.12(a). Next to the full path, attention has been paid to the linear part of the test an numerical model (Figure 4.12(b)). It can be seen that the numerical model is reasonable close to the results obtained by the tests.

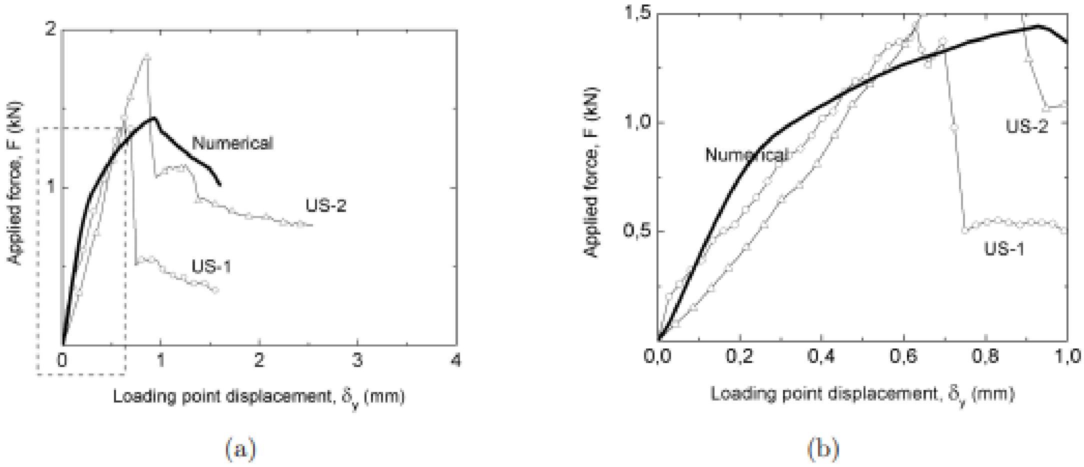

Figure 4.12: Minho test results and presented numerical results, (a) full path (b) linear part

Contrary to the experimental tests, the numerical model is capable of perfectly identifying the appearance of hinges and its sequence over the loading history. To make this sequence visible, the sequence of hinge formation is shown in the load-displacement curve shown in Figure 4.13. It can be seen that just as in the tests the four hinges were formed before failure of the arch. A comparison between the visible and numerical found hinges is given in Table 4-9.

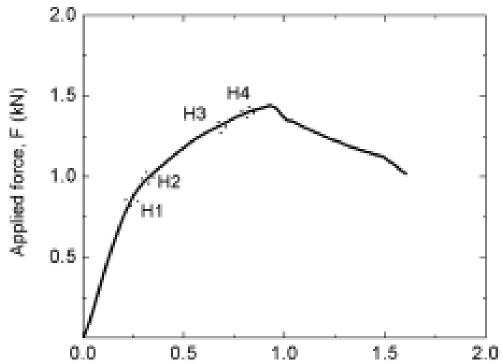

Figure 4.13: Presented model, hinge formation sequence

Table 4-9: Hinge formation sequence

Specimen	*Numerical relationship between hinge formation sequence and applied force*							
	1st		2nd		3rd		4th	
US-1	(0.6)	0.84	(1.0)	1.1	(1.2)	1.35	(1.4)	1.44
US-2	(0.7)		(1.1)		(1.4)		(1.8)	

Note: Experimental values within brackets; all values in kN.

4.4.3. Discussion of model

The numerical model shows decent comparison with the test results when looking at the maximum load and the hinge formation sequence. However, some differences also appear and need to be pointed out, starting with the properties used to model the masonry. For the linear part of the response the Young's modulus defines the slope of the force-displacement curve. The Young's modulus used in the numerical model is 5 GPa, which is not in line with compressive test results. As a micro model was created, it was expected that the Youngs modulus would be taken from the tests on both the bricks and mortar, reported in Sections 4.1.1 and 4.1.2. For both bricks and mortar a Youngs modulus of roughly 1.8 GPa was found, based on the more reliable LVDT results. If a simplified micro-modelling approach was followed, it could also be chosen to use the results based on the masonry tests from Section 4.1.3, where a Young's modulus of 2.04 GPa was found. However, a clear overview of the created model and the origin of the used properties is lacking in the report. The effect of using an "inaccurate" Young's modulus becomes visible when taking a closer look at Figure 4.12(b). It shows that the slope of the numerical model is greater compared to the slope of both tests, which is expected as a higher value of the Young's modulus was used. However, this should not be the case as the Young's modulus was experimentally found.

Another difference is found when taking a closer look at the post-peak behaviour. The tests show a large drop in the force-displacement curve, indicating brittle failure. In contrast, the numerical model does not show this drop, not capturing the actual behaviour. It could be the case that the preparation of the arch was not done with great precision, however both tests show the same post-peak behaviour, making it more reasonable to question the post peak behaviour of the created numerical model.

4.5. Modelling of Minho test

In order to study the differences between micro- and macro modelling techniques used for simulating the behaviour of masonry arch bridges, in this section both a macro- and micro model will be created. First two distinct different macro models will be considered, after which a micro modelling approach will be followed.

4.5.1. Macro model - Total strain crack

4.5.1.1. Model description

The macro model that will be created follows the approach explained in Section 3.5. In short, masonry is modelled using the total strain based crack model with a fixed crack orientation. It is assumed that the behaviour in tension can be described using the linear crack energy curve and in compression using a parabolic curve. The assumption for a parabolic curve in compression seems accurate when comparing the tests results from Section 4.1.3.2 with the available compressive curves from **Fout! Verwijzingsbron niet gevonden.**.

Using the geometry and boundary conditions given in Section 4.2, the model is created as shown in Figure 4.14. It can be seen that the arch is modelled using multiple shapes instead of using one shape. However, the shapes are perfectly connected, creating a macro model. For all elements of the arch, a local reference system is assigned in such a way that the output of stresses and strains are given in the principal directions.

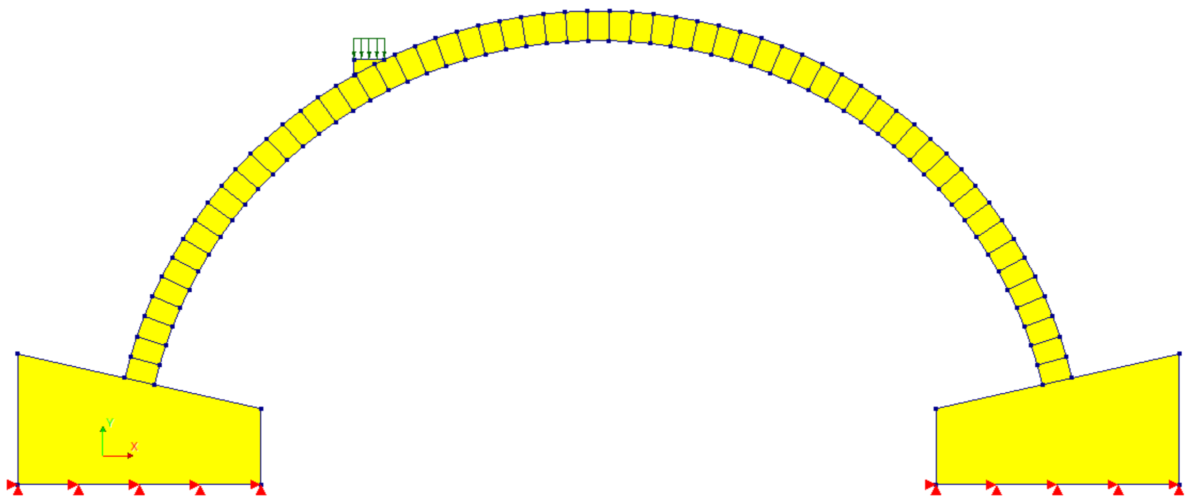

Figure 4.14: Macro model overview

4.5.1.2. Model properties

For the analysis it is chosen to follow the approach explained in Section 3.5. As mentioned, the Young modulus will be taken from the compressive test reported in Section 4.1.3, other values are taken to be similar to those reported in the paper, with an exception for the young modulus (Basilio Sánchez, 2007). As was discussed in Section 4.4.3, the young modulus was taken to be too high. Here it is chosen to make use of the Young's modulus from the compressive tests of Section 4.1.3.2. All properties used in the model are given in Table 4-10.

Table 4-10: Total strain crack model properties

Masonry properties total strain based crack model		
Linear material properties		
Young's modulus	E	$2040\ MPa$
Poisson's ratio	v	0.2
Mass density	ρ	$2300\ kg/m^3$
Total strain based crack model		
crack orientation		Fixed
Tensile behaviour		
tensile curve		Exponential
Tensile strength	f_t	$0.18\ MPa$
Mode-I tensile fracture energy	G_f^I	$0.03\ J/m^2$
crack bandwidth specification		Rots
Residual tensile strength		$0\ MPa$
Poisson's ratio reduction		No reduction
Compressive behaviour		
Compression curve		Parabolic
Compressive strength	f_c	$7.8\ MPa$
Compressive fracture energy	G_{fc}	$90\ J/m^2$
reduction due to lateral cracking		No reduction
Stress confinement model		No increase
Shear behaviour		
Shear retention function		Constant
Shear retention	β	0.01

4.5.1.3. Results

In the following figures the results of the performed analysis are given. Looking at the force displacement curve shown in Figure 4.15, it can be seen that the numerical model is able to come close to the tests results. A peak load of $1.28\ kN$ is calculated, which is close to the peak load of $1.44\ kN$ found in the first test series. The peak load is, however, achieved at a larger displacement. Next to that, the tests show a more brittle failure compared to the numerical model.

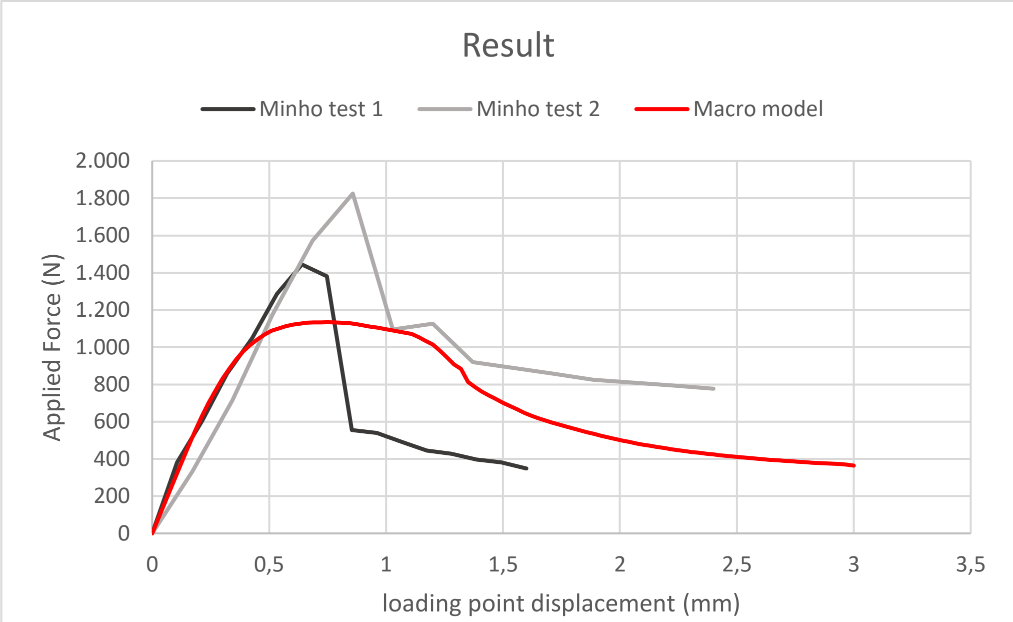

Figure 4.15: Total strain crack, force-displacement curve

Next to the load displacement curve, the results of the tests also reported the sequence of hinge formation. One of the benefits of using a numerical model, is that this hinge formation can be determined with great precision. As expected, the first crack occurred just below the loading point, shown in Figure 4.16. It can also be seen where the other cracks start to form, which is in line with the test observations. However, in the numerical model the first crack occurred in load-step 13, corresponding to a displacement of $0.36\ mm$ and a load of $938\ N$.

The second crack occurred in load-step 30 (Figure 4.17), corresponding to a displacement of $0.87\ mm$ and a load of $1280\ N$, which is the location of the peak load. The third hinge was formed in load-step 40 (Figure 4.18), corresponding to a displacement of $1.17\ mm$ and a load of $1216\ N$. After the fourth and final hinge is formed, the arch fails. This happened in load step 50 (Figure 4.19), corresponding to a displacement of $1.47\ mm$ and a load of $1095\ N$.

In Figure 4.20 the formation sequence of the hinges corresponding to the test and numerical results are shown in the load displacement curve. The hinges are shown with circular shapes on the curve.

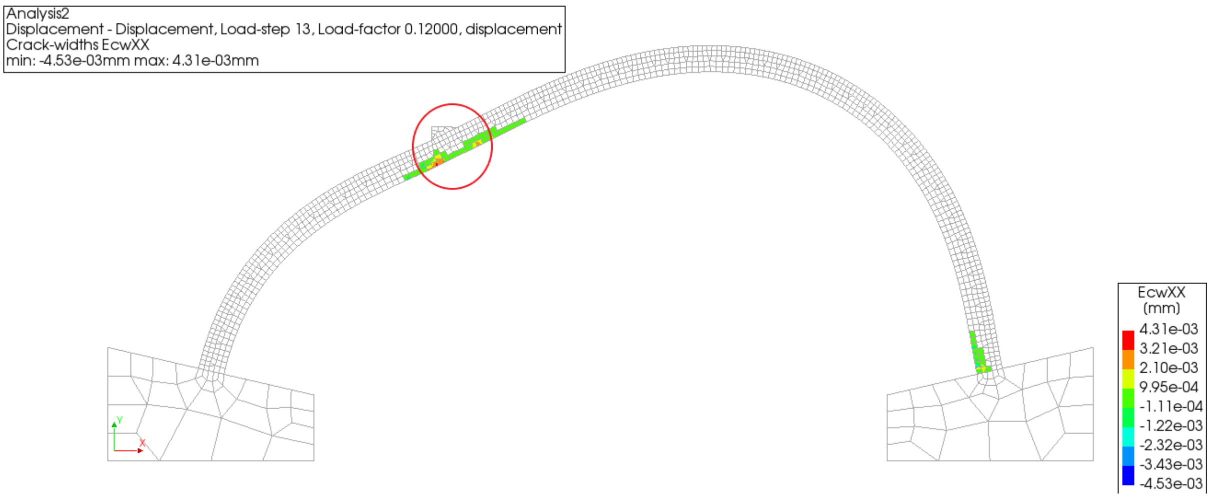

Figure 4.16: Total strain crack, location of first hinge

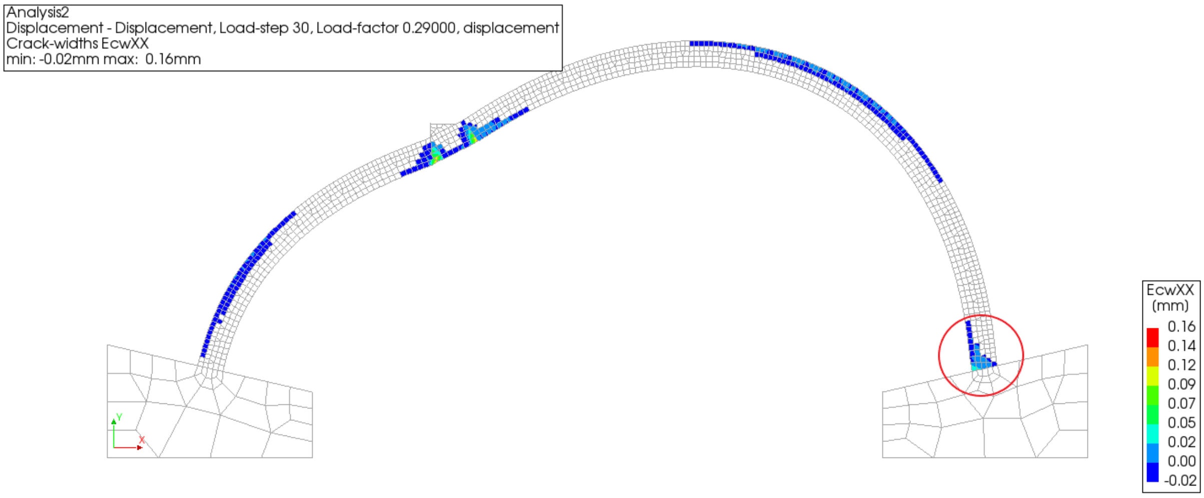

Figure 4.17: Total strain crack, location of second hinge

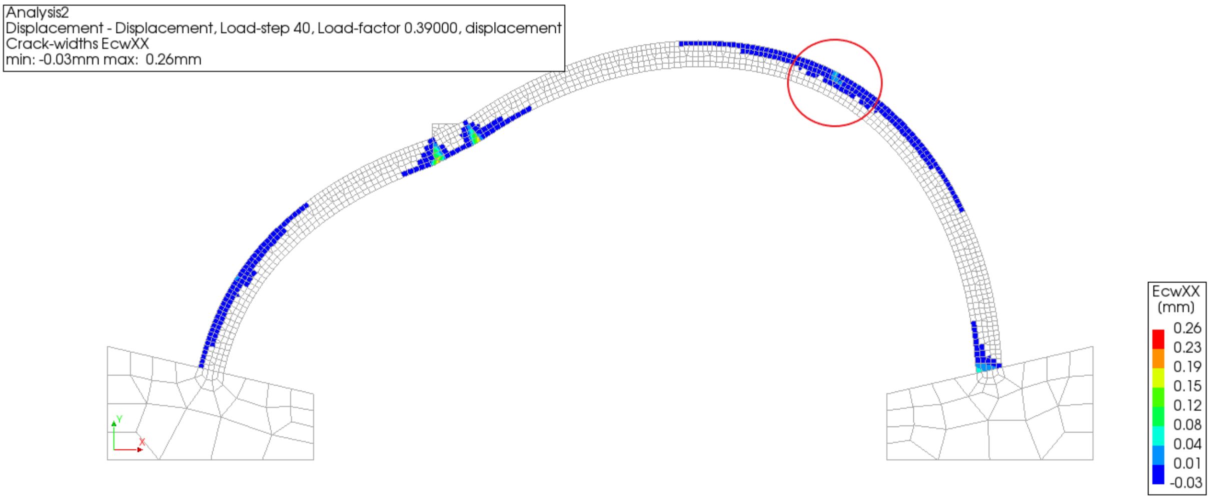

Figure 4.18: Total strain crack, location of third hinge

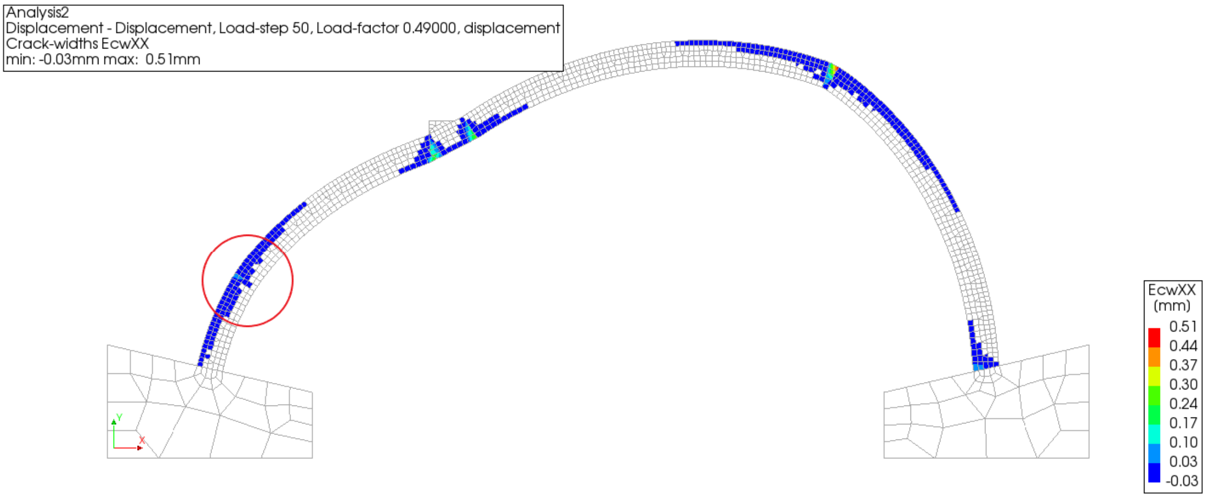

Figure 4.19: Total strain crack, location of fourth hinge

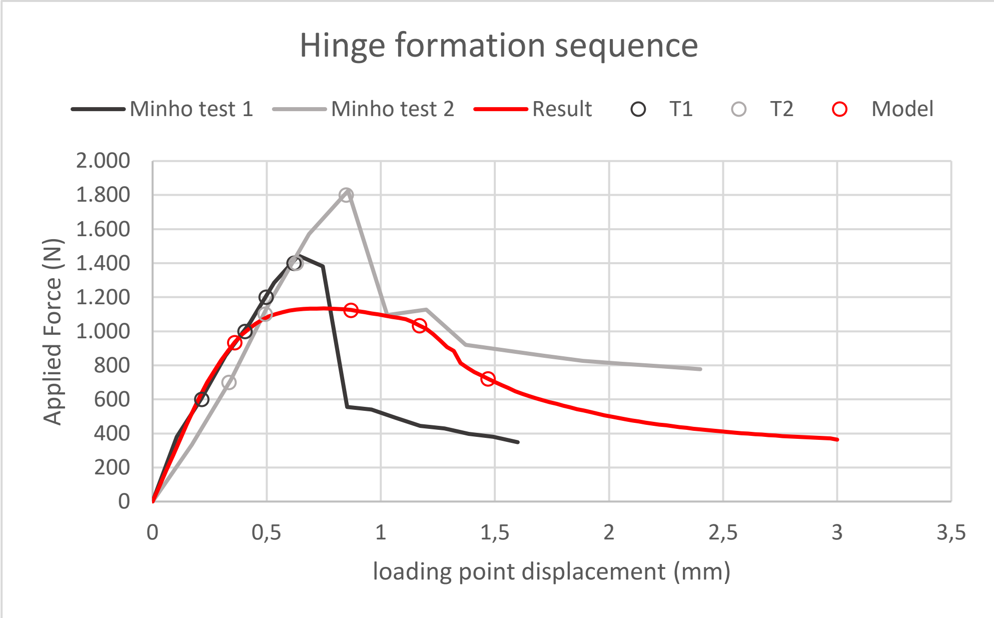

Figure 4.20: Total strain crack model, Hinge formation sequence

4.5.1.4. Discussion of results

The results from the macro model, presented in the previous section, show that the created model is close to the results from both tests. Taking a closer look at the linear part of the force-displacement curve, it can be seen that the slopes of both tests and model are equal, which was not the case in the numerical model presented in the paper (Figure 4.12(b)). As mentioned in Section 4.4.3, the Young's modulus determines this slope. This supports the assumption that the young's modulus should be taken from the masonry compressive tests and that a too high value was taken in the paper.

A difference between tests and model can be found investigating the post peak behaviour and peak load (Figure 4.15). The test results show that a brittle failure occurred, while in the model this is not the case. Another difference is found in the hinge formation sequence (Figure 4.20). In both tests, all four hinges were formed before the peak load was reached, whereas in the model this was not the case. It can however be observed that, in the macro model, all four hinges were formed before failure of the arch, which was also the case in the tests.

The above mentioned differences could be a result from the macro-modelling approach, as the cracks are smeared over the geometry and not localized in potential crack planes. However, a micro model is needed first to support this. It could also be the case that the properties used to represent the masonry are slightly different then in reality. In the paper the elastic and compressive properties were found experimentally, but the tensile properties were taken from previous works. By performing a parametric study on the tensile properties, the sensitivity to small changes of these properties can be investigated.

4.5.1.5. Parametric study

As mentioned, inaccurate tensile properties could be a reason for differences between the test and numerical results. In the following sections the sensitivity of the model to a change in in tensile strength and tensile fracture energy is investigated.

4.5.1.5.1. Tensile strength

The influence of a change in the tensile strength has to be investigated. To do so, three different tensile strengths are chosen and compared to the test results, shown in Figure 4.21. As the peak strength is not reached by the created macro model, only higher values for the tensile strength are considered, namely $f_{t,1} = 0.18\ MPa$; $f_{t,2} = 0.24\ MPa$ and $f_{t,3} = 0.30\ MPa$.

From the graph it can be seen that the change in tensile strength changes the peak load and also changes the post peak behaviour. The curve belonging to $f_{t,3}$ shows a more brittle behaviour after the peak load is reached, which was found in the tests also. Next to that, the found peak load is equal to the one observed in the first test series.

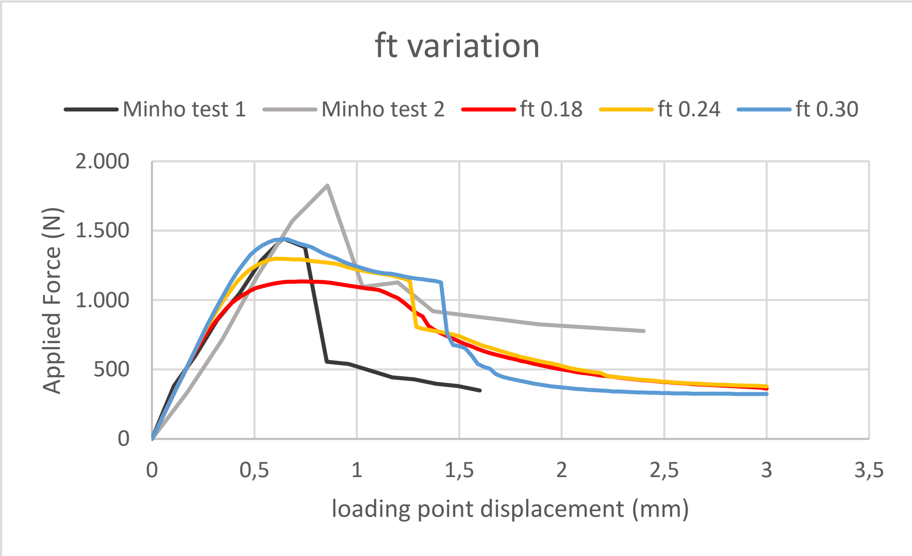

Figure 4.21: Total strain crack, tensile strength variation

4.5.1.5.2. Fracture energy in tension

The fracture energy determines the deformability of the material in tension. In order to investigate the influence of a change in fracture energy on the load-displacement curve, again 3 values will be chosen and compared to the test results (Figure 4.22). The chosen values for the tensile fracture energy are, $G^I_{f,1} = 0.03\ J/m^2$; $G^I_{f,2} = 0.01\ J/m^2$ and $G^I_{f,3} = 0.05\ J/m^2$.

The curves show that a change in the tensile fracture energy changes both the peak load and post peak behaviour of the arch. Taking a lower value results in a more brittle failure mechanism however, the peak load reduced significantly. The tests showed that brittle failure occurred, which is observed most for $G^I_{f,2}$.

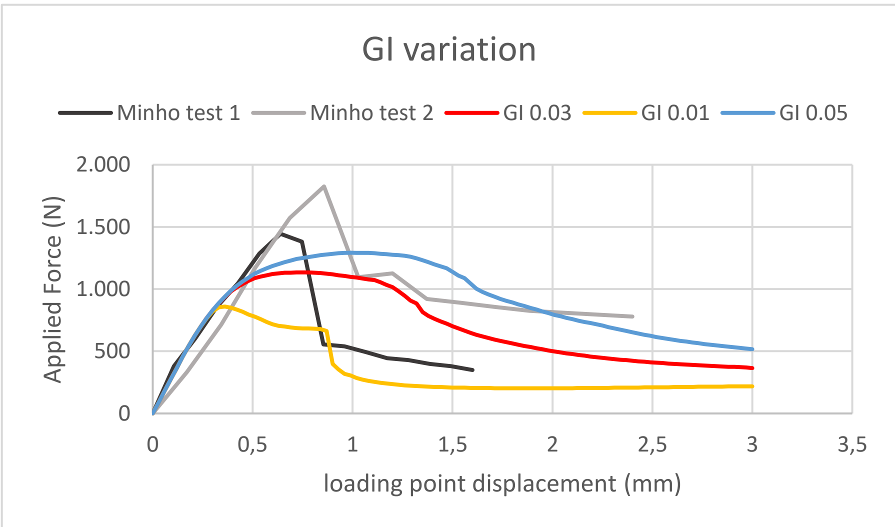

Figure 4.22: Total strain crack, fracture energy in tension variation

4.5.1.6. Calibrated model

The parametric study showed that a small change in tensile properties changes both the peak load and post peak behaviour. So, just a small difference between the actual values and the values used in the numerical model will change the reliability of the created model. With these findings, it is reasonable to assume that the tensile properties reported in the paper were taken to low. The model can be calibrated to the test results by taking a higher value for the tensile strength into account, shown in Figure 4.23. In this model a tensile strength of $f_t = 0.30\ MPa$ is used and a tensile fracture energy of $G_f^I = 0.03\ J/m^2$.

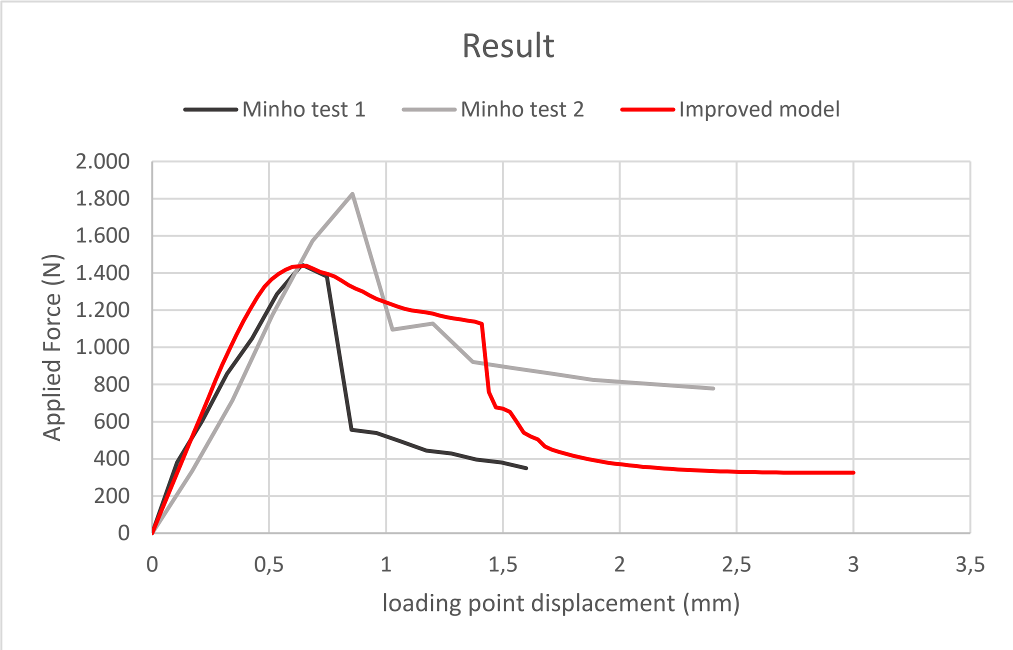

Figure 4.23: Total strain crack, calibrated force-displacement curve

4.5.2. Macro model - Engineering Masonry

4.5.2.1. Model description

The macro model that will be created follows the approach explained in Section 3.5. In short, masonry is modelled using the engineering masonry material model. This model assumes that cracks can only occur in predefined crack patterns perpendicular to the head and bed joint. The joints between the shapes represent the bed joints of the masonry.

The geometry of the model is similar to that of the previous macro model and is shown in Figure 4.24. All shapes are assigned a local element axis, the 'x' direction of the local axis is parallel to the mortar joint. Doing so, the joints between the shapes are now actually modelled as the bed joints and this value should be defined.

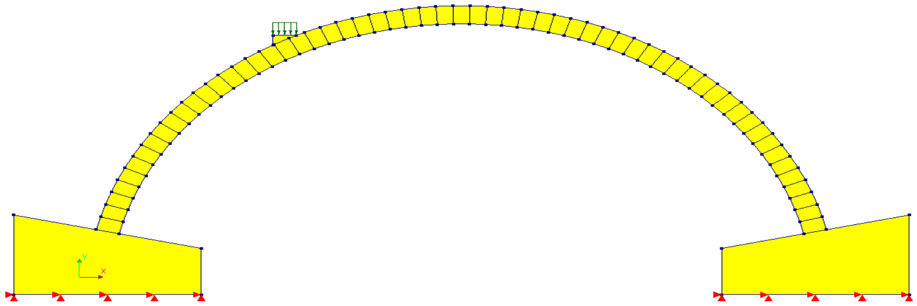

Figure 4.24: Macro model overview

4.5.2.2. Model properties

For the analysis it is chosen to follow the approach explained in Section 3.5. As mentioned, the Young modulus will be taken from the compressive test reported in Section 4.1.3, other values are taken to be similar to those reported in the paper (Basilio Sánchez, 2007).

Table 4-11: Engineering Masonry model, material properties

Masonry properties Engineering Masonry model		
Elasticity parameters		
Young's modulus	E_x E_y	$1020\ MPa$ $2040\ MPa$
Shear modulus	G_{xy}	$1750\ MPa$
Mass density	ρ	$2300\ kg/m^3$
Cracking parameters		
Head-joint failure type		Head-joint failure not considered
Bed-joint tensile strength	f_t	$0.18\ MPa$
Mode-I tensile fracture energy	$\mathrm{G_f^I}$	$0.03\ J/m^2$
Residual tensile strength		$0\ MPa$
Crushing parameters		
Compressive strength	f_c	$7.8\ MPa$
Compressive fracture energy	G_{fc}	$90\ J/m^2$
factor to strain at compressive strength		4
Unloading factor		Secant
Shear failure parameters		
Friction angle	φ	$0.75\ rad$
Cohesion	c	$0.3\ MPa$
Fracture energy in shear	G_f^{II}	$0.1\ J/m^2$
Crack bandwidth specification		*Rots*

4.5.2.3. Results

In the following figures the results of the performed analysis are given. Looking at the force displacement curve shown in Figure 4.25, it can be seen that the numerical model is able to come close to the tests results. A peak load of $1.28\ kN$ is calculated, which is close to the peak load of $1.44\ kN$ found in the first test series. The peak load is, however, achieved at a larger displacement. Next to that, the tests show a more brittle failure compared to the numerical model.

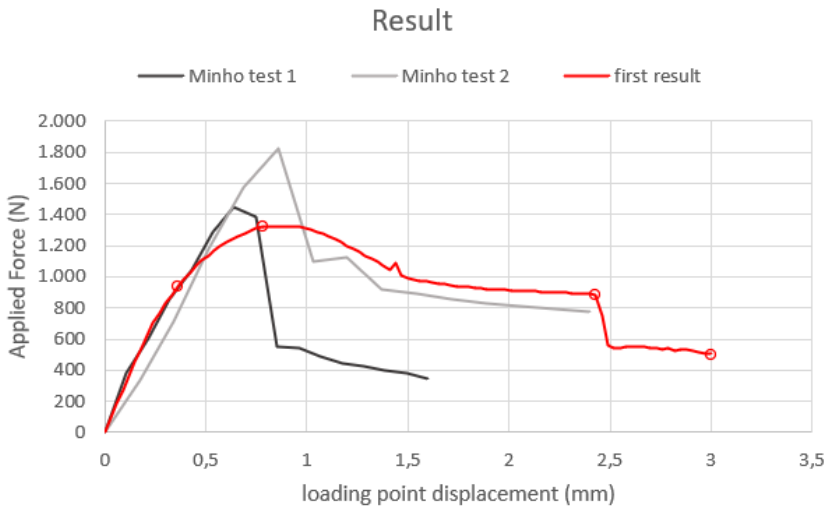

Figure 4.25: Engineering Masonry, force-displacement curve

Next to the load displacement curve, the results of the tests also reported the sequence of hinge formation. One of the benefits of using a numerical model, is that this hinge formation can be determined with great precision. As expected, the first crack occurred just below the loading point, shown in Figure 4.26. It can also be seen where the other cracks start to form, which is in line with the test observations. However, in the numerical model the first crack occurred in load-step 13, corresponding to a displacement of $0.36\ mm$ and a load of $940\ N$.

The second crack occurred in load-step 21 (Figure 4.27), corresponding to a displacement of $0.60\ mm$ and a load of $1224\ N$, which is the location of the peak load. The third hinge was formed in load-step 76 (Figure 4.28), corresponding to a displacement of $2.25\ mm$ and a load of $900\ N$. After the fourth and final hinge is formed, the arch fails. This happened in load step 85 (Figure 4.29), corresponding to a displacement of $2.52\ mm$ and a load of $546\ N$.

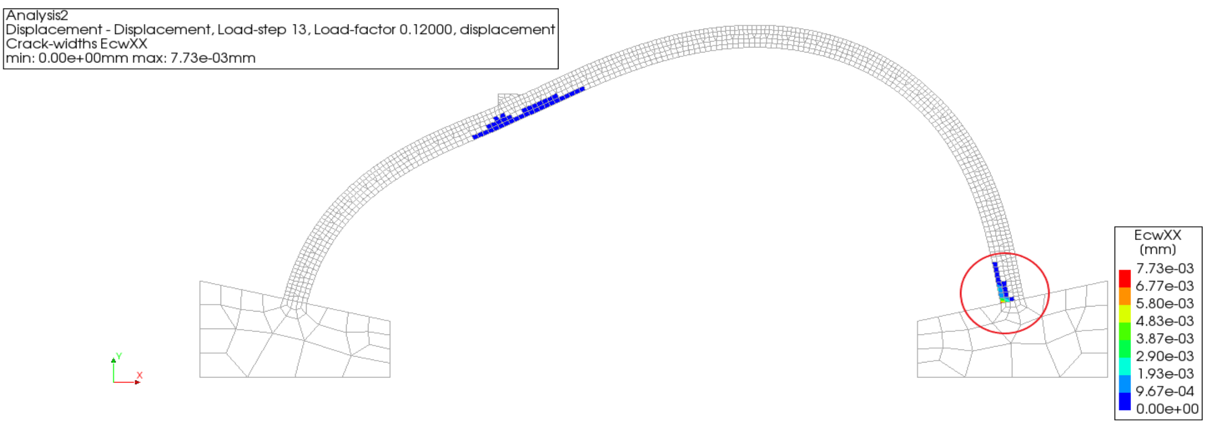

Figure 4.26: Engineering Masonry, location of first hinge

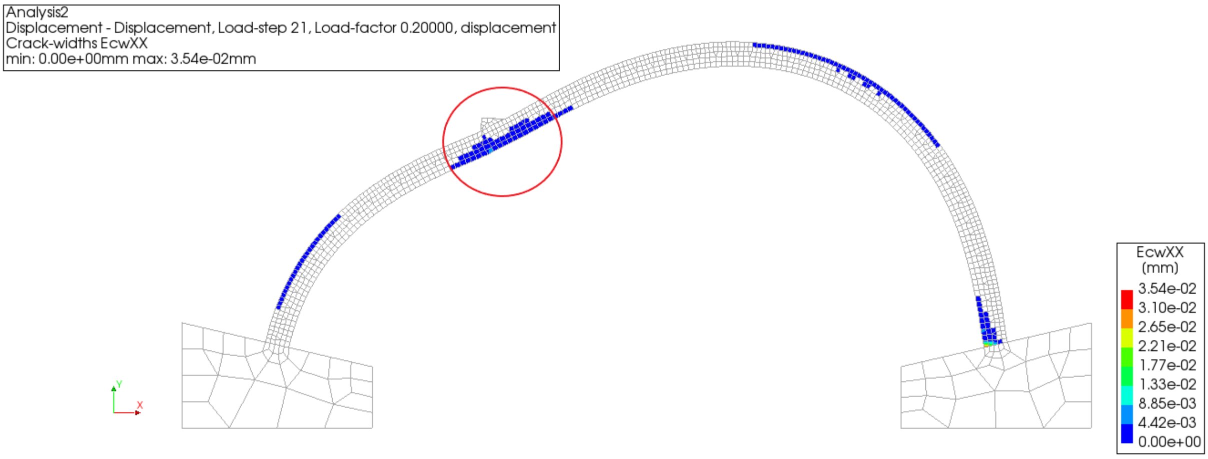

Figure 4.27: Engineering Masonry, location of second hinge

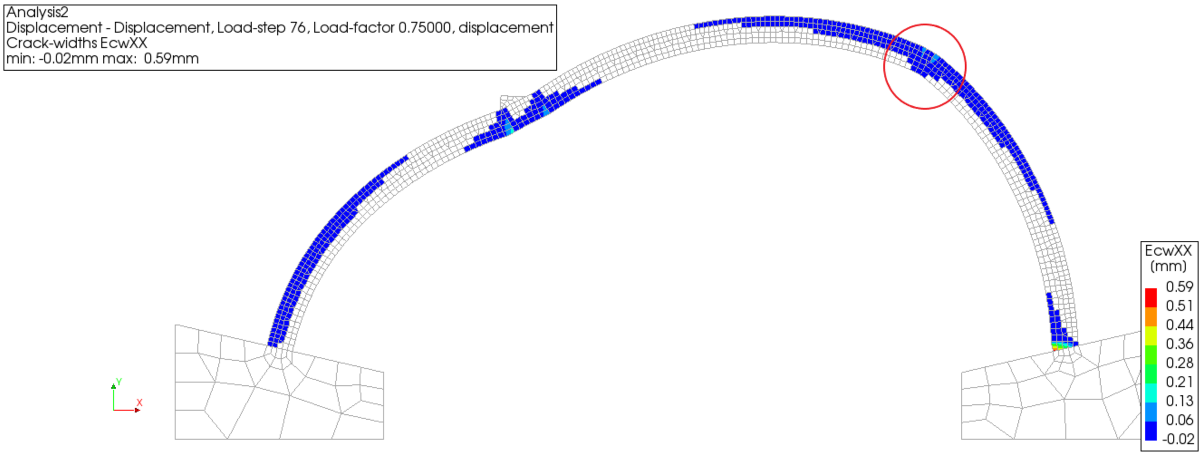

Figure 4.28: Engineering Masonry, location of third hinge

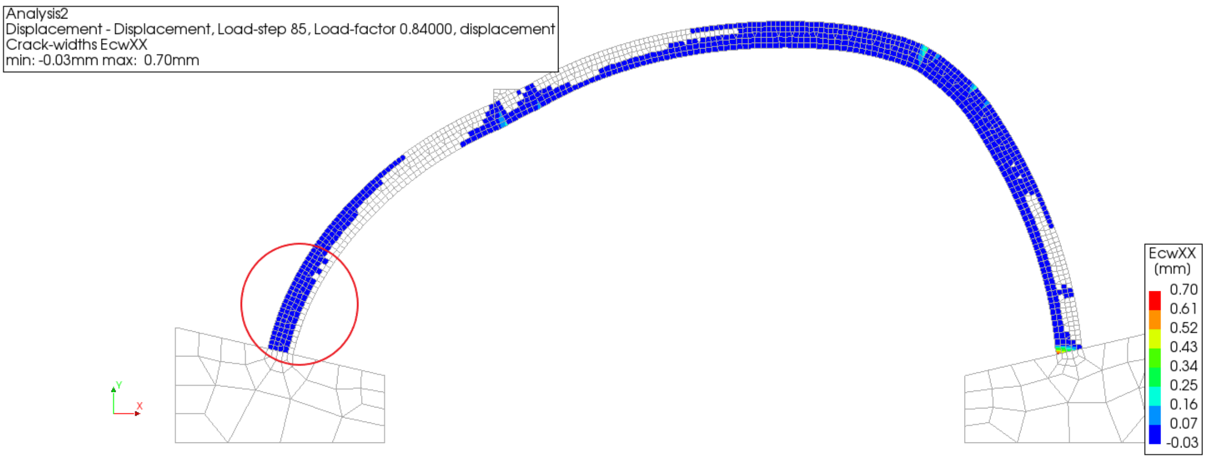

Figure 4.29: Engineering Masonry, location of fourth hinge

4.5.2.4. Discussion of results

The results from the engineering masonry model, presented in the previous section, show that the created model is close to the results from both tests. Next to that the curve also is very close to the one found with the total strain crack model in Section 4.5.1.3..

Similar to the findings of the total strain crack model, the post peak behaviour and the hinge formation sequence differs from the one obtained from the test. Again the post peak behaviour is less brittle compared to the test and only two hinges were formed before the peak load was reached. By performing a parametric study on the tensile properties of the model, the sensitivity of small changes can be investigated and a new calibrated model could be constructed.

4.5.2.5. Parametric study

The same parametric study as for the crack energy model, Section 4.5.1.5, will be performed in the following sections. So, investigating the tensile strength and tensile fracture energy.

4.5.2.5.1. Tensile strength

As the peak strength is not reached by the created macro model, only higher values for the tensile strength are considered, namely $f_{t,1} = 0.18\,MPa$; $f_{t,2} = 0.24\,MPa$ and $f_{t,3} = 0.30\,MPa$.

From the graph it can be seen that the change in tensile strength changes the peak load and also changes the post peak behaviour. The curve belonging to $f_{t,2}$ and $f_{t,3}$ show a more brittle behaviour after the peak load is reached, which was found in the tests also.

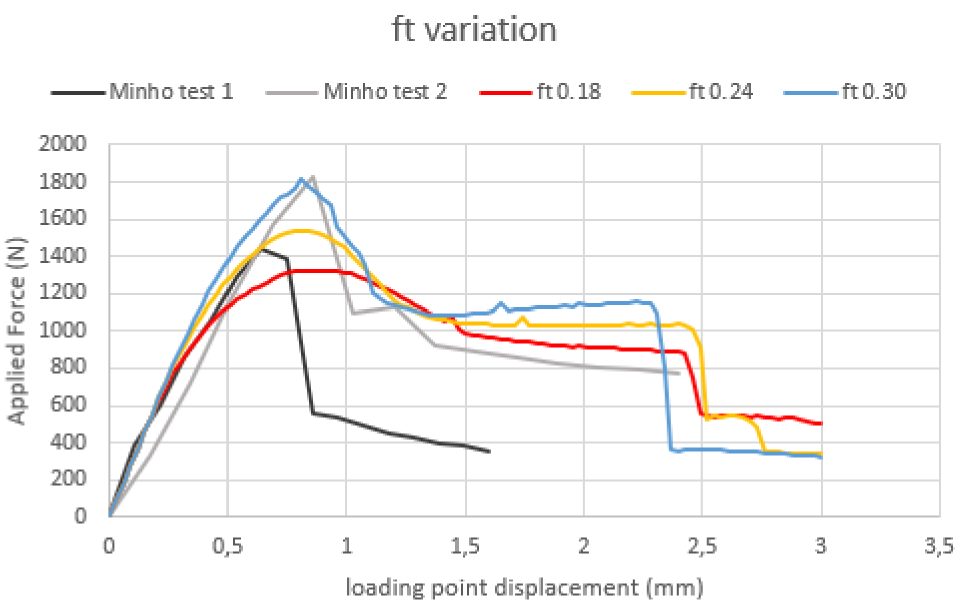

Figure 4.30: Engineering Masonry, tensile strength variation

4.5.2.5.2. Fracture energy in tension

In order to investigate the influence of a change in fracture energy on the load-displacement curve, again 3 values will be chosen and compared to the test results (Figure 4.22). The chosen values for the tensile fracture energy are, $G^I_{f,1} = 0.03\,J/m^2$; $G^I_{f,2} = 0.01\,J/m^2$ and $G^I_{f,3} = 0.05\,J/m^2$.

The curves show that a change in the tensile fracture energy changes both the peak load and post peak behaviour of the arch. Taking a lower value results in a more brittle failure mechanism, however, the peak load reduced significantly. The tests showed that brittle failure occurred, which is observed most for $G^I_{f,2}$.

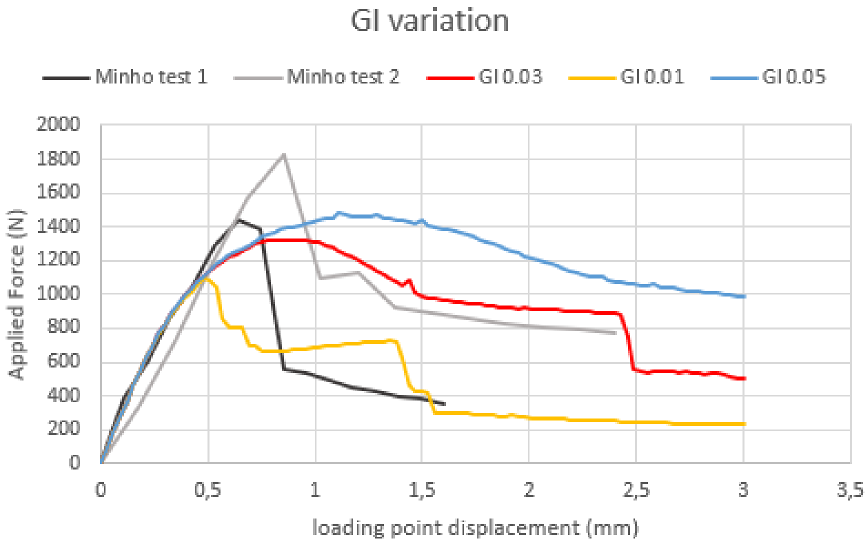

Figure 4.31: Engineering Masonry, fracture energy in tension variation

4.5.2.6. Calibrated model

The parametric study showed that a small change in tensile properties changes both the peak load and post peak behaviour. So, just a small difference between the actual values and the values used in the numerical model will change the reliability of the created model. With these findings, it is reasonable to assume that the tensile properties reported in the paper were taken to low. The model can be calibrated to the test results by taking a higher value for the tensile strength into account, shown in Figure 4.32. In this model a tensile strength of $f_t = 0.30\ MPa$ is used and a tensile fracture energy of $G_f^I = 0.03\ J/m^2$.

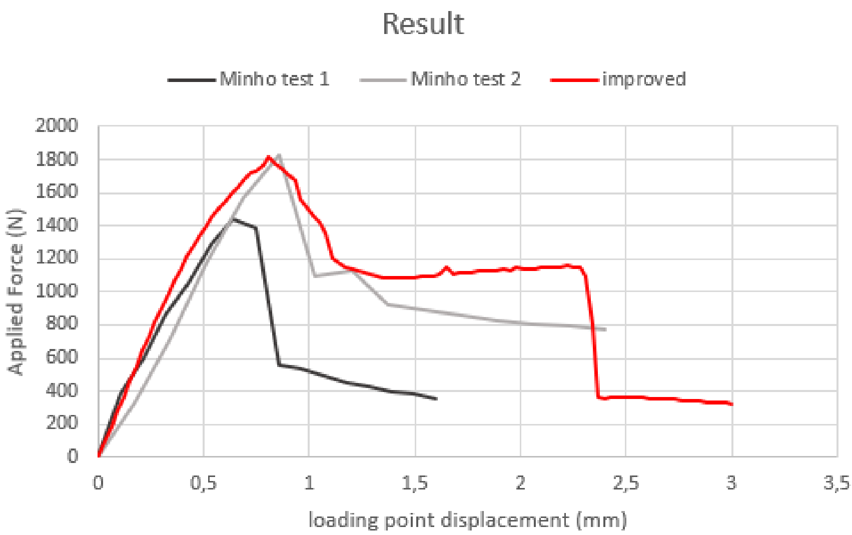

Figure 4.32: Engineering Masonry, calibrated

4.5.3. Comparison of macro models

In this section the result from the macro models presented in the previous sections will be compared, starting with the obtained first results shown in Figure 4.33. From this graph it can be seen that both models show a similar shape and that the engineering masonry model reaches a higher peak load. Although the models show a similar shape, the shape differs from the test results. During testing a sudden drop in the force displacement curve occurs, indicating a brittle failure. This could be caused by the hinge formation sequence found in the tests and models. For both tests four hinges were formed before reaching the peak load, creating an instable mechanism. In both created models, only two hinges were observed before reaching the peak load.

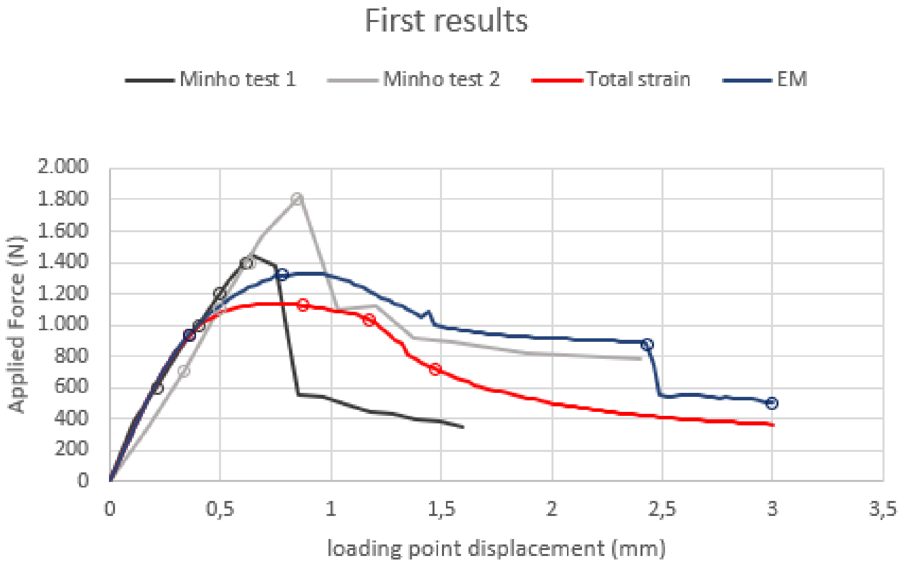

Figure 4.33: Macro models, first results

Next to the initial results, for both models a parametric study on the tensile properties is performed. This study showed that a change in either tensile strength or tensile fracture energy changes both the peak load and post peak behaviour. It was then found that by increasing the tensile strength, to a value of $f_t = 0.30\ MPa$, a result was found that is closer to test results, shown in Figure 4.34.

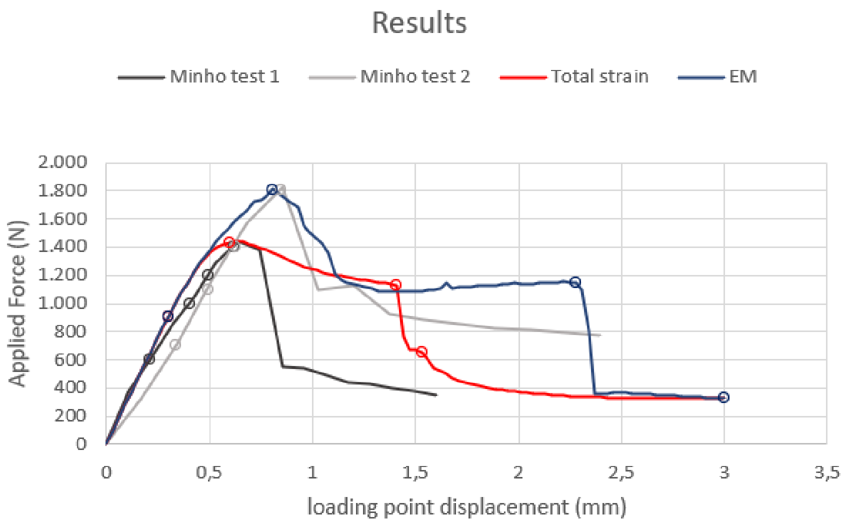

Figure 4.34: Macro models, calibrated

Looking at these calibrated results, a more brittle response is found for both models, however, there are still some differences. The engineering masonry model seems to capture the behaviour and strength of the second test series very accurately. For the total strain crack model this is slightly less the case, as the sudden drop in strength is observed later when the third hinge is formed. Again, both models only show the formation of two hinges before and two hinges after reaching the peak load. It is noteworthy to note that the sequence of hinge formation is slightly different in both models. For the total strain crack model the first hinge formed below the applied load and the second hinge formed at the right abutment, whereas for the engineering masonry model this was the other way around. This however doesn't influence the results.

When a four hinge mechanism is created it is expected that the arch will fully collapse, meaning that it is not possible to withstand any load. Taking a closer look at the test results, it can be seen that there is some residual strength of the arch after reaching the peak load. With this in mind, questions arise whether all four hinges were created before reaching the peak load.

Another unexpected result was found when comparing the crack widths for the two models, shown in Figure 4.19 and Figure 4.29. The spread in crack widths and the magnitude of these cracks seem to be larger for the engineering masonry model, which was not expected as this model makes use of predefined crack patterns and only bed-joint failure was considered.

Both models are capable of finding the peak load of the masonry arch and make a representation of the post peak behaviour. The engineering masonry is, however, more accurate compared to the total strain crack model. As discussed before, this material model takes the actual anisotropic behaviour of the masonry into account, which appears to give a better result.

4.5.4. Micro model

In this section a micro model will be constructed to find the level of detail that is added compared to a macro model. First a description of the model will be given and the results will be presented, after which a parametric study will be performed to determine the effect these changes have on the results and to calibrate it to come closer to the test results.

4.5.4.1. Model description

The micro model that will be created follows the approach explained in Section 3.5. In short, a simplified micro model is created where the units are modelled using a basic linear elastic material model and the discrete cracking material model is used to describe the interfaces. It is assumed that the behaviour in tension can be described using the nonlinear tension softening curve.

As the in the macro model the units were already modelled separately, this can be used as a basis for the micro model. Only structural line interface elements have to be added in between the units, shown in Figure 4.35.

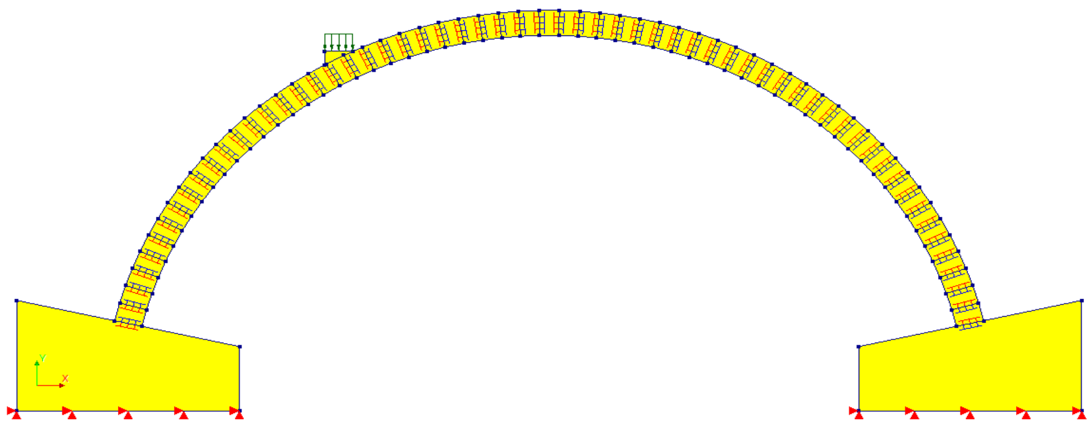

Figure 4.35: Micro model overview

4.5.4.2. Model properties

Following the approach from Section 3.5, there are two approaches to find determine the Youngs modulus. As the units now represent a composite material of brick and unit, it can be chosen to use the Young's modulus determined by the compressive tests or by formula 3.19. It is chosen to make use of the Young's modulus found in the compressive test on the masonry, equal to the one used in the macro model. The linear material properties to describe the units are given in Table 4-12.

Table 4-12: Micro model, unit properties

Masonry	*Linear material properties*
Young's modulus, E	$2040\ MPa$
Poisson's ratio, v	0.2
Mass density, ρ	$2300\ kg/m^3$

Next to the Young's modulus the stiffness properties of the interface elements have to be determined, using formula 3.20. Where it is chosen to use the Young's modulus defined above to be used to represent the units and the mortar Young's modulus taken from Section 4.1.2.2. The properties used to describe the interface elements are given in Table 4-13.

Table 4-13: Discrete cracking, interface properties

Interface properties discrete cracking		
linear material properties		
type		2D line interface
Normal stiffness modulus-y	k_n	$1663\ N/mm^3$
Shear stiffness modulus-x	k_s	$693\ N/mm^3$
Discrete cracking		
tensile strength	f_t	$0.18\ MPa$
Mode-I tension softening criterion		Exponential
Fracture energy	G_f^I	$0.03\ J/m^2$
Mode-I unloading reloading model		Secant
Mode-II shear criterion for crack development		Zero shear traction

4.5.4.3. Results

The results of the analysis are given in the figures below. Taking a closer look at the force displacement curve shown in Figure 4.36, it can be seen that the model is able to come close to the test result. A peak load of $1.31\ kN$ is obtained, which is close to the peak load in the first test series. However, the post peak behaviour is very different in the model compared to the tests.

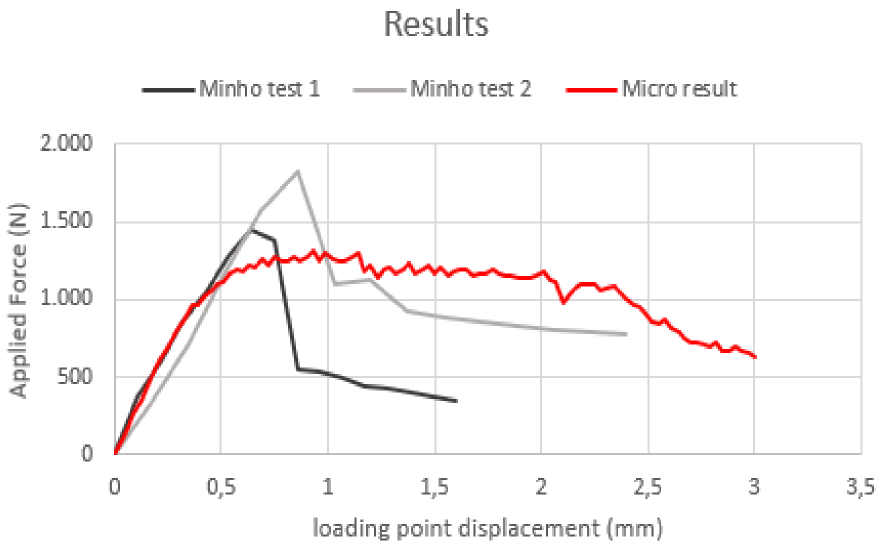

Figure 4.36: Micro model, force-displacement curve

Next to the load displacement curve, the results of the tests also reported the sequence of hinge formation. Similar to the results from the macro model, presented in section 4.5.1.3, the sequence of hinge formation is investigated.

Contrary tot the test results, the first hinge was formed at the right abutment, shown in Figure 4.37. This hinge was formed in load step 7, corresponding to a displacement of $0.18\,mm$ and a load of $525\,N$. The second hinge was formed right below the loading point in load-step 15 (Figure 4.38), corresponding to a displacement of $0.42\,mm$ and a load of $1014\,N$. The third hinge was formed in load-step 87 (Figure 4.39), corresponding to a displacement of $2.58\,mm$ and a load of $871\,N$. After the fourth and final hinge is formed, the arch fails. This happened in load step 101 (Figure 4.40), corresponding to a displacement of $3.00\,mm$ and a load of $632\,N$.

In Figure 4.41 the formation sequence of the hinges corresponding to the test and numerical results are shown in the load displacement curve. The hinges are shown with circular shapes on the curve.

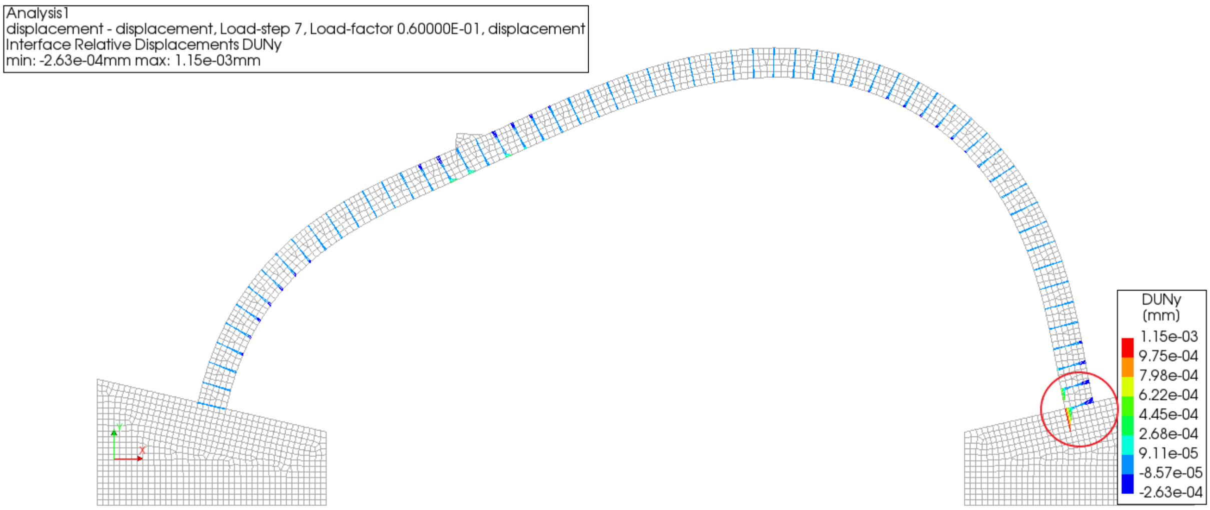

Figure 4.37: Mirco model, location of first hinge

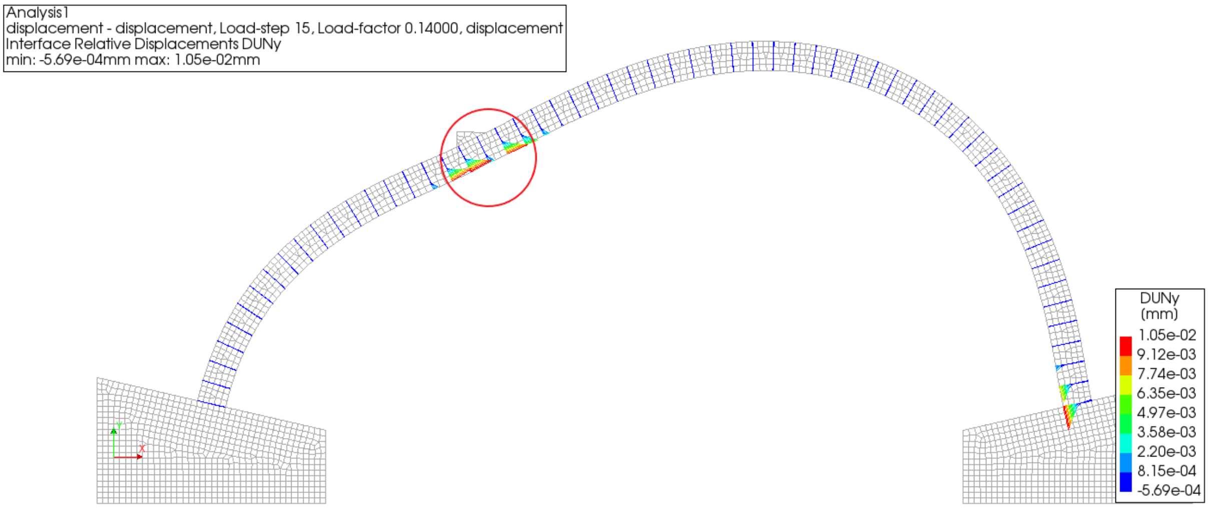

Figure 4.38: Mirco model, location of second hinge

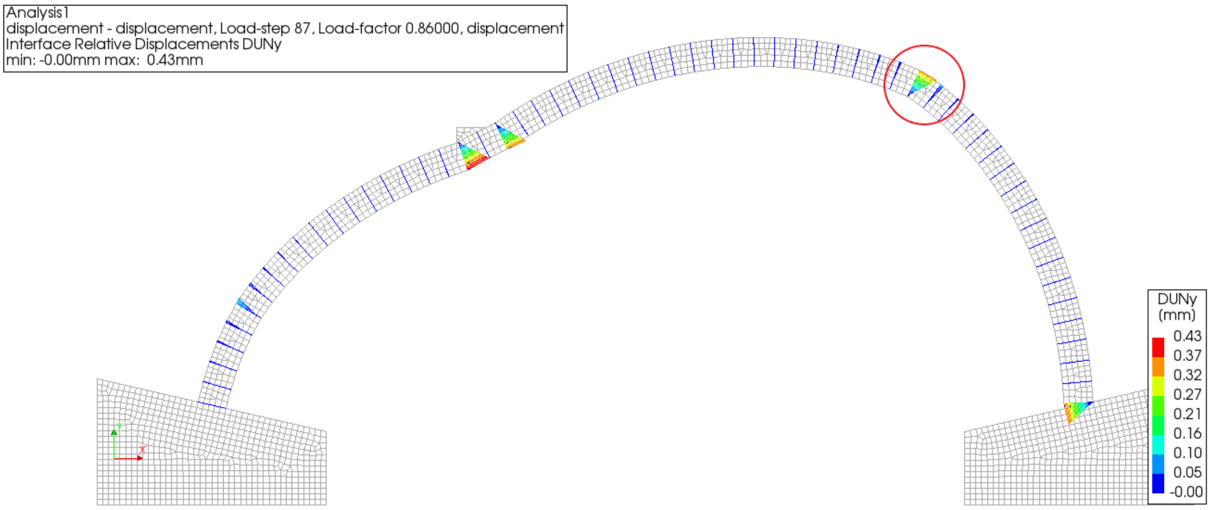

Figure 4.39: Mirco model, location of third hinge

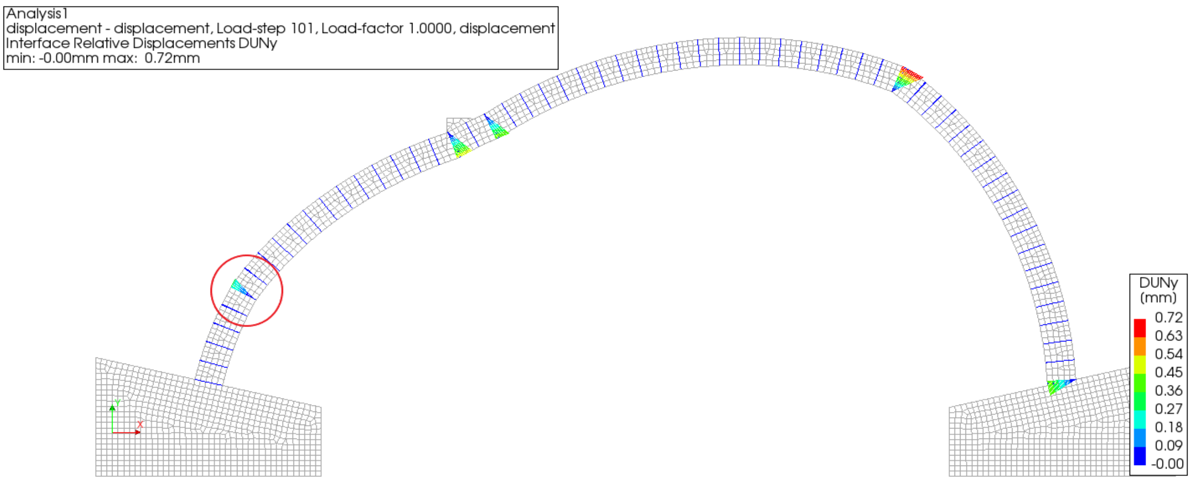

Figure 4.40: Mirco model, location of fourth hinge

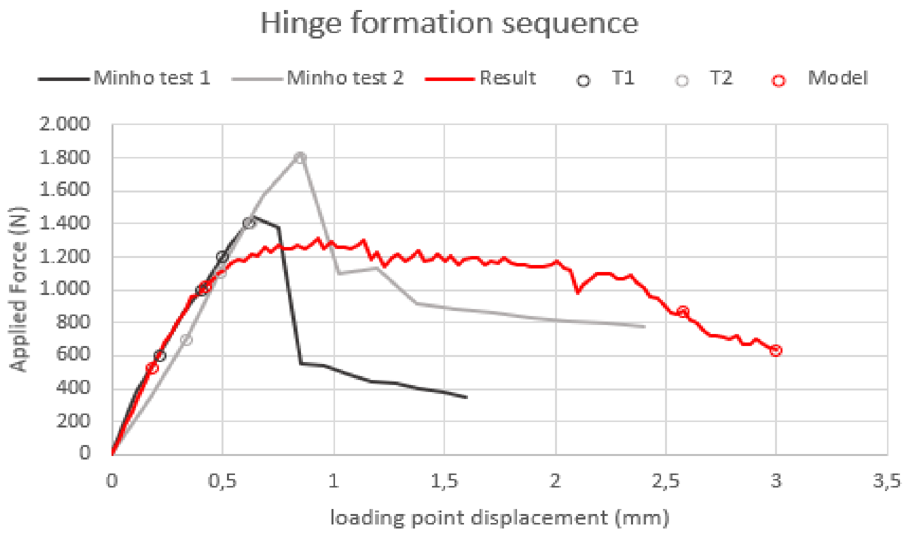

Figure 4.41: Mirco model, hinge formation sequence

4.5.4.4. Discussion of results

The results from the micro model, presented in the previous section, show that the created model can be used to analyse a masonry arch. Considering the linear part of the response, it can be noted that the slope of the model is similar to the slopes of both tests. This slope is determined by the stiffness of the interface elements and units. As the slopes are similar, it is reasonable to believe that equation 3.20 from Section 3.5.2 is an accurate tool to determine these properties.

A difference between tests and model can be found when taking a closer look at the post peak behaviour (Figure 4.36). The test results show that a brittle failure occurred, while in the model this is not the case. Another difference is found in the hinge formation sequence (Figure 4.41). In both tests, all four hinges were formed before the peak load was reached, whereas in the model this was not the case.

The above mentioned differences could be a result from the modelling approach, chosen material models or the used properties. If the properties used to represent the masonry and interfaces are slightly different then in reality, this could lead to differences. In the paper the elastic and compressive properties were found experimentally, but the tensile properties were taken from previous works. By performing a parametric study on the tensile properties, the sensitivity to small changes of these properties can be investigated.

4.5.4.5. Parametric study

Similar to the parametric study performed for the macro model, the impact of a small change in tensile properties is investigated. Next to the tensile properties, the stiffness of the interface is also investigated.

4.5.4.5.1. tensile strength

Similar to the investigation performed for the macro model (Section 4.5.1.5.1), three different values of the tensile strength are investigated. As the model did not reach the peak load obtained in the test, only higher values are investigated, namely $f_{t,1} = 0.18\ MPa$; $f_{t,2} = 0.24\ MPa$ and $f_{t,3} = 0.30\ MPa$. The first value is the value used in the initial model.

The results are plotted in a force-displacement curve, shown in Figure 4.42. Taking a closer look at the results, it can be seen that an increase in tensile strength will increase the peak load, but, does not influence the post peak behaviour.

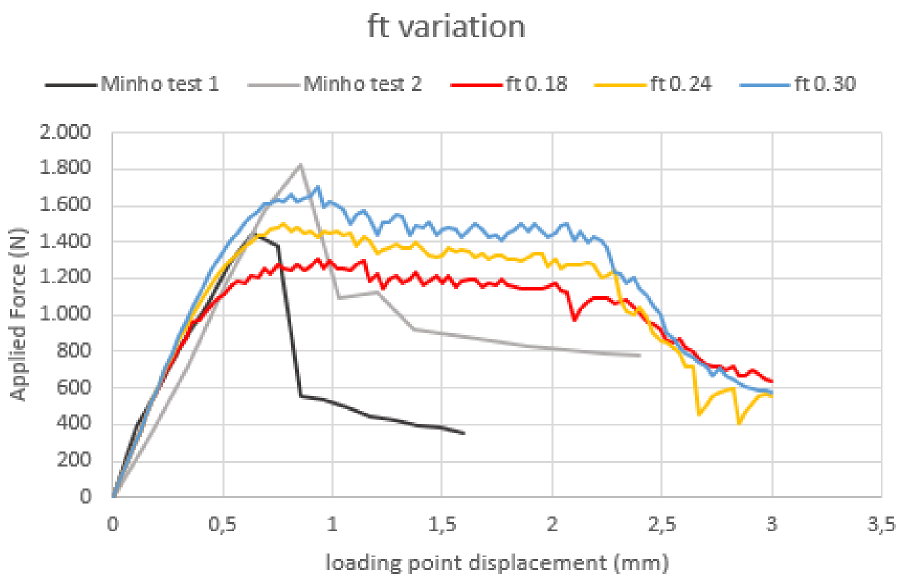

Figure 4.42: Micro model, tensile strength variation

4.5.4.5.2. Fracture energy in tension

In section 4.5.1.5.2 it was found that a change in fracture energy in tension will have significant consequences on the response for the macro model. In this section the influence of this change is checked for the micro model. Again the results of the analysis are shown in the figure below, together with the tests results. The chosen values for the tensile fracture energy are, $G_{f,1}^{I} = 0.03\, J/m^2$; $G_{f,2}^{I} = 0.01\, J/m^2$ and $G_{f,3}^{I} = 0.05\, J/m^2$.

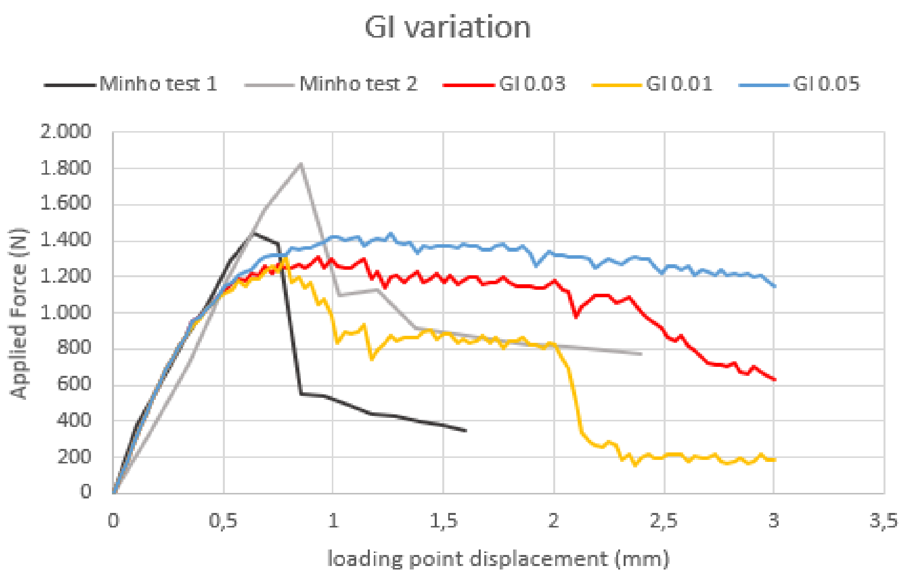

Figure 4.43: Micro model, fracture energy in tension variation

From these results it can be seen that a change in the tensile fracture energy does not result in a change in fundamental path as this is mostly given by compressive properties. The change in fracture energy only had significant impact on the post peak behaviour of the model, i.e. the peak load did not change due to the changes. The curve belonging to $G_{f,2}^{I}$ seems to capture the brittle behaviour of the response quite accurately.

4.5.4.5.3. Interface stiffness

The stiffness properties of the interface were determined in Section 4.5.4.2. In this calculation the Youngs modulus of obtained in the compressive test on the masonry specimen and mortar were used, Section 4.1.3 and Section 4.1.2 respectively. However, it is interesting to see what happens to the response when the Young's modulus and stiffness properties are taken from the brick and mortar compressive tests, from Section 4.1.1 and 4.1.2 respectively. By using equations 3.19 and 3.20, the Young's modulus and stiffness properties are obtained. Next to these stiffness properties, a third model is created using the stiffness properties reported in the paper. In Table 4-14 the Young's modulus and interface stiffness properties are given. The results of the change in stiffness are presented in the force-displacement curve in Figure 4.44. It can be seen that an increase in stiffness does not influence the response, however, decreasing the stiffness does change the response. It can also be noted that the results from the micro model, that uses the properties from the paper, completely different to the results reported in the paper.

Table 4-14: Micro model, interface stiffness properties

	Model 1	*Model 2*	*Paper*
Young's modulus, E	$2040\ MPa$	$1808\ MPa$	$5000\ MPa$
Normal stiffness, k_n	$1663\ N/mm^3$	$11935\ N/mm^3$	$24\ N/mm^3$
Shear stiffness, k_s	$693\ N/mm^3$	$4973\ N/mm^3$	$10\ N/mm^3$

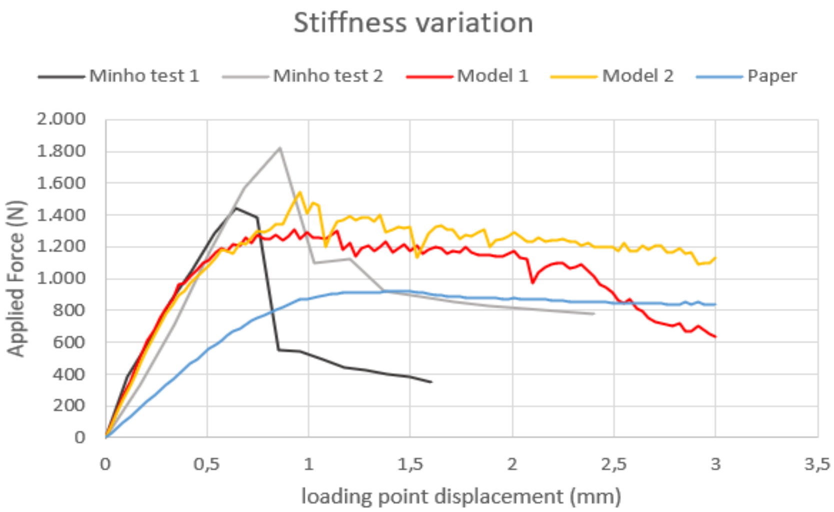

Figure 4.44: Micro model, stiffness variation

4.5.4.6. Calibrated model

The parametric study showed that a change in tensile strength changes the peak load and a change in tensile fracture energy changes the post peak behaviour. The initially created model, from Section 4.5.4.3, was not able to capture the actual post peak behaviour of the arch. By changing the fracture energy in tension, the description of the post peak behaviour can be improved. The results from section 4.5.4.5.2 showed that using a fracture energy in tension of $G_f^I = 0.01\ J/m^2$, made the response more brittle. To calibrate the model to the test results, this value will therefore be used. The initially found peak load is close to the one found in the first test series. The calibrated model is shown in Figure 4.45.

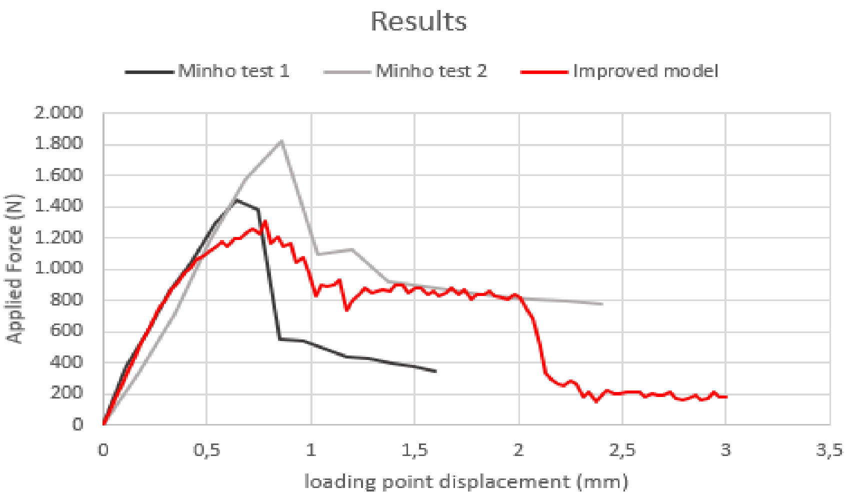

Figure 4.45: Mirco model, calibrated

4.5.5. Micro vs. Macro

In this section the results obtained with both the micro model and macro models are compared, starting with the initially obtained results shown in Figure 4.46. The macro models show a slightly more brittle post peak behaviour compared to the micro model, but, the overall shape of the curves are similar and neither of them really captures the brittle behaviour.

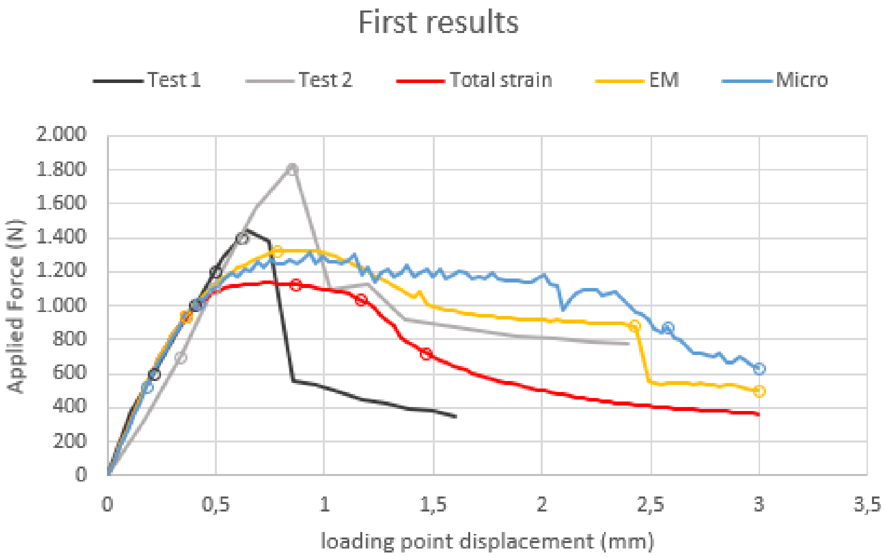

Figure 4.46: Macro vs Micro, first results

A difference is found when looking at the hinge formation sequence. In the total strain crack model the hinges are forming according to the tests, but, in the micro model and the engineering masonry model the first hinge is formed at the right abutment. This difference, however, does not influence the response of the model.

Taking a closer look at the crack widths and relative interface displacements, from Figure 4.40, Figure 4.29 and Figure 4.19, it is clear that the micro model is better in localizing the hinges. Which is also expected, as the interfaces represent these potential crack planes. However, the locations of the hinges are similar for all models. Both macro models show larger crack widths compared to the relative interface displacements from the micro model.

The biggest, and most interesting, difference is found when considering the impact of a change in tensile properties. In the macro models, a change of either the tensile strength or tensile fracture energy leads to both a change in peak load and post peak behaviour. For the micro model, a change in tensile strength only changes the peak load, and a change in tensile fracture energy only changes the post peak behaviour.

Another difference is found when improving the model to come even closer to the test results, all calibrated models are shown in Figure 4.47. To calibrate the models to the test results, the tensile strength was increased in both macro models, whereas this was achieved by reducing the tensile fracture energy in the micro model.

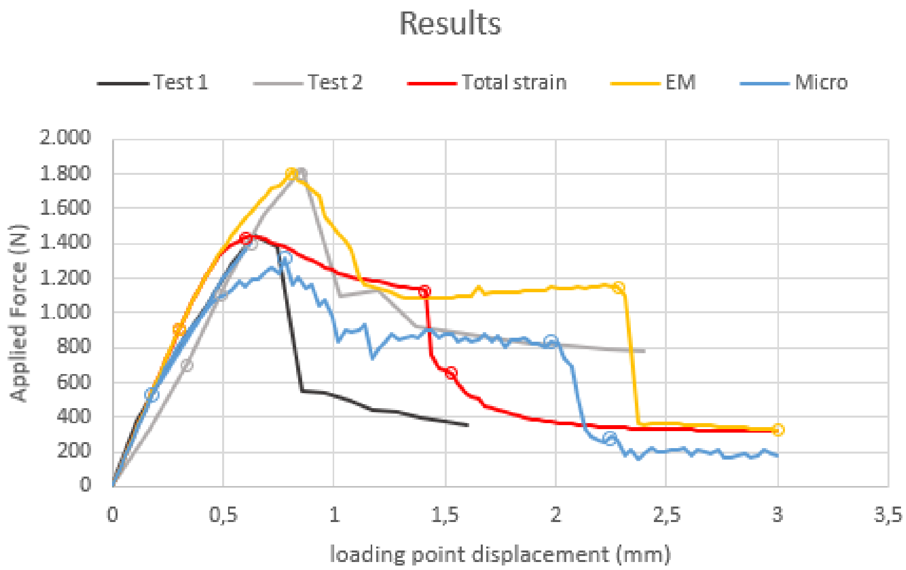

Figure 4.47: Micro vs. Macro, calibrated results

Looking at the curves, it can be seen that the micro model and the engineering masonry model show great resemblance. After the peak load is reached, a sudden drop in strength is observed, followed by a horizontal plateau and a sudden drop in strength again when the third hinge is formed. Both the micro - and the engineering masonry model make use of material models that represent the masonry as an anisotropic material, which makes these models close to reality. The total strain crack model shows a slightly different shape of the curve, only a sudden drop in strength is found when the third hinge is formed and not directly after the peak load.

5. Validation against masonry arch with backfill, Salford tests

At the university of Salford, United Kingdom (UK), research has been focused on the development of a large scale experimental facility for masonry arch bridges. This was done to gain more insight in the physical behaviour of masonry arch bridge structures in order to facilitate the development and validation of numerical analysis models (Ahmad, 2017). A test chamber was created that could exert both quasi static and cyclic loads. The overall objective of the physical model was to seek a compromise between investigating realistic behaviour, while limiting the complexity to enable study of the fundamental two dimensional behaviour of the system (Augusthus-Nelson L. , Swift, Melbourne, Smith, & Gilbert, 2018). After the development of this chamber, a series of tests were conducted to investigate the behaviour of damaged masonry arches. In order to investigate differences, the response of an undamaged masonry arch to a quasi static load was also investigated.

This test is chosen due to the overall objective of the tests, the clear description of the testing procedure and presentation of the results. Next to that, the company Witteveen+Bos used this test to try and validate the numerical programs, as mentioned in Section 1.1. In the following sections the test setup, mechanical properties and test results will be presented, after which a numerical model will be constructed.

5.1. Test setup

The arch geometry, test chamber and soil dimensions and the locations of the measuring instruments are shown in the figures below. The corresponding numerical values are given in Table 5-1.

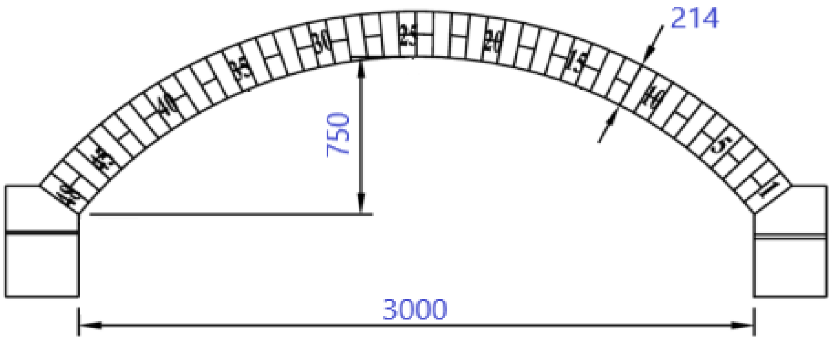

Figure 5.1: Salford test, arch geometry (Ahmad, 2017)

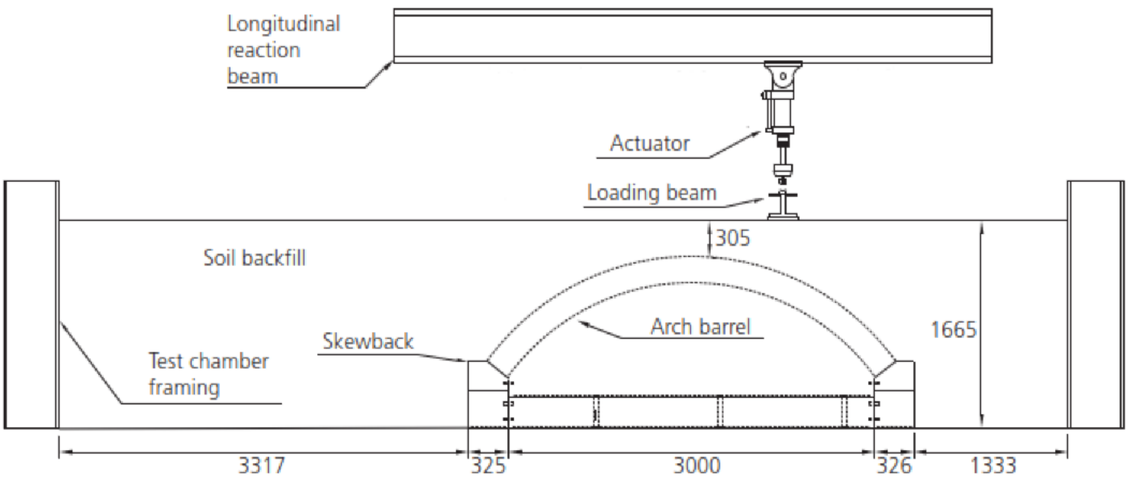

Figure 5.2: Salford test, test chamber side view (Augusthus-Nelson L. et al., 2018)

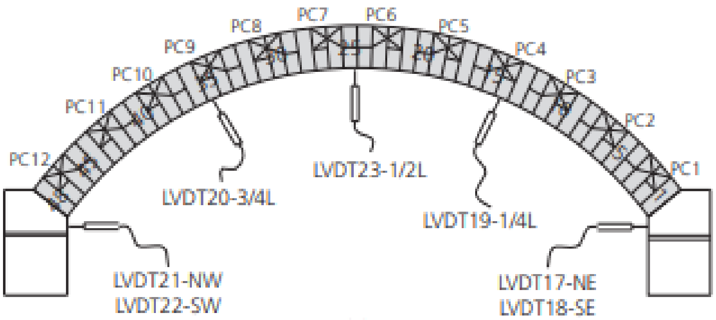

Figure 5.3: Salford test, locations of data inquisition instruments (Ahmad, 2017)

Table 5-1: Salford test, arch dimensions

shape	segmental		
span	3000 mm	abutment angle	36.9°
$\boldsymbol{n_{bricks}}$	48	brick dimensions	214*102*65 mm
Inner radius	1875 mm	Outer radius	2089 mm
Arch thickness	214 mm	Arch depth	1050 mm
Rise	750 mm		
Backfill depth (above crown)	305 mm		

As can be seen from the figure, the arch has a segmental shape with a header bonded execution of the masonry in order to eliminate ring separation failure. This arch was constructed inside a test chamber and backfilled with crushed limestone. After backfilling the centring was removed and the load was applied.

The test chamber itself was constructed using heavy duty steel I-sections to provide large stiffness. The walls of the chamber were treated to minimize friction in order to maintain plane strain conditions during the test. One of the principal requirements of the test chamber was the ability to monitor soil kinematics during testing. One of the longitudinal walls was constructed using acrylic sheets, in order to capture digital images of the soil movement (Augusthus-Nelson L. et al., 2018).

The abutments are executed in two parts of reinforced concrete, a base and a skewback. The base was bolted directly to the strong floor, creating fixed conditions. The skewback was connected with a horizontal mortar layer to the base, making it possible for the skewback to slide.

Crushed limestone was used as backfill material. It was placed and compacted in 120 mm thick layers in a controlled manner, so that the unit density of the material will be the same everywhere in the chamber.

In total three different masonry arches were tested, all with different loading conditions. As mentioned and shown in Figure 5.2, a cyclic and quasi static load can be applied by the servo-controlled hydraulic actuators. In two tests a cyclic load was applied to cause damage to the bridge, after which the bridge was loaded with a quasi static load to failure. The other test was performed to function as reference to compare the results of the damaged arches with and was therefore only subjected to a quasi-static load. This last test will be considered in this study.

The actuator has a maximum load capacity of $200\ kN$ and applies the load on a steel profile crossing the width of the arch. In this way the load is evenly distributed over the width and plane strain conditions are supported. The quasi-static load was applied in a displacement controlled manner at the most unfavourable position of the arch (quarter span), highlighted in Figure 5.2. Using the LVDTs and pressure cells (PC) shown in Figure 5.3 data is acquired and reported to a computer.

5.2. Mechanical properties

Prior to the tests, the used materials were analysed and subjected to various tests to determine the material properties, given in Table 5-2 (Augusthus-Nelson L. et al., 2018). These properties are useful for modelling purposes, however there are still some important properties missing.

Table 5-2: Salford test, mechanical properties (Augusthus-Nelson L. et al., 2018)

Properties		
Brick		
Density	ρ	$2226\ kg/m^3$
Water absorption		1.9 %
initial water absorption		$0.03\ kg/(m^2/min)$
Compressive strength	$f_{c,u}$	$176\ MPa$
Mortar		
compressive strength	$f_{c,m}$	$1.3\ MPa$
Density	ρ	$1470 - 1570\ kg/m^3$
Masonry		
Compressive strength	f_c	$25\ MPa$
fracture energy in compression	G_{fc}	$30\ J/m^2$
Limestone, crushed		
Cohesion	c_L	$3.3\ kPa$
Internal angle of friction	ϕ_L	54.5°
Unit weight	ρ	$20.0\ kN/m^3$

As mentioned, Witteveen+Bos have used this test to validate different numerical programs. Geotechnical engineers have determined and calculated the missing backfill properties. These properties were all reported in internal documents and are presented in Table 5-3 (Witteveen+Bos Raadgevende ingenieurs B.V., 2019)[5].

Table 5-3: Salford test, backfill properties by W+B (Witteveen+Bos Raadgevende ingenieurs B.V., 2019)[5]

Backfill properties - crushed limestone		
Weight	$\gamma_{unsat}/\gamma_{sat}$	$19.10\ kN/m^3$
Young's modulus	E	$20.83\ MPa$
Poisson's ratio	v	0.0
*Cohesion**	c	$7.0\ kPa$
*Internal angle of friction**	ϕ_L	40^o
Dilatancy angle	ψ	0^o
Friction between soil and masonry	R_{inter}	0.66

* According to the Salford test, the backfill material has a cohesion of 3.3 kN/m^2 and an internal angle of friction of 54.5°. However, physically speaking, is an internal friction angle greater than 45^o not possible. It is therefore more likely that the cohesion is greater than reported. A sensitivity study showed that using a cohesion of $7.0\ kN/m^2$ and an internal friction angle of 40^o will give similar results.

For the masonry arch, only the compressive strength and fracture energy in compression are given. In order to make a numerical model, more information regarding the behaviour of the masonry in tension and shear is needed. These values can be taken from the Dutch guidelines for the assessment of the

[5] Source from the intranet of Witteveen+Bos (not publicly accessible).

structural safety of buildings in case of erection, reconstruction and disapproval, and shown in Table 5-4 (NPR 9998:2020, 2020).

Table 5-4: Masonry properties, after 1945 (NPR 9998:2020)

Masonry properties		
Young's modulus	E	$6000\ MPa$
Shear modulus	G	$2500\ MPa$
Poisson's ratio	v	0.2
Compressive strength	f_c	$10.0\ MPa$
Compressive fracture energy	G_c	$15\ J/m^2$
Tensile strength	f_t	$0.2\ MPa$
Tensile fracture energy	G_f^I	$0.01\ J/m^2$
Shear strength	τ_{max}	$0.3\ MPa$
Shear fracture energy	G_f^{II}	$0.2\ J/m^2$

5.3. Experimental results

The results are given as a force-displacement curve below the loaded section, shown in Figure 5.4. Using particle image velocimetry equipment, the soil movement was analysed during the tests as shown in Figure 5.6. It was found that the arch eventually failed under a load of 141 kN due to the formation of a four hinge mechanism. The locations of the hinges are shown in Figure 5.5.

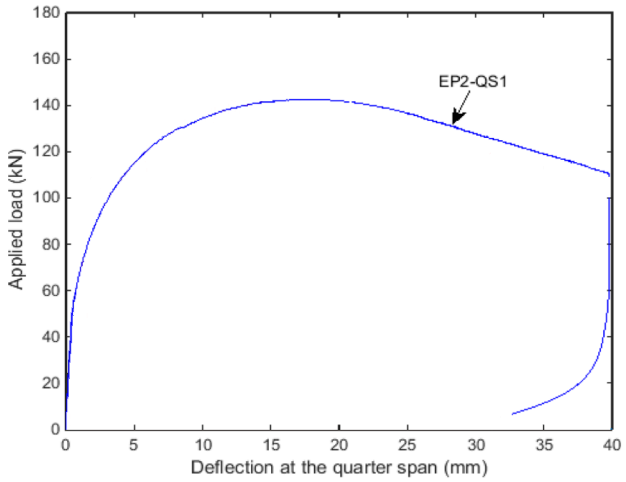

Figure 5.4: Salford test, results (Augusthus-Nelson & Swift, 2020)

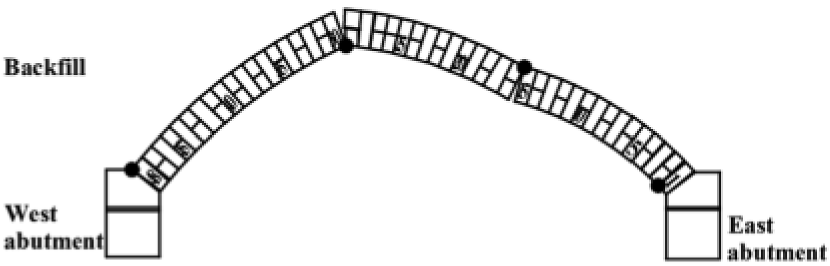

Figure 5.5: Salford tests, failure mechanism (Ahmad, 2017)

Figure 5.6: Salford test, particle image velocimetry output from start test until maximum load (Ahmad, 2017)

5.4. Modelling of Salford test

In the following sections numerical models for the Salford test will be created. As mentioned, the test was set up in such a way that plane strain conditions were created. Due to the plane strain conditions it is not possible to make use of the engineering masonry material model. Therefore, only one macro model, based on a total strain crack material model, and micro model will be created.

5.4.1. Macro model - Total strain crack

5.4.1.1. Model description

The macro model that will be created follows the approach explained in Section 3.5. In short, masonry is modelled using the total strain based crack model with a fixed crack orientation and the backfill is modelled using the Mohr-Coulomb material model. It is assumed that the behaviour in tension can be described using an exponential curve and in compression using a parabolic curve. The interaction between the backfill and the arch is modelled using Coulomb-friction interface elements.

Using the geometry and boundary conditions given in Section 5.1, the model is created as shown in Figure 5.7. Similar to the Minho test, the arch is modelled using multiple, perfectly connected, shapes with all different local element axis. The load is applied as a prescribed deformation at quarter span. This load is applied as a point load in combination with a tying set over a length of $203\ mm$, where the displacements in vertical direction are equal. This doesn't influence the results or applied load, but makes analysing results easier.

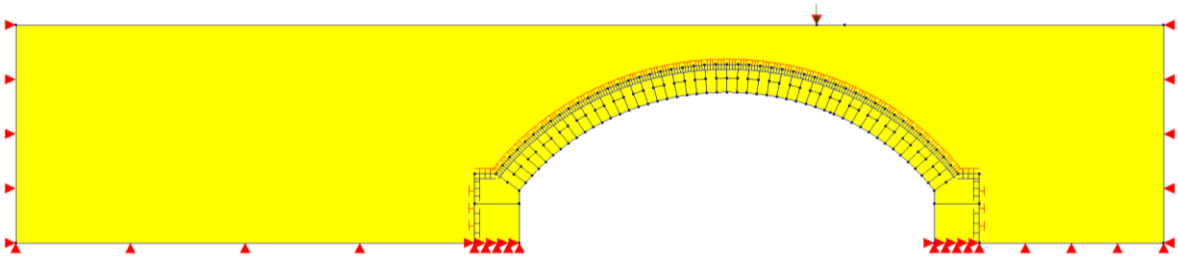

Figure 5.7: Macro model, initial

5.4.1.2. Model properties

The material properties used in the model are given in the tables below. It is chosen to make use of the backfill properties determined by Witteveen+Bos, Table 5-3, and the masonry properties given Table 5-4. This is done, due to the lack of supporting material test data. As now all properties are assumptions, the impact of a change in those properties has to be investigated. This investigation also contains the properties as reported by the researchers.

Table 5-5: Macro model, Mohr-Coulomb backfill properties

Backfill properties Mohr-Coulomb		
linear material properties		
Young's modulus	E	$20.83\ MPa$

Poisson's ratio	v	0
Mass density specification		Saturated density
Density	ρ	$2000\ kg/m^3$
Mohr-Coulomb and Drucker-Prager plasticity		
Plasticity model		Mohr-Coulomb plasticity
Cohesion	c	$7\ kPa$
Friction angle	ϕ	40^0
Dilatancy angle	ψ	0^0
Friction hardening		Constant friction angle
Tension cut-off		based on mean stress
Tension cut-off value	p_t	$2\ kPa$
Initial stress		
Lateral pressure ratio		Effective stresses - Isotropic
	K_0	0.7

Table 5-6: Macro model, total strain crack masonry properties

Masonry properties total strain based crack model		
Linear material properties		
Young's modulus	E	$6000\ MPa$
Poisson's ratio	v	0.2
Mass density	ρ	$2370\ kg/m^3$
Total strain based crack model		
crack orientation		Fixed
Tensile behaviour		
tensile curve		Exponential
Tensile strength	f_t	$0.20\ MPa$
Mode-I tensile fracture energy	$\mathrm{G_f^I}$	$0.01\ J/m^2$
crack bandwidth specification		Rots
Residual tensile strength		$0\ MPa$
Poisson's ratio reduction		No reduction
Compressive behaviour		
Compression curve		Parabolic
Compressive strength	f_c	$10\ MPa$
Compressive fracture energy	G_{fc}	$15\ J/m^2$
reduction due to lateral cracking		No reduction
Stress confinement model		No increase
Shear behaviour		
Shear retention function		Constant
Shear retention		0.01

Table 5-7: Macro model, Coulomb friction soil-structure interface properties

Interface properties Coulomb friction	
linear material properties	
type	2D line interface

Normal stiffness modulus-y	k_n	$1000\ N/mm^3$
Shear stiffness modulus-x	k_s	$10\ N/mm^3$
Coulomb friction		
Cohesion	c	$5.6\ kPa$
Friction angle	ϕ	$34°$
Dilatancy angle	ψ	$0°$
Interface opening model		Tension cut-off
Tensile cut-off value	p_t	$2\ kPa$

5.4.1.3. First results

The results of this model are given as a force-displacement curve, shown in Figure 5.8. A peak load of $52.1\ kN$ is calculated, while during the test a peak load of $141\ kN$ was obtained. Next to the force-displacement curve, the displacements, plastic strains, compressive stress in the backfill and crack-widths at the peak load are shown.

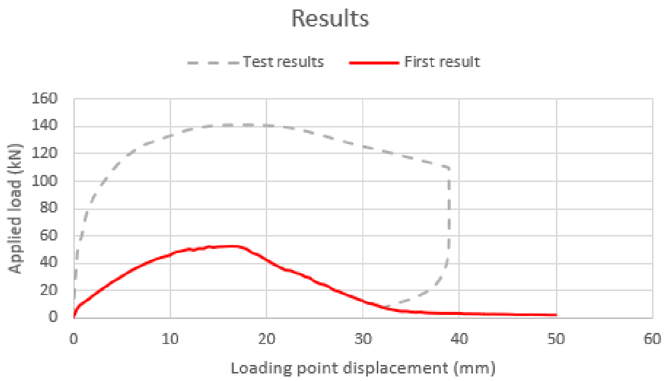

Figure 5.8: Macro model, initial first results

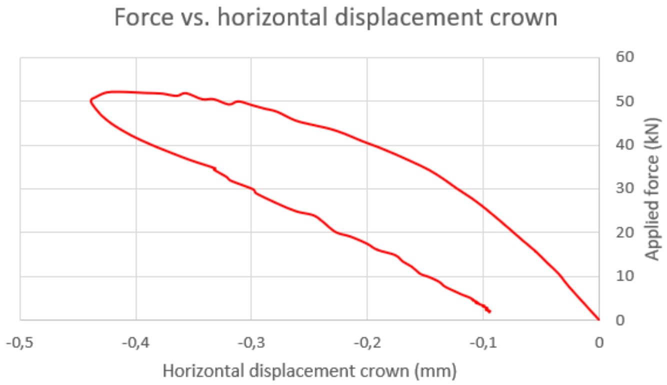

Figure 5.9: Macro model, horizontal displacement crown

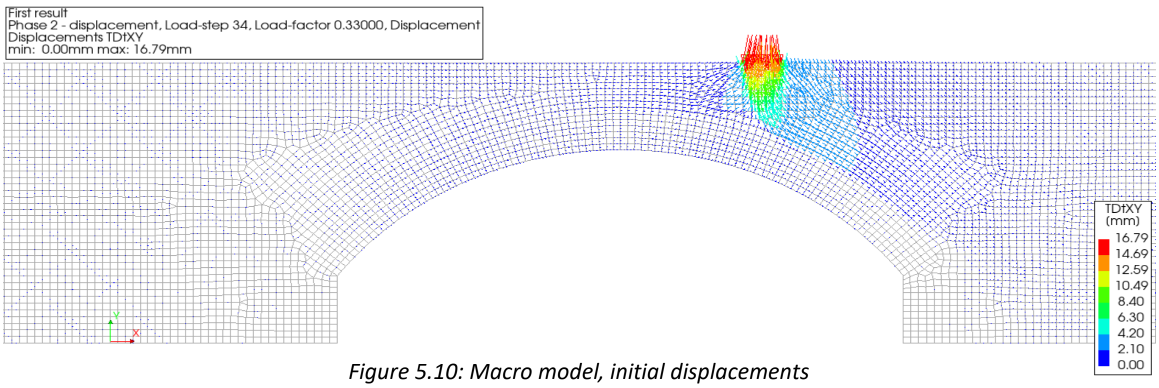

Figure 5.10: Macro model, initial displacements

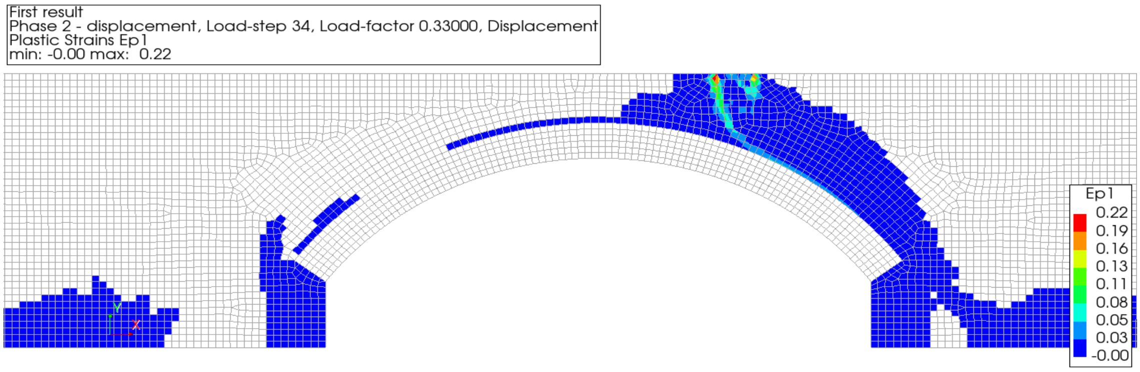

Figure 5.11: Macro model, initial plastic strains

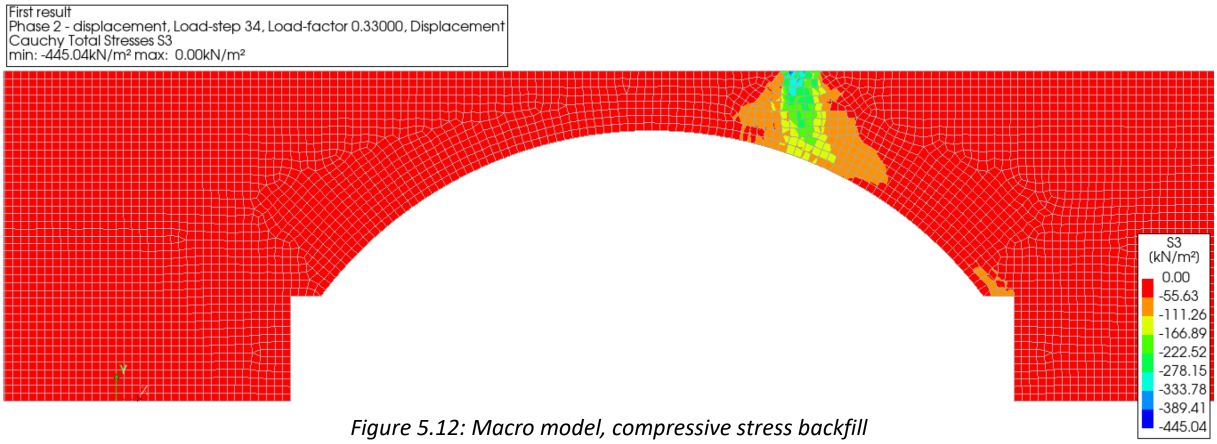

Figure 5.12: Macro model, compressive stress backfill

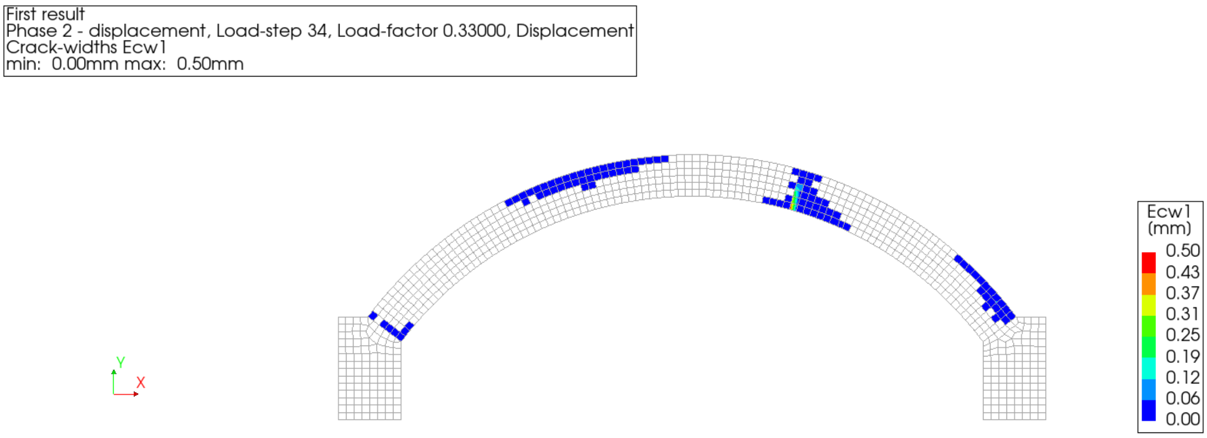

Figure 5.13: Macro model, crack-widths masonry arch

An extra analysis was performed where the load was applied in a forced controlled manner.

5.4.1.4. Discussion of results

The presented results show that this model is not able to represent the behaviour of the masonry arch bridge. Considering the force-displacement curve shown in Figure 5.8, it can be observed that the initial slope of the response, the peak load and post-peak behaviour differ from the test results. As mentioned before, the used properties are assumptions. They were not extensively reported in the supporting papers. Whether these assumptions lead to the inaccurate results can be determined by performing a parametric study.

However, prior to performing the parametric study, it is also important to know what failure mode is occurring. With that knowledge, an approach for the parametric study can be determined based on the governing failure mode and material. The plastic strains in the backfill, Figure 5.11, show that these plastic strains are large below the applied load, indicating that the backfill fails locally. This is supported by investigating the displacements, compressive forces and the crack-widths in the masonry arch, shown in Figure 5.10, Figure 5.12 and Figure 5.13, respectively. The displacements and compressive stress in the backfill are large directly below the loading points and the crack-widths in the masonry arch are small. Although there are cracks visible at the locations where hinges are expected, no mechanism has been formed. considering the horizontal displacements from the crown of the arch, Figure 5.9, it can be noticed that a very small horizontal displacement is found and that the arch moves back to almost the original position. Next to this, the parametric study presented in Appendix A shows that any change in masonry properties will not effect the global behaviour of the bridge. Hence, local failure of the backfill is occurring.

In the test a four hinge mechanism was pointed out to be the governing fail mode. Next to that, as stated in Section 2.2.4, a four hinge mechanism is usually the cause of failure. Therefore it was not expected that the local failure of the backfill was the governing failure mode. The behaviour of backfill is complex and is influenced by the behaviour of the backfill on micro scale. Due to the introduced load, relatively high compressive stresses are introduced which cannot be calculated by the program. This is one of the shortcomings of the material model implemented in DIANA. This phenomenon will not be investigated into depth, instead a small area below the load will be given linear elastic properties. By doing so, it is assumed that this area cannot fail and the load is spread over a wider area.

5.4.1.5. Adapted model

The adapted model is shown in Figure 5.14, where the highlighted part is the area where linear material properties are applied. The slope of the sides is equal to that of the internal friction angle of the soil and the height of the area is similar to the loading width. The properties used in this model will be similar to those given in Section 5.4.1.2, after which a parametric study will be performed.

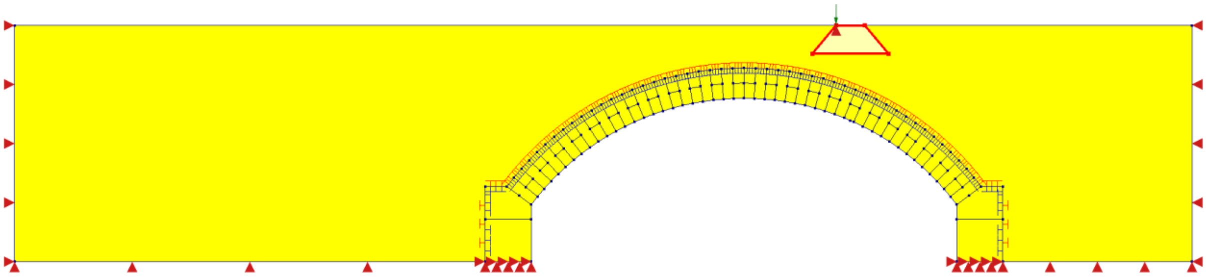

Figure 5.14: Macro model, adapted model geometry

5.4.1.6. First results adapted model

The results of this model are given as a force displacement curve, shown in Figure 5.15. A peak load of $103.6\ kN$ is calculated, while during the test a peak load of $141\ kN$ was obtained. Next to the force-displacement curve, the displacements, plastic strains, stress and crack-widths at the peak load are shown in Figure 5.17 to Figure 5.22.

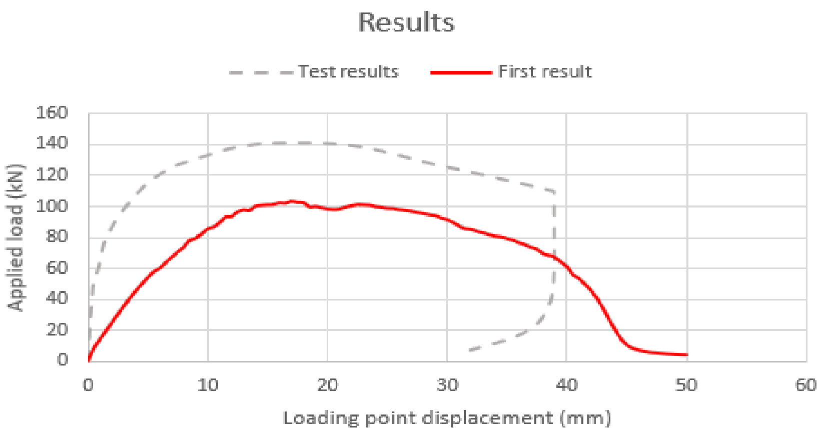

Figure 5.15: Macro model, force-displacement curve

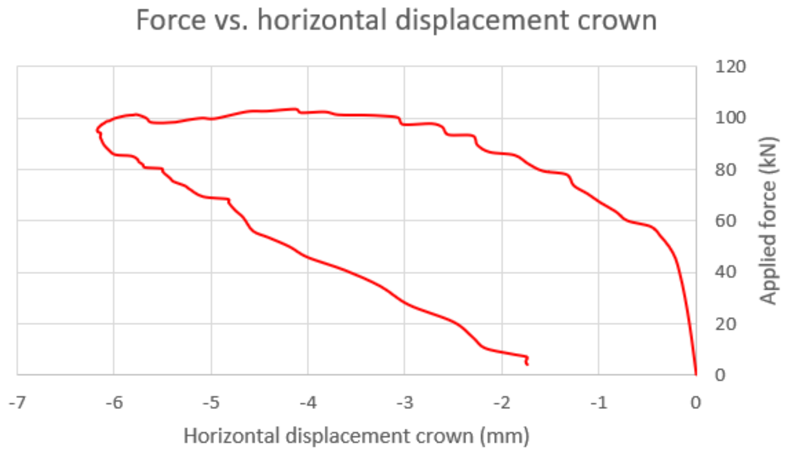

Figure 5.16: Macro model, horizontal displacement crown

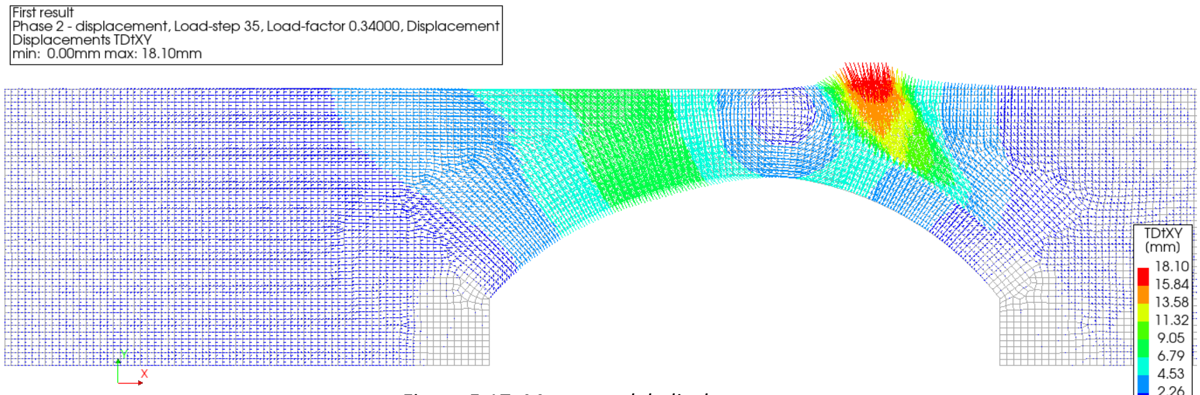

Figure 5.17: Macro model, displacements

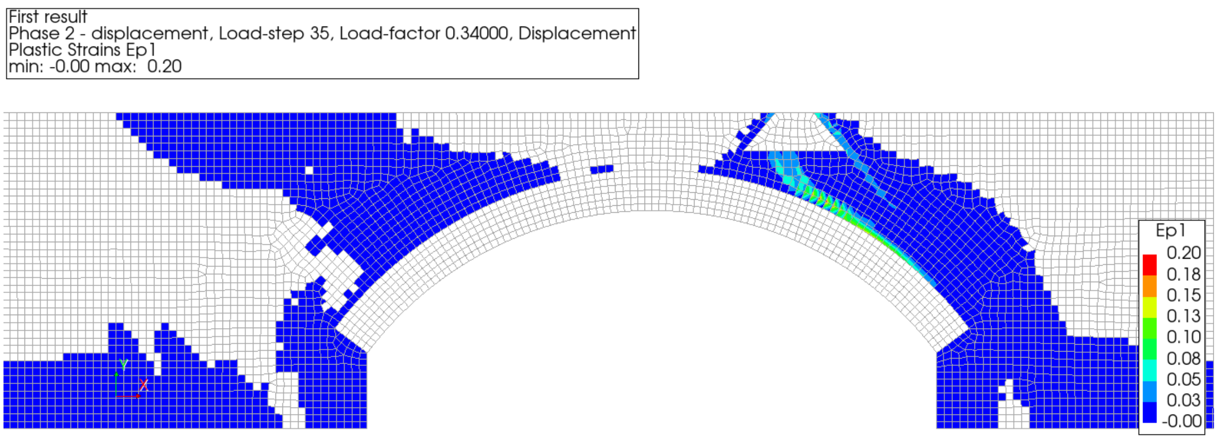

Figure 5.18: Macro model, plastic strain at peak load

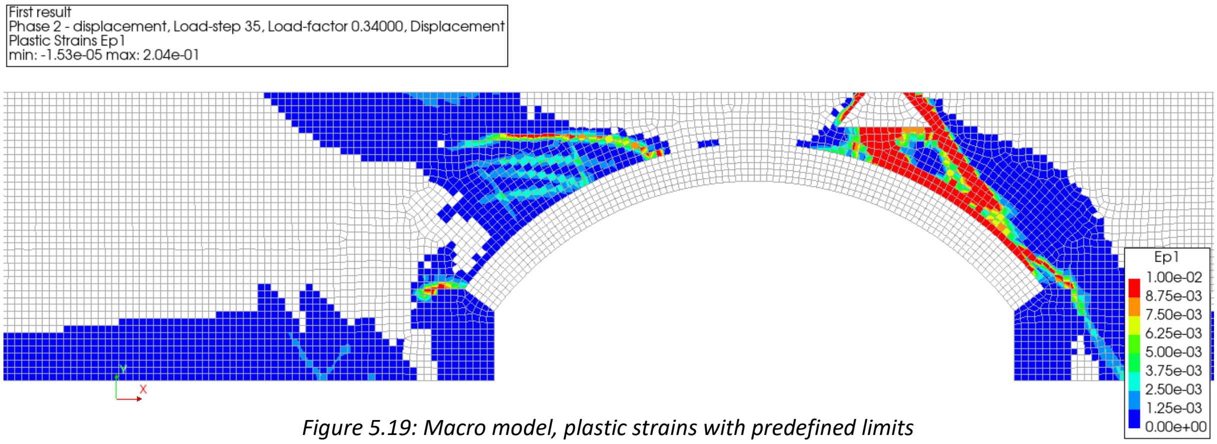

Figure 5.19: Macro model, plastic strains with predefined limits

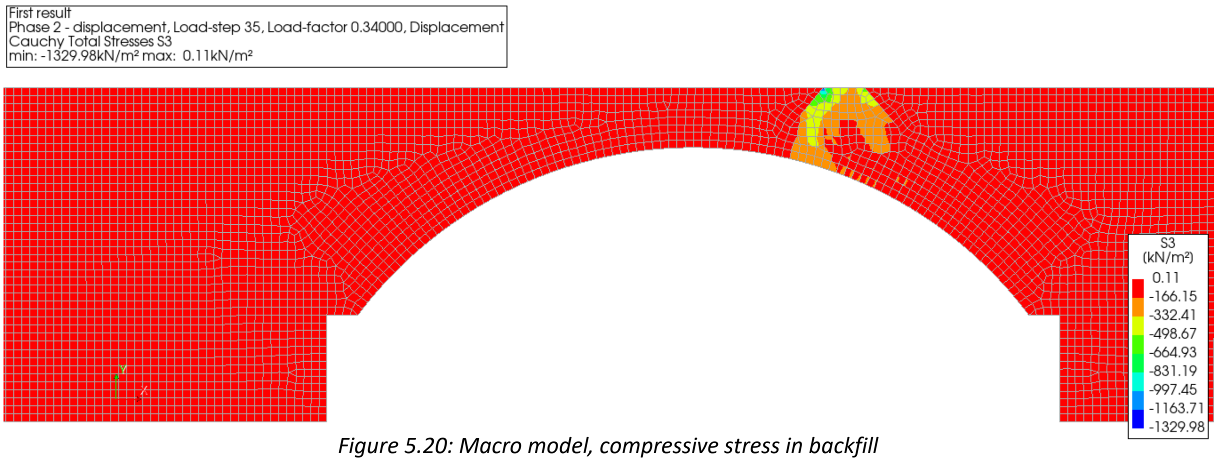

Figure 5.20: Macro model, compressive stress in backfill

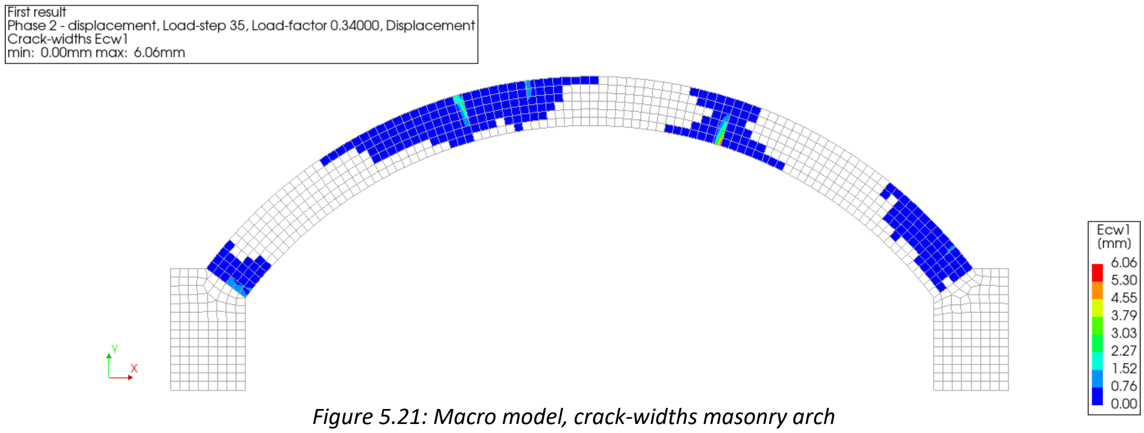

Figure 5.21: Macro model, crack-widths masonry arch

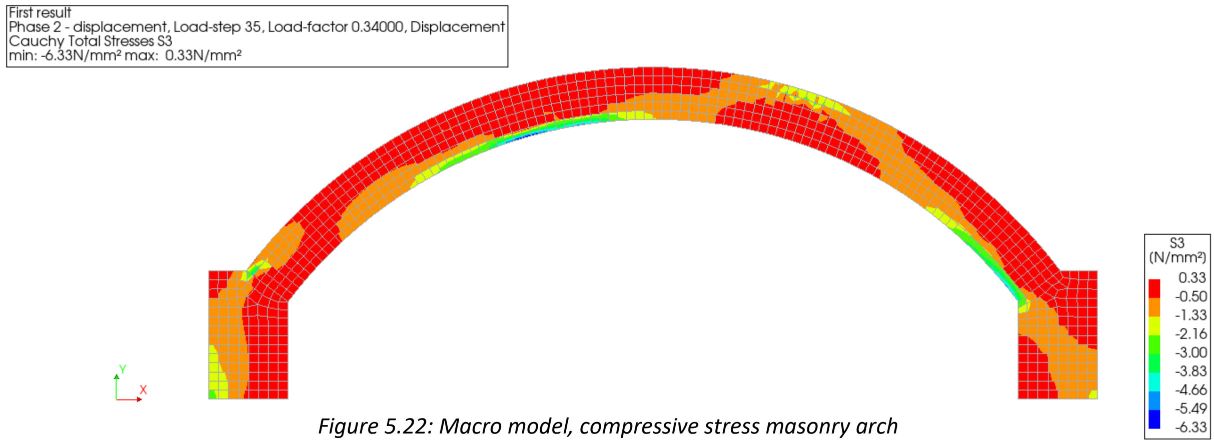

Figure 5.22: Macro model, compressive stress masonry arch

5.4.1.7. Discussion of first results adapted model

The results of the adapted model, presented in the previous section, show that this model is approaching the test results. Although the initial response is different and the peak load is not reached, the overall shape of the force displacement curve is similar to that of the test results.

Comparing the displacements (Figure 5.17) with those obtained in the test (Figure 5.6), it can be noticed that these two figures show similar trajectories. The magnitude of these displacements are for the test unknown, making it not possible to compare the values of the displacements. However, it can be said that the deformation follow a similar path.

In Figure 5.18 the plastic strains are shown, which again show large plastic strains in the backfill, indicating that the backfill is still failing locally. There is, however, a fundamental difference with the failure observed in the initial model of Section 5.4.1.3. In the initial model, large plastic strains appeared directly after the first load step. In the "adapted model", these plastic strains are initially small and grow towards larger values as the load increases, which indicates that there is a sliding failure of the backfill. It is still local failure, but, it is also the governing global failure mode. In Figure 5.19 the plastic strains are again showed with predefined limits for the contour plot settings. This figure shows that the passive side of the backfill also contributes to the stability of the structure. Due to the applied load, the arch is moving to the left and the passive resistance is utilized for stability.

The crack widths, shown in Figure 5.21, show that there are now clear cracks in the masonry arch. As expected, there are four planes where cracks localize and grow larger with increasing load. Although a relatively large crack-width of $6.06\,mm$ was found, a mechanism has not been formed. This is confirmed when considering the compressive stress in the masonry arch, Figure 5.22, and the theory of the "line of thrust", presented in Section 2.2.3. A hinge is formed when the resultant of the compressive forces touches either the intrados or extrados. Figure 5.22 shows that this is not the case, hence there is no mechanism formed.

By performing a parametric study, it could be determined whether the failure of the backfill is indeed governing. When changes in masonry properties do not effect the results and changes in backfill properties do, it can be said that the backfill is governing. Next to the parametric study, it will be investigated whether the more advanced hardening soil material model will give different results as obtained with the "basic" Mohr-Coulomb model.

5.4.1.8. Parametric study

As discussed above, a parametric study is needed to determine what the actual failure mechanism is and if a change in properties also changes the governing failure mechanism. Next to that, tests to determine the mechanical properties of the individual materials are lacking in the supporting report, the parametric study could determine more accurate values for these materials. In Table 5-8 an overview of the influence that various parameters have on the response of the analysis is given. In the following sections, the parameters that do have influence on the response are analysed further. The force displacement curves for the other parameters are shown in Appendix B.

Table 5-8: Influence of various parameters

Parameter		*Influences results*
Masonry		
Tensile strength	f_t	Yes
Tensile fracture energy	G_f^I	No
Compressive strength	f_c	Yes

Compressive fracture energy	G_c	No
Backfill		
Internal friction angle	ϕ	Yes
Dilatancy angle	ψ	No
Lateral pressure ratio	K_0	No
Young's modulus	E	Yes
Soil-Structure interface	R_{int}	No

5.4.1.8.1. Tensile strength

A first study is performed on the tensile strength of the masonry, while keeping all other variables constant. It was observed that the arch is moving and cracks start to form, but, a mechanism had not been formed yet. The test results stated that the formation of a four hinge mechanism is the governing failure mode. In this section it will be investigated whether a lower tensile strength will result in the formation of a four hinge mechanism and what impact a higher tensile strength has on the results. To this end, three different values of the tensile strength are applied, $f_{t,1} = 0.50\ MPa$, $f_{t,2} = 0.05\ MPa$ and $f_{t,3} = 0.01\ MPa$. The resulting force displacement curves are shown in Figure 5.23.

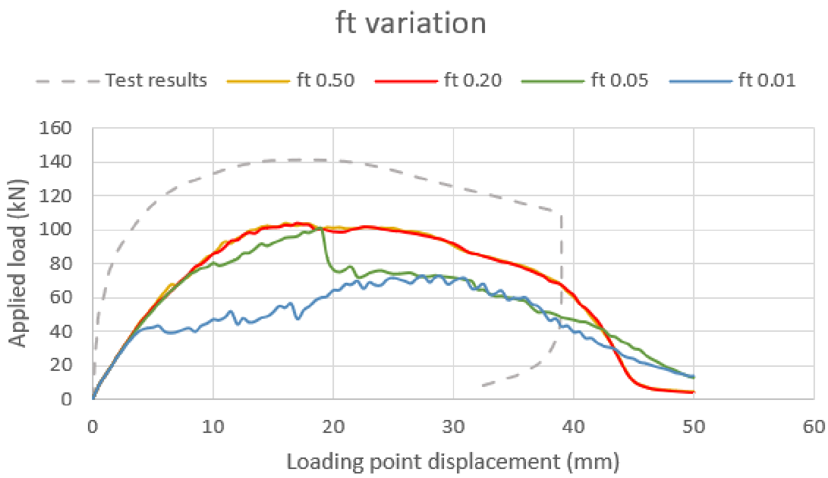

Figure 5.23: Marco model, tensile strength variation

It can be seen that taking a higher value of the tensile strength does not influence the response or peak load, which also supports that indeed the bridge failed due to failure of the backfill. The curves belonging to lower values of the tensile strength show that this value does influence the response of the bridge. For instance the curve belonging to $f_{t,2} = 0.05\ MPa$ shows a sudden drop in the force-displacement curve after reaching the peak load, and the curve belonging to $f_{t,3} = 0.01\ MPa$ shows an different shape from (nearly) the start.

After investigating the results belonging to $f_{t,2} = 0.05\ MPa$, a new phenomenon can be observed. Considering the crack-widths, shown in Figure 5.24, it can be seen that cracks start to form along the arch and not only perpendicular to the intrados/extrados of the arch. This can be explained by considering Poisson's ratio and the compressive forces, Figure 5.26. Poisson's ratio couples the deformations of a material perpendicular to direction of the load. As masonry has a non-zero Poisson's ratio, a compressive force will cause an element to deform and expand in perpendicular direction, creating tensile forces and cracks.

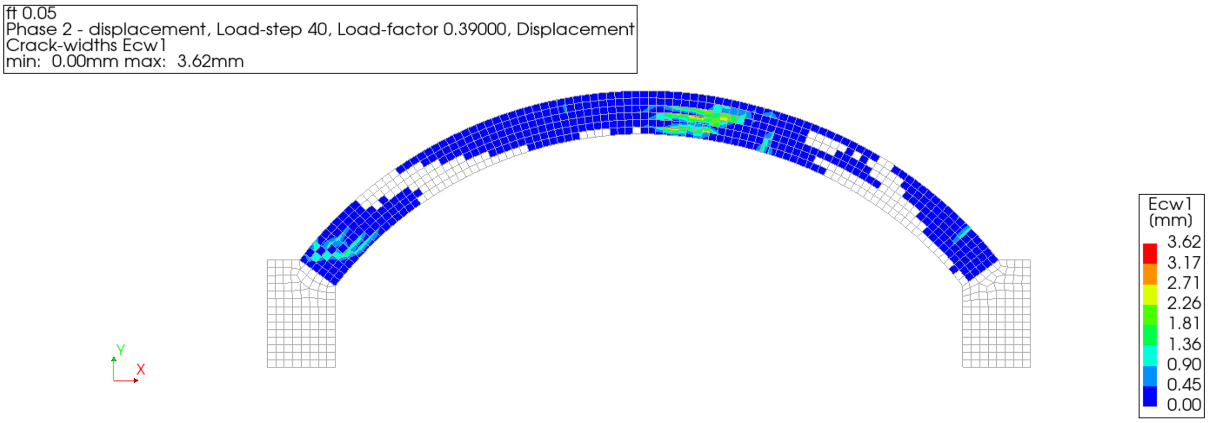

Figure 5.24: Macro model, crack-widths ft 0.05

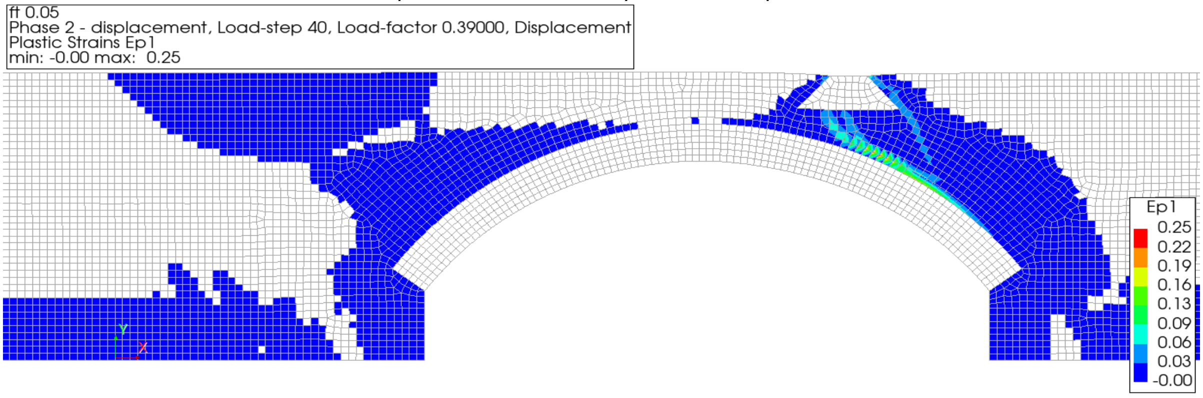

Figure 5.25: Macro model, plastic strain ft 0.05

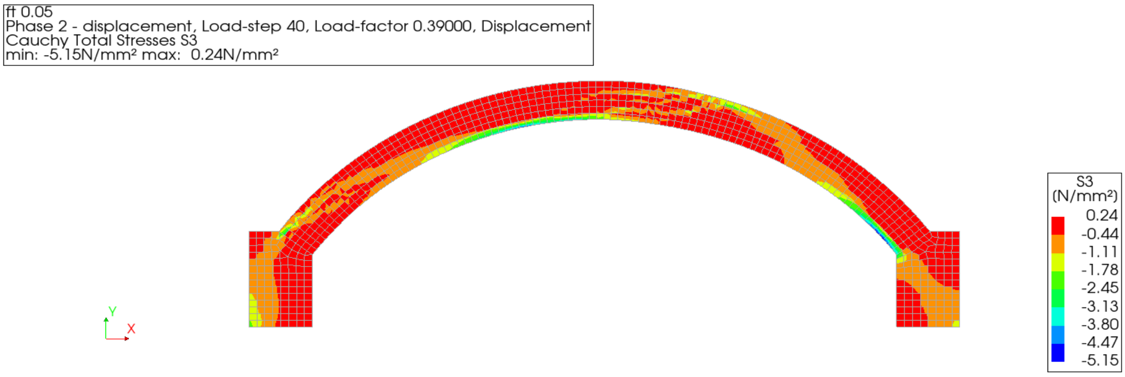

Figure 5.26: Macro model, stress in arch ft 0.05

The parametric study on the tensile strength of masonry showed that taking higher values does not influence the force displacement curve. This supports the observation that the backfill is still the governing part in the model. Taking lower values for the tensile strength, however, does influence the response. Cracks parallel to the intrados/extrados are being formed, which cannot form in reality and was not observed in the test, therefore, this phenomena needs to be avoided in the numerical models. To overcome this problem, values for the tensile strength should not be taken too low. In Section 5.4.3 the reason for this phenomena to occur will be explained in more depth.

5.4.1.8.2. Fracture energy in tension

Similar to the parametric study performed on tensile strength, the tensile fracture energy is also investigated. The resulting force-displacement curves for three different values of the tensile fracture energy, $G_{f,1}^{I} = 0.03\,J/m^2$, $G_{f,2}^{I} = 0.01\,J/m^2$ and $G_{f,3}^{I} = 0.001\,J/m^2$, are shown in **Fout! Verwijzingsbron niet gevonden.**.

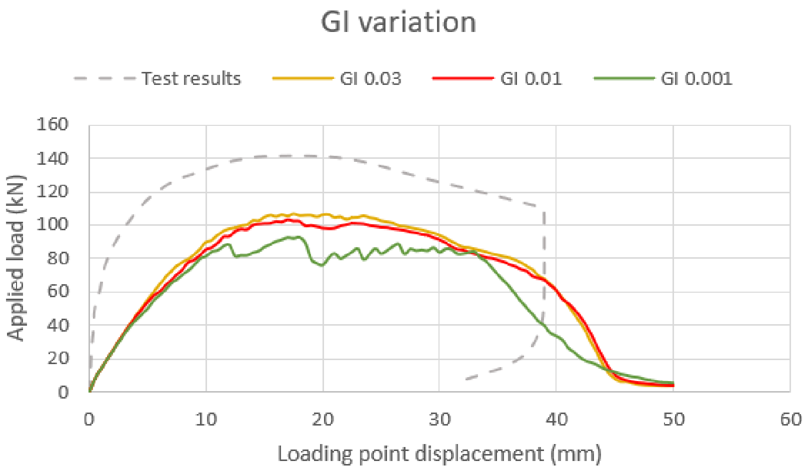

Figure 5.27: Macro model, tensile fracture energy variation

Just as for the tensile strength, an increase in tensile fracture energy does not influence the response. However, a reduction does influence the response. The crack-widths belonging to $G^I_{f,3} = 0.001\ J/m^2$, Figure 5.28, shown that cracks are formed parallel to the intrados/extrados, similar to the results for a lower tensile strength. To overcome this problem, values for the tensile fracture energy should not be taken too low.

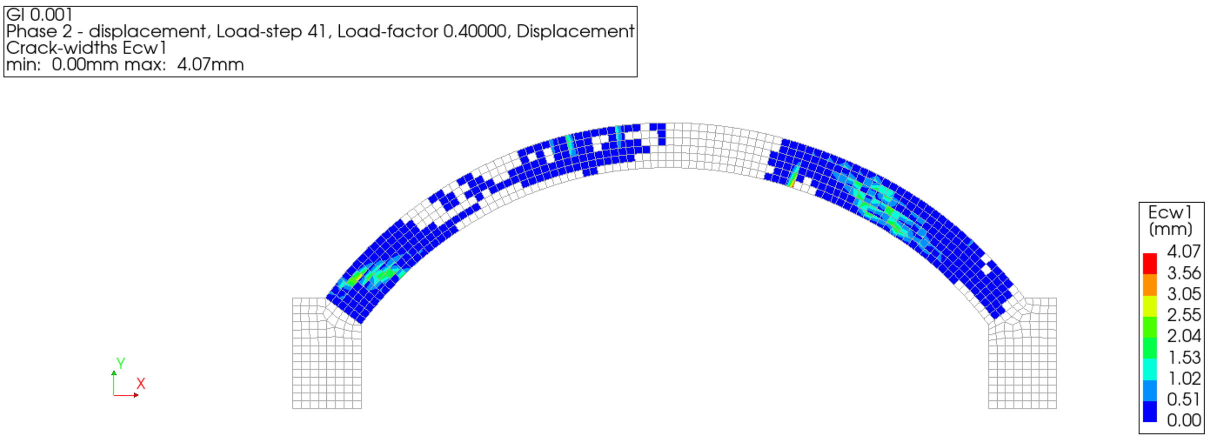

Figure 5.28: Macro model, crack-widths GI 0.0001

5.4.1.8.3. Compressive strength

Next to investigating tensile properties, the compressive properties could also play a role in the response. Recalling the “line of thrust” theory presented in Section 2.2.3, when the resultant of the compressive stress touches the intrados/extrados a hinge is being formed. This compressive stress could be larger then the compressive strength, resulting un crushing of the material. When a “too low” compressive strength is used, crushing could be happening prior to the resultant touching the intrados/extrados and the bridge could loose its stability. Four different compressive strengths are considered, $f_{c,1} = 5\ MPa$, $f_{c,2} = 10\ MPa$, $f_{c,3} = 15\ MPa$ and $f_{c,4} = 2\ MPa$, the resulting force-displacement curves are shown in Figure 5.29.

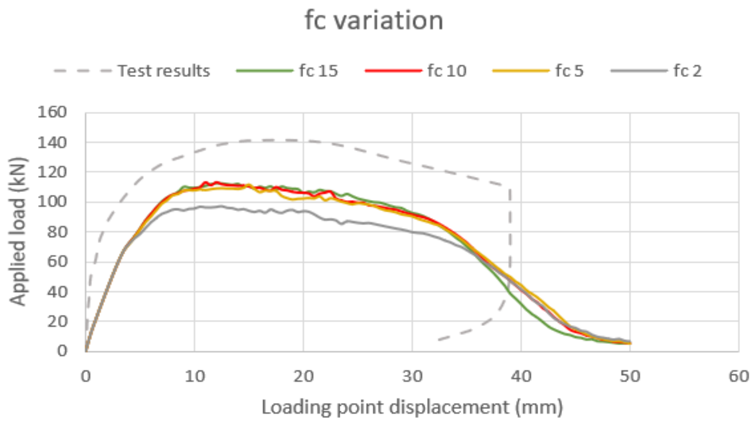

Figure 5.29: Macro model, compressive strength variation

From these curves it can be seen that the compressive strength does influence the peak load of the bridge. However, this difference is only noticed when using a unrealistic low compressive strength of $2\ MPa$ is used. The observed peak load is $97.2\ kN$, which is 14.4% lower compared to the other results. Although crushing of the material does happen, it does not lead to a brittle failure and the global behaviour is still dominated by the behaviour of the backfill. This is made visible when considering the plastic strains and compressive stress, shown in Figure 5.30 and Figure 5.31, respectively. Figure 5.31 shows that the compressive strength is reached at all locations where hinges are expected to be formed.

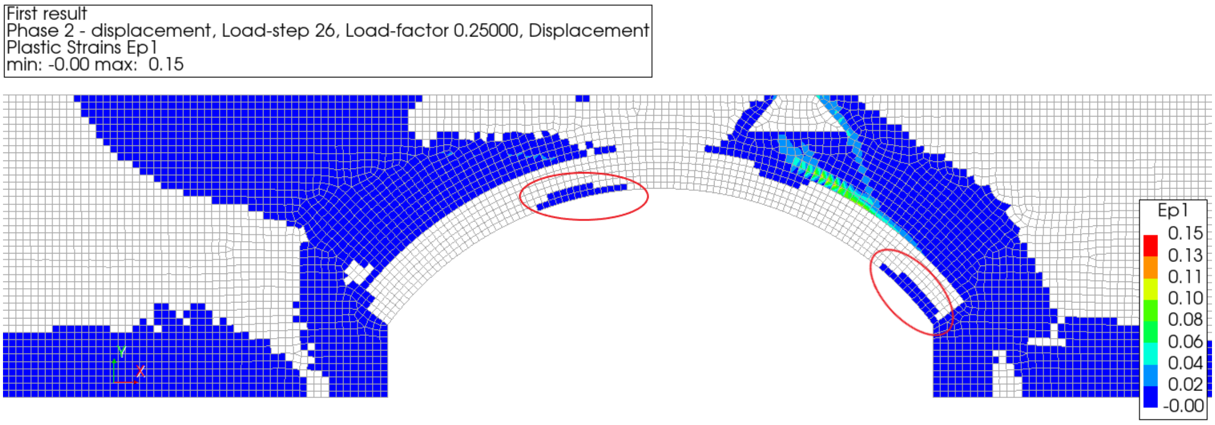

Figure 5.30: Macro model, plastic strains fc 2

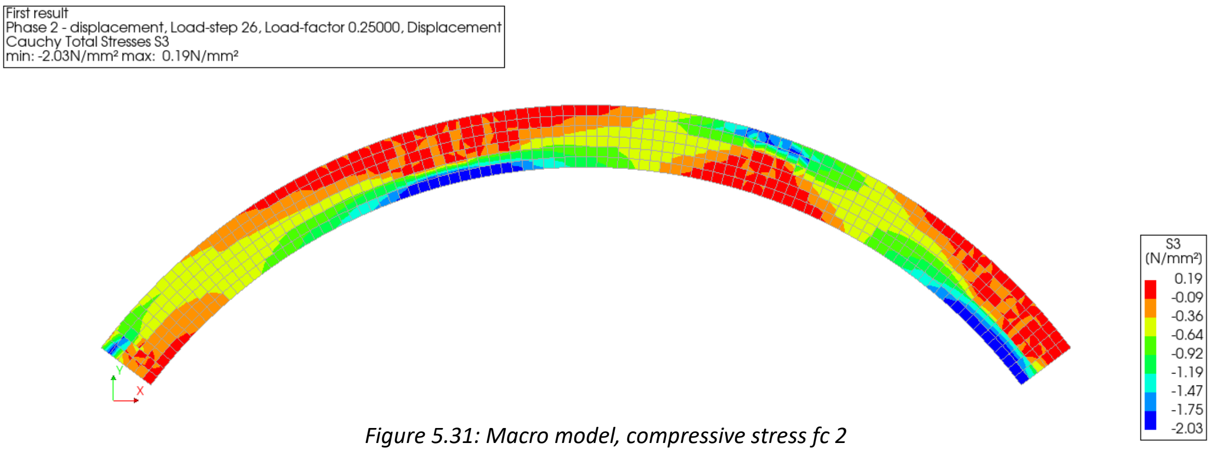

Figure 5.31: Macro model, compressive stress fc 2

5.4.1.8.4. Internal friction angle (backfill)

The previous parametric studies were focused on masonry properties, but, as failure of the backfill is governing, the consequence of changing backfill properties needs to be investigated as well. Next to that, the researchers reported an internal friction angle of $54.5°$, while an angle of $40°$ was used in the model. The reason for using this lower internal friction angle was because of the unlikeliness of a soil having an internal friction angle larger than $45°$, as mentioned in Section 5.2. The impact of this assumed lower internal friction angle is investigated. The force-displacement curves of three different friction angles, $\phi_1 = 30°$, $\phi_2 = 40°$ and $\phi_3 = 54.5°$ are shown in Figure 5.32.

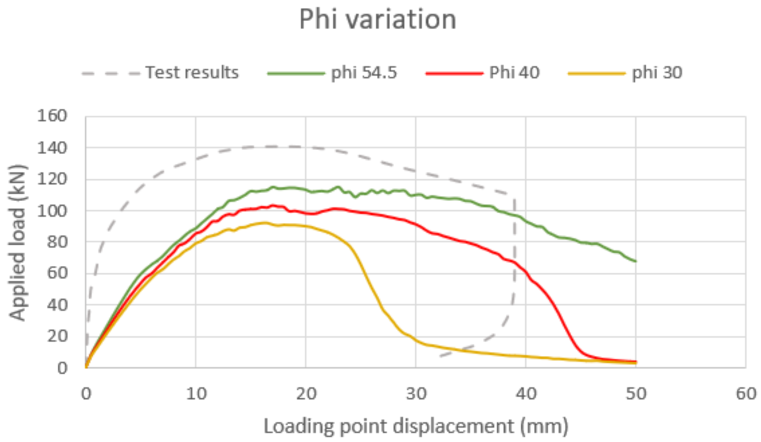

Figure 5.32: Macro model, friction angle variation

The curves in the figure shown that a change in internal friction angle have rather large consequences on the resulting force displacement curve. Taking a lower friction angle will result in a lower peak load and a more brittle post-peak behaviour. A higher internal friction angle, on the other hand, increases the peak load.

5.4.1.8.5. Young's modulus (backfill)

The initial slope of the response is different compared to the test results and previous parametric studies did not cause any change. As the backfill is governing in this test, the Young's modulus of the backfill determines the slope of the initial response. The Young's modulus was not reported in the test papers, but was assumed to be $20.83\ MPa$ in Section 5.4.1.2. As can be seen the slope is not steep enough, hence, a higher Youngs modulus should be taken. The force displacement curves of three different Young's moduli, $E_1 = 20.83\ MPa$, $E_2 = 40\ MPa$ and $E_3 = 80\ MPa$ are shown in Figure 5.33.

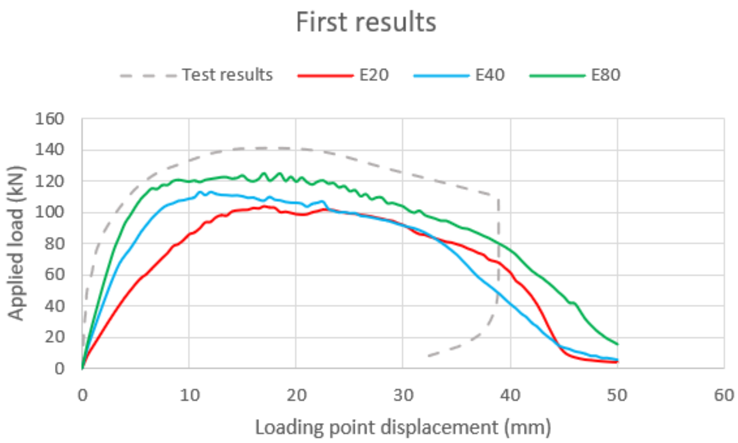

Figure 5.33: Macro model, Young's modulus variation

From these curves, it is clear that increasing the Young's modulus increases the slope of the initial response, as expected, and increases the peak load. The initially assumed Young's modulus of $20.83\ MPa$ is too low, and had to be higher in the test. The curve belonging to $E_3 = 80\ MPa$, shows that it approaches the initial slope obtained in the test. However, for crushed limestone a Young's modulus of $80\ MPa$ is rather high.

5.4.1.9. Calibrated model, properties and results

As mentioned before, the in the paper reported properties were incomplete and assumptions were made about their values. Because of these assumptions, a parametric study was performed. The results of this parametric study make it possible to "improve" the model, in such a way that the actual behaviour could be described more accurately. The properties for this "calibrated" model are shown in Table 5-9. It is noteworthy that the properties that changed were related to the behaviour of the backfill and the internal friction angle, reported by the researchers, is used. Properties describing the behaviour of the masonry arch and soil-structure interface are kept similar to the ones reported in Table 5-6 and Table 5-7.

Table 5-9: Macro model, calibrated backfill properties

Backfill properties Mohr-Coulomb		
linear material properties		
Young's modulus	$\boldsymbol{E}$	$\boldsymbol{40\ MPa}$
Poisson's ratio	v	0
Mass density specification		Saturated density
Density	ρ	$2000\ kg/m^3$
Mohr-Coulomb and Drucker-Prager plasticity		
Plasticity model		Mohr-Coulomb plasticity
Cohesion	c	$7\ kPa$
Friction angle	$\boldsymbol{\phi}$	$\boldsymbol{54.5^0}$
Dilatancy angle	ψ	0^0
Friction hardening		Constant friction angle
Tension cut-off		based on mean stress
Tension cut-off value	p_t	$2\ kPa$
Initial stress		
Lateral pressure ratio		Effective stresses - Isotropic
	K_0	0.7

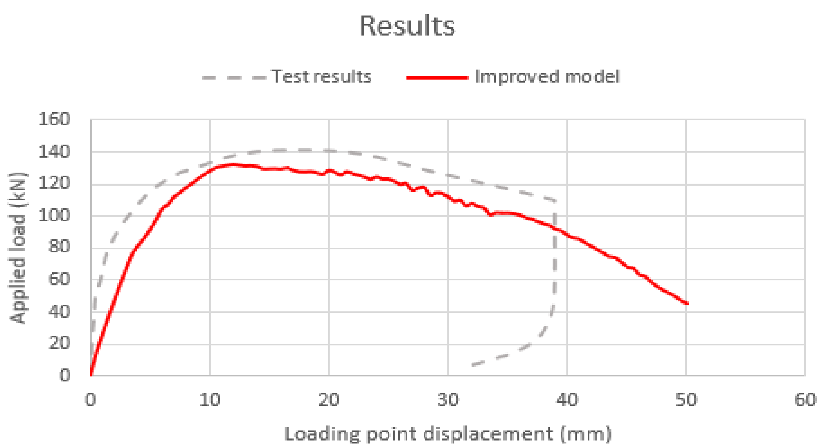

Figure 5.34: Macro model, calibrated

The resulting force-displacement curve is shown in Figure 5.34. Although the peak load of $132.1\ kN$ and initial response are not exactly similar to the test results, the overall shape of the curve is.

5.4.1.10. Hardening soil material model

As mentioned before, the Mohr-Coulomb material model was used to model the backfill. However, the hardening soil material model is more advanced and is expected to model the behaviour of the backfill better. In this section the effect of using the hardening soil model will be investigated. The properties used for the hardening soil model are presented in Table 5-10 , the properties used to model the masonry and soil-structure interface are kept similar to those reported in Table 5-6 and Table 5-7 from Section 5.4.1.2.

Table 5-10: Macro model, hardening soil backfill properties

Backfill properties Hardening Soil		
Modified Mohr-Coulomb engineering input		
Reference triaxial secant stiffness	E	$20.83\ MPa$
Unloading-reloading stiffness	E_{ur}	$62.49\ MPa$
reference oedometer tangent stiffness	E_{oed}	$20.83\ MPa$
Poisson's ratio	v	0
Cohesion	c	$7\ kPa$
Friction angle at shear failure	ϕ	$40°$
Dilatancy angle at shear failure	ψ	$0°$
Use modified Rowe's dilatancy rule		yes
Failure ratio qf/qa		0.9
Exponent m		0.5
Reference pressure		$0.1\ MPa$
Specify preconsolidation stress		Preconsolidation stress based on derived OCR
Tension cut-off		Based on principal stress
Tension cut-off value	p_t	$2\ kPa$
Mass density		
Mass density specification		Dry density and porosity
Density	ρ	$2000\ kg/m^3$
Porosity	n	0.3
Initial stress		
Lateral pressure ratio		Effective stresses - Isotropic
	K_0	0.7

5.4.1.11. First results

The results of this model are given as a force displacement curve, shown in Figure 5.35. A peak load of $109.6\ kN$ is found. Next to the force-displacement curve, the displacements, plastic strains and crack-widths at the peak load are shown in Figure 5.37, Figure 5.36 and Figure 5.38, respectively.

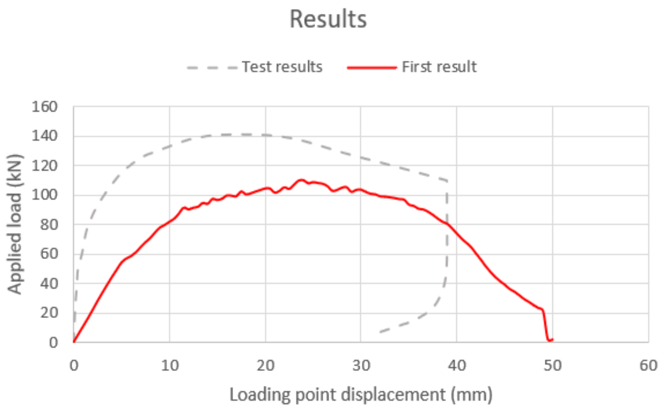

Figure 5.35: Macro model, hardening soil, first results

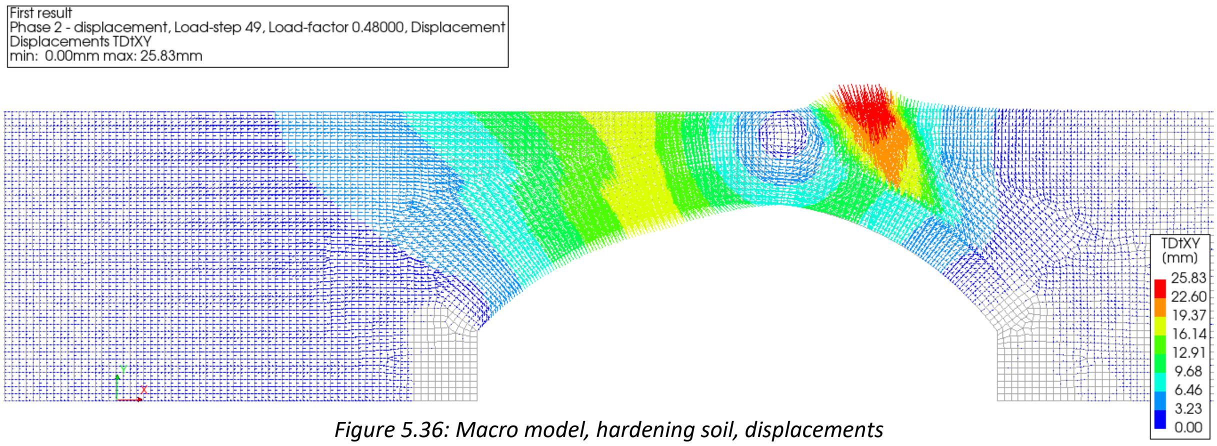

Figure 5.36: Macro model, hardening soil, displacements

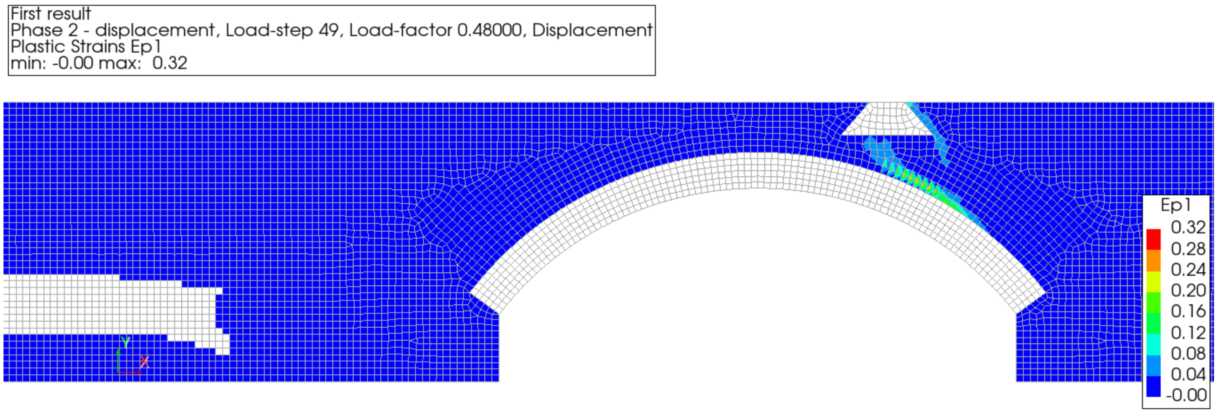

Figure 5.37: Macro model, hardening soil, plastic strains

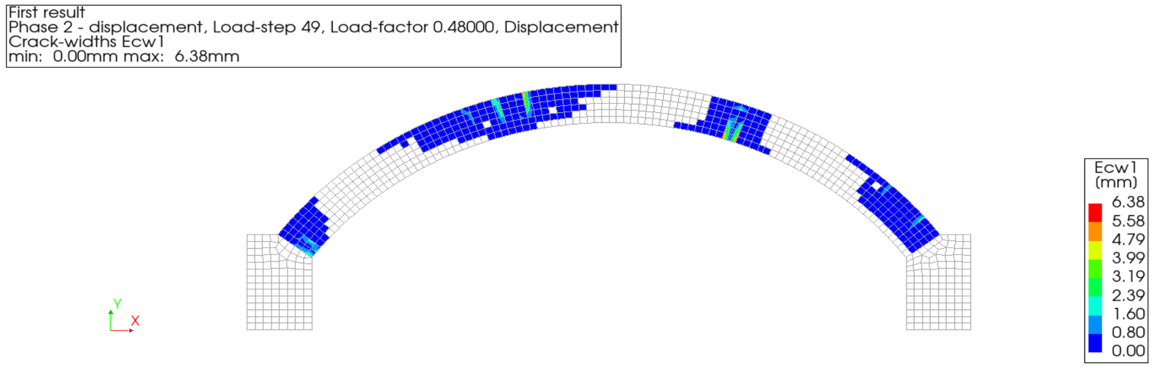

Figure 5.38: Macro model, hardening soil, crack widths masonry arch

5.4.1.12. Parametric study

Similar to the previous model, a parametric study was performed to see what the influence of a change in parameters would have on the results. The resulting force-displacement curves of this study are given in Appendix C. After investigating the results, it was found that the parameters influencing the results were similar to those of the Mohr-Coulomb material model.

There was, however, one variation that showed some unexpected result, namely the variation in internal friction angle of the backfill, shown in Figure 5.39. The results show that increasing the friction angle of the backfill from $40°$ to $54.5°$ would result in a large reduction of the capacity. The results are thus far out of range of the others that they are considered to be inaccurate. It shows that this material model is not able to analyse friction angles greater than $45°$.

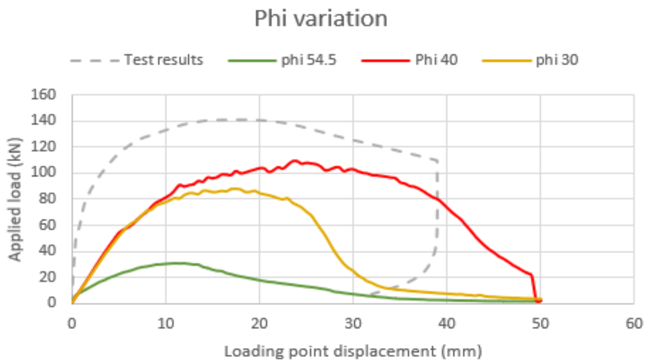

Figure 5.39: Macro model, hardening soil, internal friction angle variation

5.4.1.13. Mohr-Coulomb vs. Hardening soil

It is now possible to compare the results of the different material models used to represent the backfill. To do so, the first results obtained with the methods are shown in Figure 5.40. From this figure it is clear that the resulting force-displacement curves are very close. The biggest difference it that the peak load was found at larger displacement, however, this difference is negligible small. Next to that, the plastic strains (Figure 5.18 and Figure 5.37) show a similar shape and magnitude. In other words, both material models give similar results.

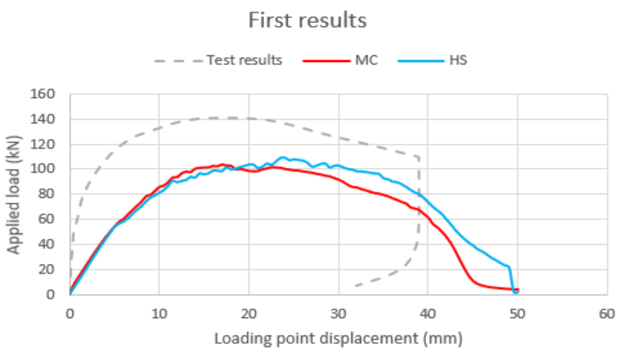

Figure 5.40: Mohr-Coulomb vs Hardening Soil, first results

As for both models a parametric study was performed, these results are also compared in Appendix D. The comparison shows that mostly every variation has similar results, except when the internal friction angle of $54.5°$ is used, shown in Figure 5.41. It would have been expected that an increase in internal friction angle would also increase the peak load and post peak response as was found for the Mohr-Coulomb model. It is believed that the unexpected curve found for the Hardening Soil model has to do with shortcomings of the numerical program and has to be considered as an unrealistic result.

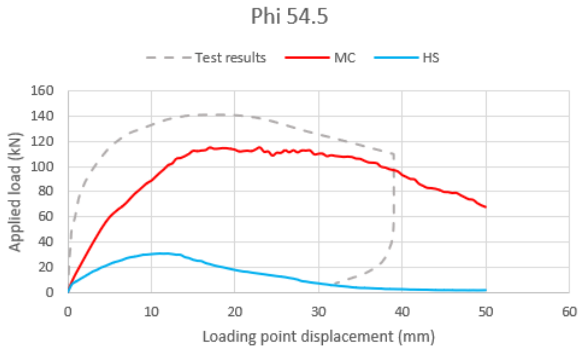

Figure 5.41: Mohr-Coulomb vs Hardening Soil, Phi 54.5

The biggest difference between both material models does not originate from the obtained results, but, has to do with the computational power needed to obtain the results. One analysis performed with the Mohr-Coulomb model took on average 45 minutes while for the Hardening Soil model the average time was a slightly over 2 hours. As the Hardening Soil model is more complex, it could have been expected to take longer to run the analysis. However, the added amount of accuracy is limited, or not even there, making the Mohr-Coulomb model the preferred material model.

5.4.1.14. Introduction of the load

In the test, the load was applied as a point load on a steel profile crossing the test chamber. Due to the differences in backfill cover, there is a small difference of stiffness of the backfill. This mean that the displacements below the steel profile can differ, so that the profile can rotate. In the presented model, the load is introduced as a deformation over a given width, i.e. all nodes have an equal vertical displacement. These two methods to introduce the load in the system are slightly different. In this section the influence of different loading conditions are investigated.

In a first investigation the load was introduced as a redescribed deformation on to of the steel profile, as shown in Figure 5.42. In this model, the area below the profile is not given linear elastic properties, but properties similar to the other backfill. The resulting plastic strains, shown in Figure 5.43, show that adding the rotation capacity to the load introduction, do not overcome the local failure below the profile and show a similar profile to the ones shown in Figure 5.11.

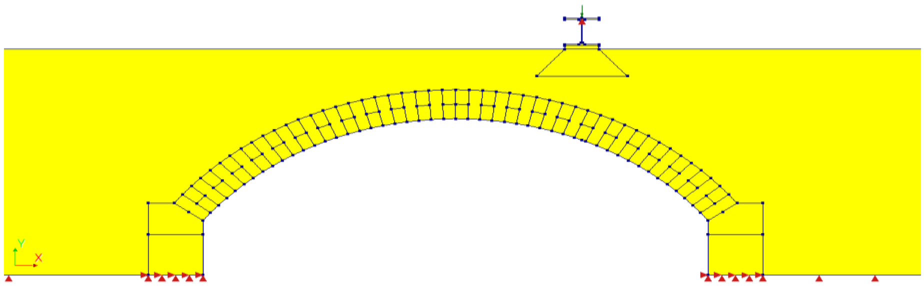

Figure 5.42: Macro model, displacement with profile

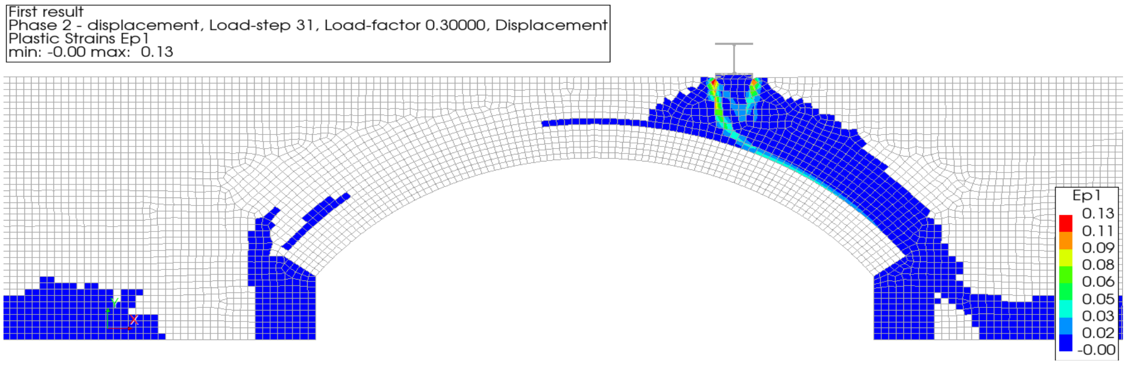

Figure 5.43: Macro model, displacement with profile plastic strains

A second option that is investigated is changing the loading from displacement controlled to force controlled. By doing so, the nodes on the loading edge can have different vertical displacements, i.e. making rotations possible. The results of this analysis are shown in Figure 5.44, again showing the local failure below the load. Changing the loading conditions does not affect the observed local failure of the backfill. Making the added linear elastic part in this area the most effective option to overcome this local failure.

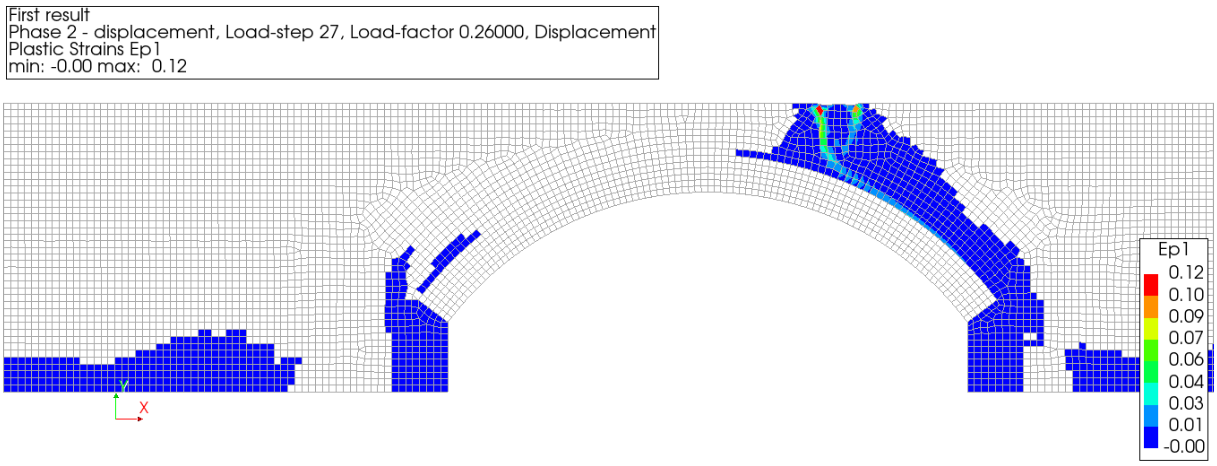

Figure 5.44: Macro model, force controlled, plastic strains

As the load introduces large stresses in the backfill, which lead to the local failure, a final analysis was performed where the load is spread over a larger area, shown in Figure 5.45. The plastic strains shown in Figure 5.46 now also show that the backfill is failing. However, in this case the plastic strains are not large directly below the load, but grow towards the failure that was also observed in the adapted model of Figure 5.18. The findings in these analysis support the fact that the backfill is governing.

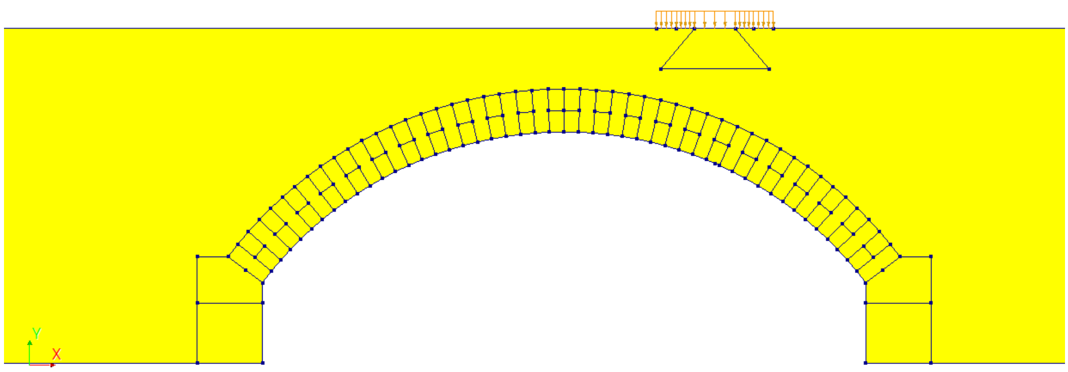

Figure 5.45: Macro model, load spread

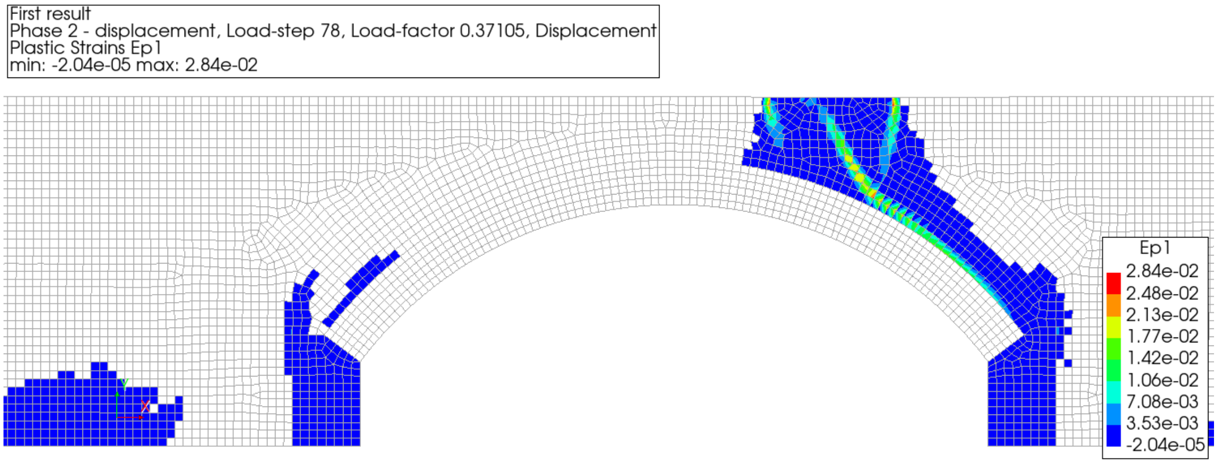

Figure 5.46: Macro model, load spread plastic strains

5.4.2. Micro model

5.4.2.1. Model description

The micro model that will be created follows the approach explained in Section 3.5. In short, a simplified micro model is created where the units are modelled using a basic linear elastic material model and the combined cracking-shearing-crushing material model is used to describe the unit-mortar interfaces. The interaction between the backfill and the arch is modelled using Coulomb-friction interface elements.

From the previous analysis of the macro model, it was found that a small area beneath the load had to be modelled using linear elastic properties to eliminate the local failure of the backfill. Next to that, it was also found that the Mohr-Coulomb material model is the preferred option to model the backfill, as the hardening soil material model did not add accuracy and increased the computational time significantly.

The geometry given in Section 5.4.1.5 is now again used, with the added interface elements between the units. The total model is now shown in Figure 5.47, a detailed overview of the interface elements in the arch is shown in Figure 5.48.

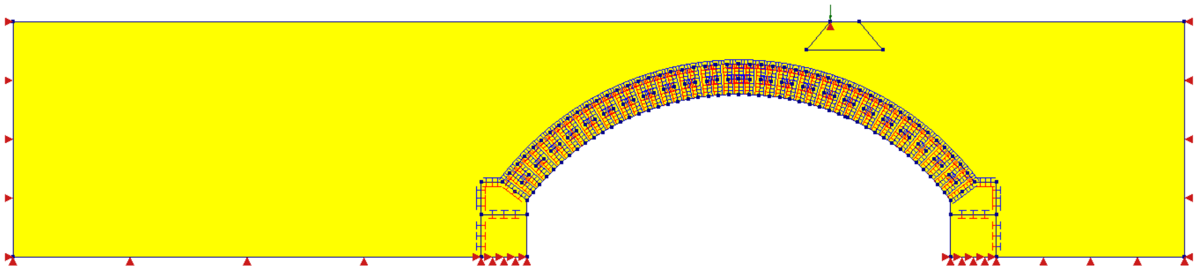

Figure 5.47: Micro model, overview

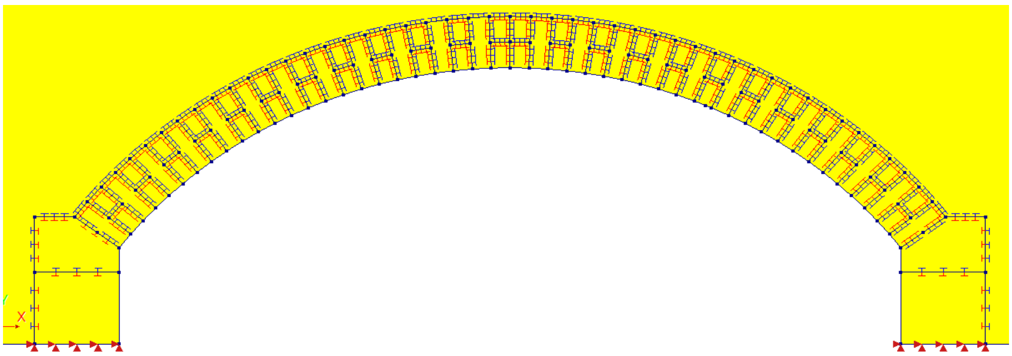

Figure 5.48: Micro model, interface elements detail

5.4.2.2. Model properties

The properties used in the model are given in the tables below. These properties are similar to the ones used in the Macro model. It was found that the reported Young's modulus of the backfill was too low, therefore, the Young's modulus of the "calibrated" model will be used.

Table 5-11: Micro model, Mohr-Coulomb backfill properties

Backfill properties Mohr-Coulomb		
linear material properties		
Young's modulus	E	40 MPa
Poisson's ratio	v	0
Mass density specification		Saturated density
Density	ρ	$2000\ kg/m^3$
Mohr-Coulomb and Drucker-Prager plasticity		
Plasticity model		Mohr-Coulomb plasticity
Cohesion	c	$7\ kPa$
Friction angle	ϕ	40^0
Dilatancy angle	ψ	0^0
Friction hardening		Constant friction angle
Tension cut-off		based on mean stress
Tension cut-off value	p_t	$2\ kPa$
Initial stress		
Lateral pressure ratio		Effective stresses - Isotropic
	K_0	0.7

Table 5-12: Micro model, Coulomb friction soil-structure interface properties

Interface properties Coulomb friction		
linear material properties		
type		2D line interface
Normal stiffness modulus-y	k_n	$1000\ N/mm^3$
Shear stiffness modulus-x	k_s	$10\ N/mm^3$
Coulomb friction		
Cohesion	c	$5.6\ kPa$
Friction angle	ϕ	$34°$
Dilatancy angle	ψ	$0°$
Interface opening model		Tension cut-off
Tensile cut-off value	p_t	$2\ kPa$

Table 5-13: Micro model, unit properties

Masonry	Linear material properties
Young's modulus, E	$2040\ MPa$
Poisson's ratio, v	0.2
Mass density, ρ	$2300\ kg/m^3$

Table 5-14: Micro model, cracking-shearing-crushing interface properties

Interface properties combined cracking-shearing-crushing		
linear material properties		
type		2D line interface
Normal stiffness modulus-y	k_n	$1663\ N/mm^3$
Shear stiffness modulus-x	k_s	$693\ N/mm^3$
Combined cracking-shearing-crushing		
Cracking		
tensile strength	f_t	$0.2\ MPa$
Fracture energy	G_f^I	$0.01\ J/m^2$
Shearing		
Cohesion	c	$0.3\ MPa$
Friction angle	ϕ	$30°$
Dilatancy angle	ψ	$0°$
Shear fracture energy	G_f^{II}	$0.2\ J/m^2$
Crushing		
Compressive strength	f_c	$10\ MPa$
Factor Cs		9
Compressive fracture energy	G_{fc}	$15\ J/m^2$
Equivalent plastic relative displacement	κ_p	$8\ mm$

5.4.2.3. First results

The results of the analysis are given in the Figures below. In Figure 5.49 the force-displacement curve is shown, where a peak load of 121.5 kN was found at a loading point displacement of 16.5 mm. The plastic strains in the backfill, the relative interface displacements and the total interface tractions are shown in Figure 5.50, Figure 5.51 and Figure 5.52, respectively.

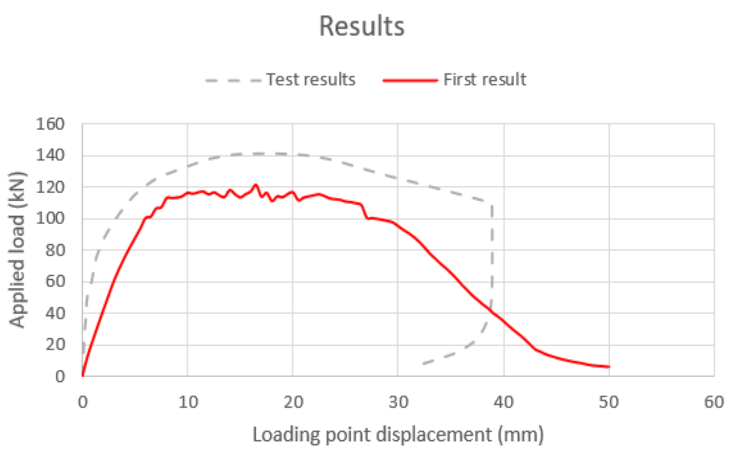

Figure 5.49: Micro model, force-displacement curve

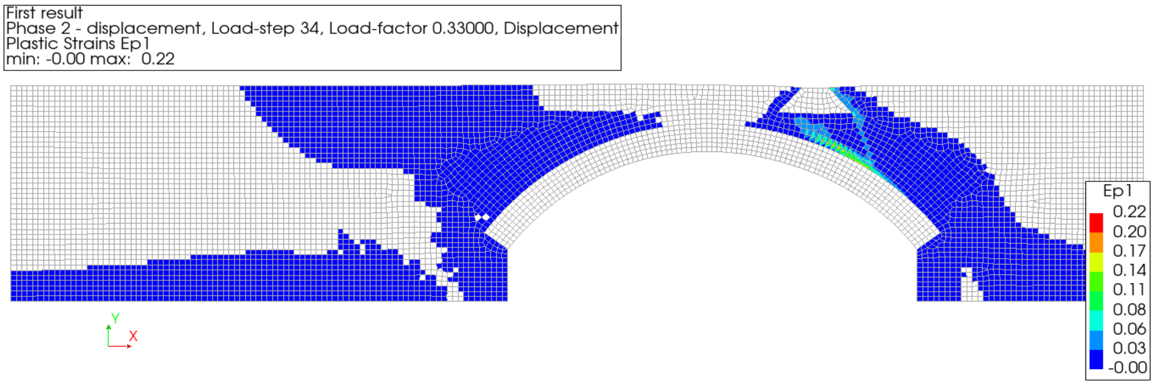

Figure 5.50: Micro model, plastic strains

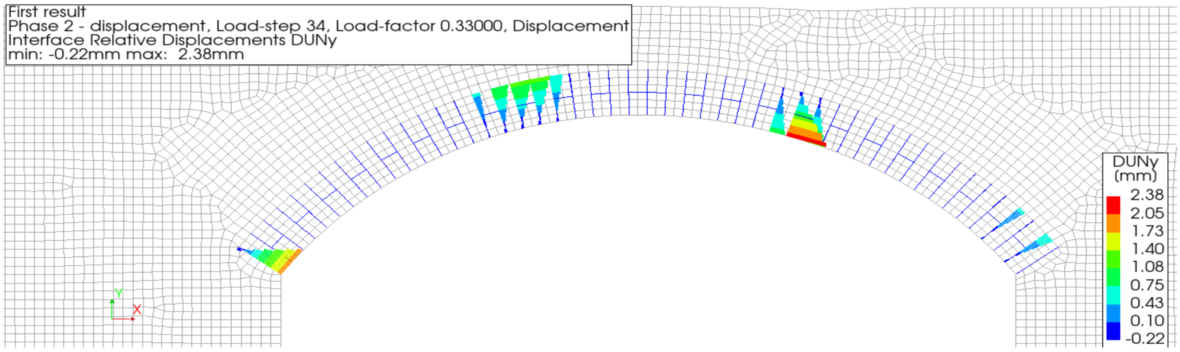

Figure 5.51: Micro model, relative interface displacements

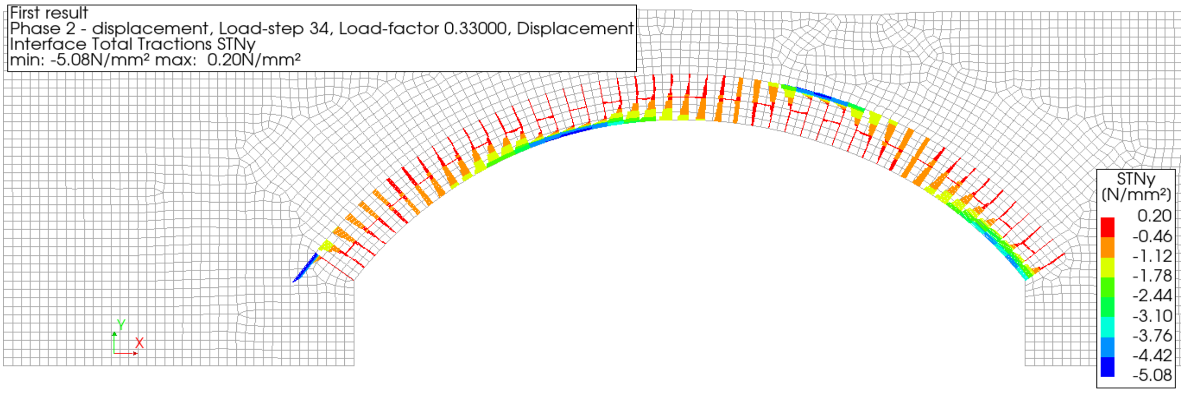

Figure 5.52: Micro model, total interface tractions

5.4.2.4. Discussion of results

The force-displacement curve from Figure 5.49, shows that the model is close to the test results. Although the initial response is slightly different and the peak load is not reached, the overall shape of the curve looks similar to the test results.

Considering the plastic strains, shown in Figure 5.50, large plastic strains in the backfill are found. These strains are similar to the ones found in the macro model, which makes sense as the same material model for the backfill was used. The magnitude of these strains grows in every step and localizes when the strains become larger, again indicating sliding failure of the backfill.

The relative interface displacements, shown in Figure 5.51, are actually representing the crack widths in the masonry arch. The figure shows that the cracks are localizing in the planes where it is expected the hinges to develop, in order to create the four hinge mechanism. Although it is clear that the cracks are forming, the displacements are small and four hinges did not fully develop yet. Which gives power to the finding that the sliding failure of the backfill was the actual governing failure mode.

When analysing the total interface tractions, Figure 5.52, it can be seen the compressive strength of the interfaces is not reached, indicating that crushing does not occur. However, the relative interface displacements show negative values. This is due to the used non-linear interface model, where pre-peak inelastic deformations can occur before reaching the compressive strength. What can be seen is that the resultant of the compressive stress is gradually moving to the intrados or extrados of the arch. The "line of thrust" theory, presented in Section 2.2.3, explained that when this resultant reaches one of the edges a hinge will be formed. Looking at Figure 5.52, it is clear that this is not happening in four planes, i.e. a mechanism has not been formed yet and the backfill is governing.

5.4.2.5. Parametric study

Just as was performed with the macro model, and because of the uncertainty of the actual material properties, the effect of a change in certain material properties is investigated. This study will help determine what parameters are actually influencing the behaviour of the model. Next to that, the result can be compared to those of the macro model, which could indicate what modelling technique is preferable when modelling masonry arch bridges.

In Table 5-15 and overview of the performed variations and whether they influence the results or not is given. In the following sections the parameters that do influence the results will be investigated into depth. The force-displacement curves of the other variations are shown in Appendix E.

Table 5-15: Micro model, influence of various parameters

Parameter		*Influences results*
Masonry		
Tensile strength	f_t	No
Tensile fracture energy	G_f^I	No
Compressive strength	f_c	Yes
Compressive fracture energy	G_c	No
Backfill		
Internal friction angle	ϕ	Yes
Dilatancy angle	ψ	No
Lateral pressure ratio	K_0	No
Soil-Structure interface	R_{int}	No

5.4.2.5.1. Compressive strength

To investigate the influence of the compressive strength, three different strengths are considered, $f_{c,1} = 5\ MPa$, $f_{c,2} = 10\ MPa$ and $f_{c,3} = 15\ MPa$. The resulting force-displacement curves are shown in Figure 5.53.

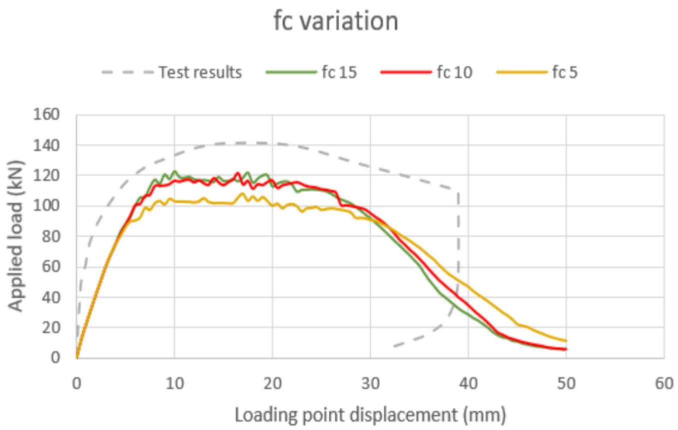

Figure 5.53: Micro model, compressive strength variation

The curves show that reducing the compressive strength to $5\ MPa$, also reduces the peak load to $107.9\ kN$, which indicates that crushing will now happen in the masonry arch. Which is confirmed by the relative interface displacements shown in Figure 5.54. It can be seen that there are negative displacements where the material is crushing.

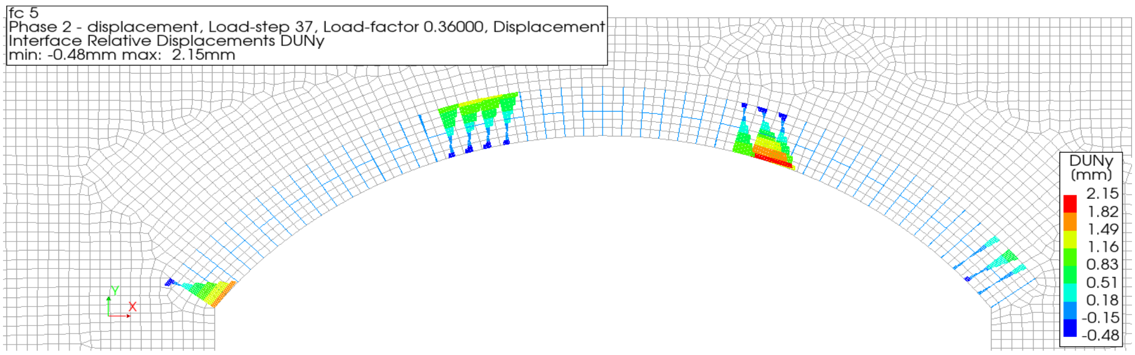

Figure 5.54: Micro model, interface relative displacements

Although the material is crushing and the peak load is reduced, the post-peak behaviour did not change. Next to that, Figure 5.54 shows that the four hinge mechanism is still not found. This means that the peak load is limited due to the reduced compressive strength, but the post-peak response is determined by the behaviour of the backfill.

5.4.2.5.2. Internal friction angle (backfill)

As was explained in Section 5.4.1.8.4, different values for the friction angles are reported in the documents. Similar to those values, the variations for the internal friction angles are performed again using $\phi_1 = 30°$, $\phi_2 = 40°$ and $\phi_3 = 54.5°$. The resulting force displacement curves are shown in Figure 5.55.

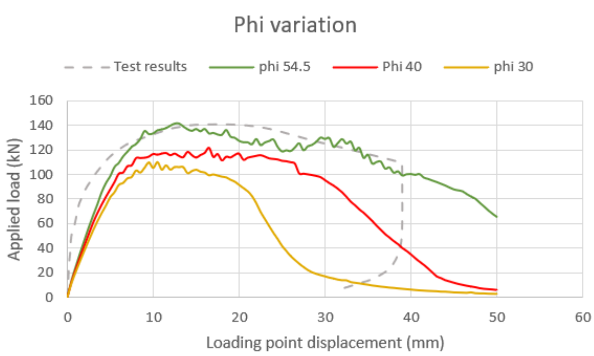

Figure 5.55: Micro model, friction angle variation

The curves in the figure shown, again, that the internal friction angle plays a mayor part in the behaviour of the bridge. A lower friction angle will result in a lower peak load and a more brittle post-peak behaviour. Where a higher internal friction angle, on the other hand, increases the peak load.

5.4.2.6. Calibrated model

Again, due to the incompleteness of reported material properties and the assumptions made for these properties, it is now possible calibrate the model to be closer to the test results. As the parametric study showed that only the internal friction angle of the backfill had a big influence on the behaviour, by increasing this friction angle from $40°$ to $54.5°$ a better fit is found. All other properties are kept similar to those of Section 5.4.2.2, the resulting force-displacement curve is shown in Figure 5.56.

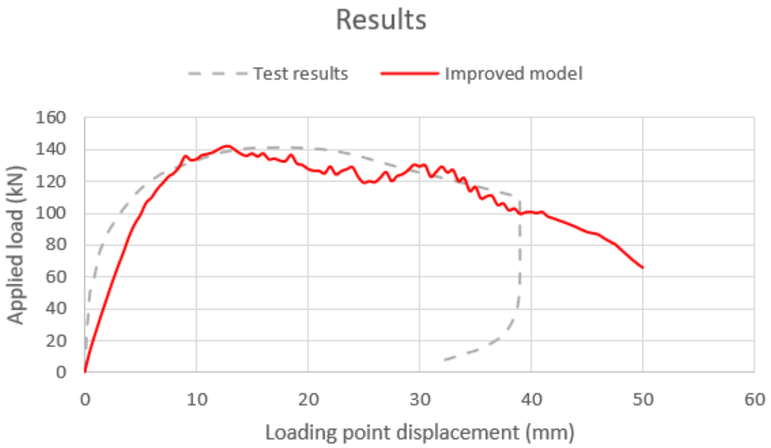

Figure 5.56: Micro model, calibrated

The calibrated model has a peak load of $141.5\ kN$, where in the test a peak load of $141\ kN$ was found. Looking at the figure, the initial response of the model is slightly different compared to the test results, however, the overall shape of the curves are very similar.

5.4.3. Micro vs. Macro

In this section, the results of the micro and macro models are compared, starting with the initial results shown in Figure 5.57. As can be seen, the curves are close to each other and the models seem to behave similar. For both models sliding failure in the backfill was the governing failure mode, as explained in Sections 5.4.1.6 and 5.4.2.4. Not only the force displacement curves are close to each other, so are the crack widths, Figure 5.21 and Figure 5.51. In the macro model a crack width of $2.64\ mm$ was found, in the micro model this was $2.38\ mm$. When the initial assumed properties are used, both models behave similar and show similar results.

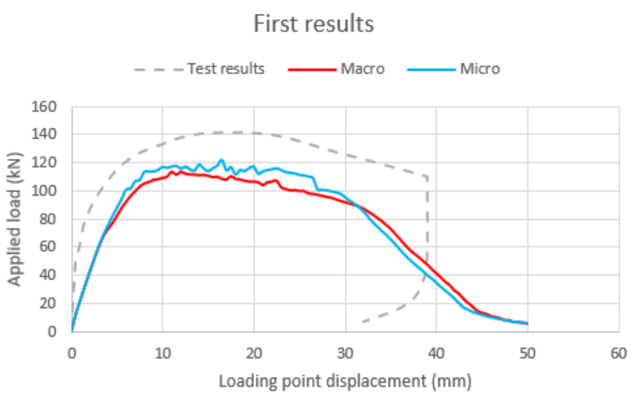

Figure 5.57: Micro vs. Macro, First results

Comparing the results from the parametric studies, it is found that the models are sensitive to changing properties. Both models are sensitive to a change in internal friction angle of the backfill, which could also be expected considering the dominant failure of the backfill. Both models are also sensitive to changes in compressive strength, however, the micro model is more sensitive compared to the macro model. In the macro model, reducing the compressive strength to $2\ MPa$ lead to a reduction of the peak load of 14.4%. While in the micro model, reducing the compressive strength to $5\ MPa$, lead to a reduction of 11.2%.

Considering the tensile properties, it is important to consider the way the material models are defined and what the difference between the modelling techniques are. Masonry is defined as a composite material of bricks and mortar, where the tensile properties are governed by the weakest part in this composite. For masonry, the weakest part is the brick-mortar bond strength and it is expected that the arch will fail in these interfaces. In a micro modelling approach, the engineer implements this assumption into the model geometry by placing interface elements between the units, in such a way that this is the only place where it can fail, i.e. predefined crack patterns. In a macro modelling approach, failure can occur anywhere in the arch and in any direction. Although this is the case, the initial results showed that, for both micro and macro model, the cracks are forming perpendicular to the intrados or extrados, as was expected. This changes for the macro model when a lower value for the tensile strength is used, where the cracks became parallel to the intrados. There are two reasons that together cause this to occur, Poisson's ratio and isotopy. As explained in Section 5.4.1.8.1, Poisson's ratio relates a deformation in one direction to a deformation in the perpendicular direction. In other words, compressing a material in a given direction can cause tensile strains perpendicular to the loaded direction, as shown in Figure 5.58. Next to the Poisson's ratio, isotropy means that the properties of a material are similar in all directions. In the macro model, an isotropic material model was used to describe the masonry, where the tensile strength came from the brick-mortar bond strength, $f_{t,interface}$ in Figure 5.59. In reality, this bond strength is only perpendicular to the arch, but, due to isotropy this strength is now also given in the other direction, $f_{t,brick}$ in Figure 5.59, while In reality $f_{t,interface} \ll f_{t,brick}$ instead of the used $f_{t,interface} = f_{t,brick}$ relation. The combination of high compressive forces, Poisson's ratio, isotropy and low tensile strength is the cause for the unexpected cracks and force-displacement curve shown in Figure 5.60. The phenomena can be avoided by not using too low values for the tensile strength in the macro model.

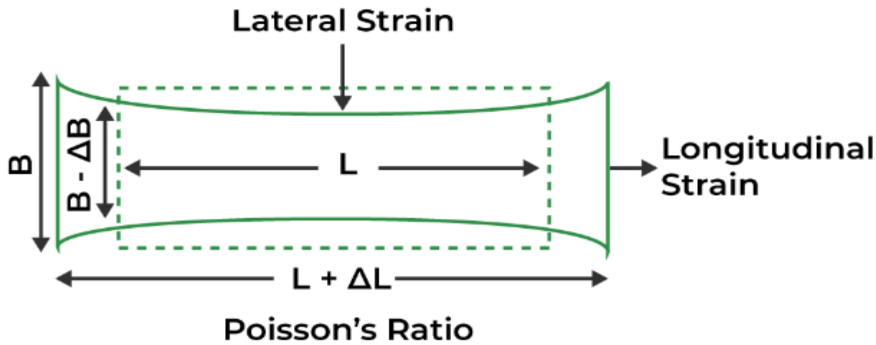

Figure 5.58: Poisson's ratio

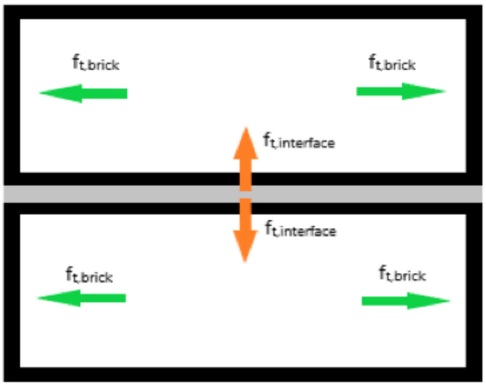

Figure 5.59: Tensile strength masonry

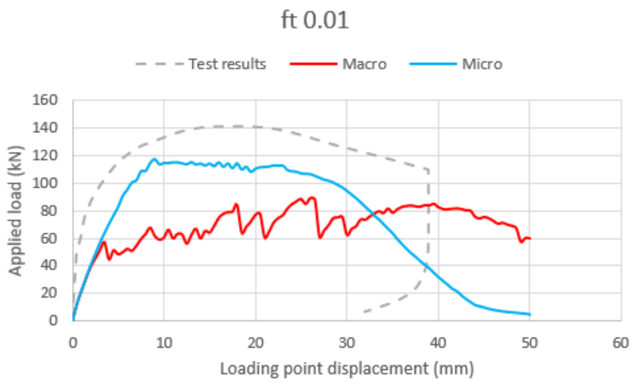

Figure 5.60: Micro vs Marco, ft 0.01

It was found that both models are calibrated to the test results, by increasing the internal friction angle of the backfill, shown in Figure 5.61. Both models are now close to the results obtained in the test and their post peak behaviour is very similar. The micro model shows a slightly higher peak load of $141.6\ kN$, where in the macro model a peak load of $132.1\ kN$ is found. The peak load of the micro model is almost exact the peak load found in the test.

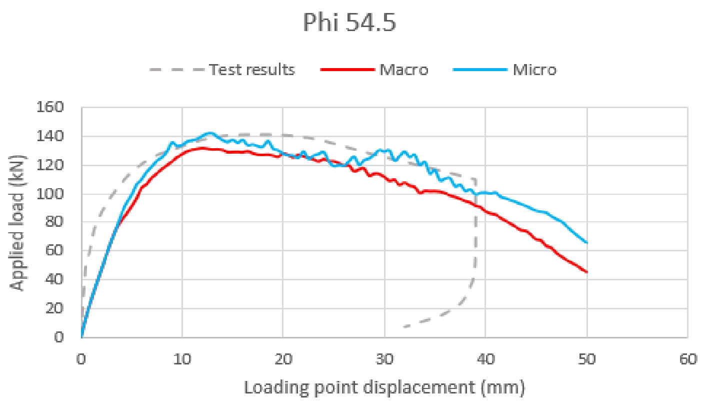

Figure 5.61: Micro vs Marco, Phi 54.5

Other variation in the material properties did not show changes and therefore, the results of both micro and macro model are close. All other variations are shown in Appendix F.

6. Conclusions and recommendations

6.1. Conclusions

The work presented in this study investigated different modelling approaches that can be followed when modelling masonry arch bridges. The main goal was to find a numerical model that is able to capture the actual behaviour of the masonry arch bridges. Masonry arch bridges are a combination of a masonry arch and the soil surrounding the arch, i.e. the backfill. As the behaviour of soils has been investigated into depth, this study focussed, initially, more on different modelling approaches that represent the behaviour of masonry. To do so, first the behaviour of an isolated masonry arch (i.e. without any backfill) is investigated, after which backfill is added. A main research question was defined, followed by five sub-questions. The main research question this study is addressing is:

What is the role of constitutive models on simulating the structural behaviour of masonry arch bridges?

In order to formulate an answer to this question, answers to the sub-questions are needed.

Sub-questions:

SQ1. Could the models describe the behaviour of just the masonry arch?

In the modelling approach presented in this study, three types of models were considered: a micro model, in which the components of the masonry arch are modelled separately; an isotropic macro model (i.e. total strain crack); and an anisotropic macro model (i.e. engineering masonry). Initially the models were employed to simulate the tests conducted at the University of Minho. This showed that the behaviour of an isolated masonry arch can be modelled with high precision. The precision of the model depends, however, on the approach used to represent the arch. As masonry is an anisotropic material, it is essential to assign a material model that is capable to take this behaviour into account. Comparing the macro models, total strain crack and engineering masonry, shows that the isotropic model fails to capture the brittle failure in the post peak behaviour, where the anisotropic model is.

There is also a big discrepancy between the models and the tests. This difference is found when considering the hinge formation sequence. In the tests, a four hinge mechanism was formed before the peak load was attained, where in the models only two hinges were formed before and two hinges after the peak load. However, when examining the force displacement curve of the test results, some sort of strengthening occurs after the peak load is reached, meaning that full collapsed did not occur yet. This is also visible in the results of all models and raises questions whether the reported behaviour is correct. It is plausible that the cracks appeared at the given forces, but that doesn't mean these are fully developed hinges yet.

Overall the engineering masonry and micro model are very well suited to represent the behaviour of a masonry arch. Both models are sensitive to changes in tensile properties, however, the result of such a change is different for both models. Changing either the tensile strength or tensile fracture energy, leads to a change in both peak load and post peak behaviour in the macro models. Where, in the micro model, a change in tensile strength only affects the peak load and a change in tensile fracture energy changes only the post peak behaviour. This is due to the fact that the macro models are based on a total strain theory, where stress is related to strain, and the micro model (i.e. interface material model) is based on a total deformation theory, where tractions are related to displacements.

SQ2. Does the accuracy change when backfill is added to the model?

To assess the accuracy of the models, a second test (performed at the University of Salford) was considered, where backfill was added to the masonry arch bridge. The accuracy of the numerical results did change when backfill was added to the problem. It was determined that the backfill behaviour is governing the behaviour of the investigated bridge. A change in masonry properties did not result in large differences, but a change in the internal friction angle of the backfill did cause large differences.

Due to the plane strain conditions it was not possible to employ the engineering masonry material model. Therefore, the total strain crack model and micro model were used. There is a minimal variation between the results of these models, which was the case for just the arch. But again, the behaviour of the backfill dominated the behaviour of the bridge, making it hard to determine which one is more suitable.

SQ3. What is the impact of isotropy on the model accuracy?

Isotropy plays a major role when analysing masonry arches or masonry arch bridges. As already mentioned in *SQ1*, the anisotropic models are capable of reproducing the brille failure for just a masonry arch, where the isotropic model is not. When backfill is added, the difference between an isotropic and anisotropic model diminished significantly, as in this case the backfill failed.

Although the difference may appear negligible, the parametric study showed that it does influence the results when a low tensile strength is assigned to the material. In an isotropic material model, the tensile strength is assigned to all directions of the element, where an anisotropic material has a different strength in different directions. In masonry arch bridges, relatively high compressive stresses are found in the arch to transfer the load to the subsoil. When a material is loaded in one direction, Poisson's effect causes the element to deform in the perpendicular direction. Given the constraints provided by the surrounding elements, stresses arise. As the arch is loaded in compression, Poisson's effect now causes tensile stresses to occur in the transversal direction. In this direction, the tensile strength of the masonry should be taken as the tensile strength of the bricks rather than the brick-mortar bond strength, used in the isotropic model. For low values of the tensile strength, an unrealistic failure pattern in the arch is found with the isotropic model, where the micro model does not show this failure pattern.

Overall, isotropy can influence the accuracy of numerical models. In general, larger values for tensile strength and fracture energy need to be used in isotropic models to avoid unrealistic failure patterns. However, when the behaviour of the backfill dominates the behaviour of the bridge, isotropy becomes less important to represent the behaviour of the masonry arch.

SQ4. How much accuracy is added when a micro modelling technique is used?

As the results obtained in this study derive from research performed by others, it is hard to quantify the enhanced level of accuracy. To make a statement about the accuracy of the models in terms of resemblance of the failure mechanism, more data is needed on for instance crack widths and displacements. For the Minho test, the micro model was close to the first test results and the macro model closer to the second test results. In the Salford test, the results of both approaches were close to each other. It is therefore not possible to state whether the results of the one or other approach are more accurate.

What is evident, however, is that in general smaller values for tensile properties can be used in the micro model compared to the macro models. As explained above, this comes from Poisson's effect and isotropy. Next to that, micro models are better in localizing cracks and hinges compared to the macro models.

SQ5. Which modelling approach has to be used for masonry arch bridges?

The primary, and preferred, approach is a micro modelling approach. The results obtained in this study, show the best resemblance with the results obtained in either the Minho or Salford test. Next to that, the model is less sensitive to a change in material properties and is able to take the anisotropic nature of masonry into account.

The second approach is the macro model approach. When considering just a masonry arch, the engineering masonry material model is able to mimic the behaviour of the masonry, and the results are comparable with those obtained with the micro model. However, this material model can only be used in plane stress conditions and couldn't be used for the Salford test where plane strain conditions were applied. So, for masonry arch bridges, the total strain crack model has to be used, while this model was not capable of mimicking the behaviour of just a masonry arch. Hence, the micro modelling approach is preferred. However, the macro models can be used when sufficient tensile properties are used, to avoid unrealistic failure patterns in the arch.

Due to the dominant failure of the soil, a definitive recommendation on which approach best represents masonry arch behaviour is not possible. Next to that, further investigation is needed to determine whether the backfill behaviour is still dominant when the shape of the arch changes. Although it is not possible to make a big statement, this study shows that there are two approaches that could be followed.

It is now possible to address the main question:

What is the role of constitutive models on simulating the behaviour of masonry arch bridges?

The study has shown that the actual behaviour of masonry arch bridges can be modelled in detail, however, the backfill properties seem to be most critical. It was expected that the modelling of the masonry arch would have been critical, as the researchers described the formation of a four hinge mechanism, which also is the most common failure mode for these type of bridges. However, sliding failure of the backfill was the governing failure mode. Due to the load, the arch deforms to the left, creating space for the backfill below the load. In this area, large plastic strains are observed in the backfill and the backfill fails. Although this is the case, poor modelling of the masonry arch itself could lead to changes in results.

When a macro modelling approach is followed, the tensile strength assigned to the masonry material model has to be of a sufficient magnitude. If too low values are used, unrealistic cracks start to appear in the arch and the arch fails. This is due to Poisson's ratio and isotropic nature of the material model, where the tensile strength of the material is the same in all directions. The study showed that this is not the case when a micro modelling approach is followed. All the possible crack planes are modelled with interface elements with a different stiffness in both directions, creating a anisotropic model. The results showed that any variation in tensile strength did not influence the results.

The compressive masonry properties can also influence the behaviour, as was found. Using a lower compressive strength causes the arch to crush at some points, however, this only influences the peak load of the models and did not influence the post peak behaviour or governing failure mode. This post peak behaviour was still governed by sliding failure of the backfill. The study showed that the macro model was less sensitive to a change in compressive strength compared to the micro model, which is opposite to what was found for the tensile strength. Although the compressive strength does influence the results, it influence is limited and only occurs when very low values are used.

Combining the above, it could be said that a micro modelling approach is preferred when modelling masonry arch bridges. This model is good at localizing the cracks and is less sensitive to a change in tensile properties. However, similar results can be found with a macro model. The biggest difference between the two is that, for a macro model, considerably higher values for the tensile strength should be used to avoid unrealistic failure patterns.

Although the micro modelling approach it preferred, this study showed that the behaviour of the backfill is governing the behaviour of the model. Initially the backfill failed locally just below the load, after which linear elastic properties had to be given to this area, to find that the backfill was sliding over the arch and was still governing the behaviour.

In the analysed tests, it was given at what point and under what load a “hinge” was formed. For both tests, a four hinge mechanism was given as the governing failure mechanism, however, the numerical models did not find this mechanism. The by the researchers called “hinges” could also be the first visible crack that was formed, which does not mean that this is a hinge yet. The numerical models show that initially multiple cracks appear and start to grow, to a point where the cracks start to accumulate in one plane and the other cracks are closing. Only in this case, it is clear that a hinge is formed. Comparing test results to the numerical results, a similar force displacement curve is found, while a different failure mechanism is governing. Questions can now be raised about the accuracy of the program, which could lead to higher safety factors or more restrictions, while it could very well be the case that the program was very accurate. Instead of focussing on the formation of a hinge, it would bet more efficient to focus on the crack widths, these eventually reveal when a hinge is formed.

Concludingly, it is not yet possible to make a statement on how masonry arch bridges should be modelled. It is clear that isotropy does influence the behaviour of the arch and that a micro modelling approach is more stable, however, the behaviour of the structure is governed by the behaviour of the backfill. This has not been mentioned in previous literature, where the formation of a four hinge mechanism was governing. More tests need to be performed where not only the masonry arch is analysed, but also the movements in the backfill. Next to that, the in the Salford tests created plane strain conditions do not entirely represent a traffic load. The load for a car for instance, is not applied over the entire width of a bridge, but only below the wheels/axles. The influence of the type of loading needs to be investigated as well.

6.2. Recommendations

The results obtained in this study show that there is still a lot unknown about the behaviour of masonry arch bridges and further research is required to gain this knowledge. The first action needed to do so, is performing a series of tests. This series should contain a test on just a masonry arch, a masonry arch with backfill, a masonry arch with backfill and a subsoil. The results from these test series should not only be focussed on the arch behaviour, as it was found that the backfill is governing for the tests analysed in this study. The series of tests should be performed on arches with different span-to-rise ratios, by doing so, it can be determined whether the backfill actually is governing or for what span-to-rise ratio the masonry arch becomes governing. Prior to the tests, the materials, bricks, mortar, masonry (brick+mortar) and backfill, have to be tested extensively to determine the actual material properties.

The numerical models can now be created, using the obtained material properties, and compared to the test results. In order to make a statement on how the masonry arch should be modelled, it is important to find a test series where the arch is governing the behaviour of the structure. Otherwise the behaviour of the backfill would be dominant and the difference between a isotropic macro material model and an anisotropic micro model would limited, as was found in this study.

Next to the need for well described and reported tests series, it can also be checked whether a three-dimensional numerical model could be used. In such a model, it is possible to apply actual axle loads at realistic locations. Creating a three-dimensional model also introduces new problems, such as the description of the anisotropic materials in three directions. However, it could help understand what is actually happening when a masonry arch bridge is loaded.

Another option that can be investigated is the use of a combination of macro and micro modelling. In the in this study presented micro model, the bricks are modelled as continuum elements that cannot fail. However, crushing can also occur in the bricks and not only in the unit-mortar interface. It might even be more realistic to consider crushing to occur in the units and cracking and shearing to occur in the interfaces.

The above recommendations are important to gain more data and eventually knowledge about the behaviour of masonry arch bridges. However, not only data is needed, engineers need to find a clearer definition of a hinge and when this actually occurs. Mathematically speaking, hinges have a clear definition, but, how can this be determined with the naked eye or what measuring instrument is needed? Engineers and researchers need to find an agreement on the definition of a hinge and how the appearance of a hinge can be determined during a test. In line with the presented study, it would be more effective to focus on crack widths. It is globally known where the hinges are expected to be formed, if the crack widths of these planes are monitored a better hinge formation sequence can be determined.

7. References

Ahmad, S. (2017). *Static Analysis of Masonry Arches.* Salford: University of Salford.

Augusthus-Nelson, L., & Swift, G. (2020, 10). Experimental investigation of the residual behaviour of damaged masonry. *Structures, 27*, pp. 2500-2512.

Augusthus-Nelson, L., Swift, G., Melbourne, C., Smith, C., & Gilbert, M. (2018). Large-scale physical modelling of soil-filled. *International Journal of Phisical modelling in Geotechnics, 18*(2), pp. 81-94.

Basilio Sánchez, I. (2007). *Strengthening of arched masonry.* Guimarães, Portugal: Unitversity of Minho.

Bentley. (2023). 3 - Reference Manual. In *PLAXIS 2D 2023.1* (p. 257). Delft: Bentley.

Block, P., DeJong, M., & Ochsendorf, J. (2006). As Hangs the Flexible Line: Equilibrium of Masonry Arches. *Nexus Network Journal, 8*(2), pp. 13-24.

Brinkgreve, R. B. (2005). Selection of soil models and parameters for geotechnical engineering application. *Soil Constitutive Models* (pp. 69-98). Reston, Virginia: American Societyof Civil Engineers.

Callaway, P., Gilbert, M., & Smith, C. C. (2012). Ifnluence of backfill on the capacity of masonry arch bridges. *Bridge Engineering*, 147-158.

Casas, J. R. (2011, 4 1). Reliability-based assessment of masonry arch bridges. *Construction and Building Materials, 25*(4), pp. 1621-1631.

CUR. (1994). *Structural masonry: an experimental/numerical basis for practical design.* Gouda: CUR.

DIANA FEA. (2022). Combined Cracking-Shearing-Crushing. In D. Ferreire, & J. Manie, *DIANA - Finite Element Analysis.* Delft: DIANE FEA BV.

DIANA FEA. (2022). Discrete Cracking. In D. Ferreira, & J. Manie, *DIANA- Finite Element Analysis.* Delft: DIANA FEA BV.

DIANA FEA. (2022). Engineering Masonry Model. In D. Ferreira, & J. Manie, *DIANA - Finite Element Analysis.* Delft: DIANA FEA BV.

DIANA FEA. (2022). Hardening Soil Model/Modified Mohr-Coulomb Engineering Input. In D. Ferreira, & J. Manie, *DIANA - Finite Element Analysis* (pp. -). Delft: DIANA FEA BV.

DIANA FEA. (2022). Mohr-Coulomb Plasticity. In D. Ferreira, & J. Manie, *DIANA - Finite Element Analysis* (pp. -). Delft: DIANA FEA BV.

DIANA FEA. (2022). Plane Strain Elements. In D. Ferreira, & J. Manie, *DIANA - Finite Element Analysis.* Delft: DIANA FEA BV.

DIANA FEA. (2022). Plane Stress Elements. In D. Ferreira, & J. Manie, *DIANA - Finite Element Analysis.* Delft: DIANA FEA BV.

DIANA FEA. (2022). Structural Interface Elements. In D. Ferreira, & J. Manie, *DIANA - Finite Element Analysis.* Delft: DIANA FEA BV.

DIANA FEA. (2022). Total Strain Crack Models. In D. Ferreira, & J. Manie, *DIANA- Finite Element Analysis.* Delft: DIANA FEA BV.

Duncan, J., & Chang, C. (1970, 9 1). Nonlinear analysis of stress and strain in soils. *Journal of the Soil Mechanics and Foundations Division, 96*(5), 1629-1653.

Esposito, R., Hendriks, M., & Rots, J. (2022, 12 1). *Computational modelling of structures [Powerpoints].* Retrieved from Brightspace: https://brightspace.tudelft.nl/d2l/le/content/399435/Home

Goldscheider, M. (1984). True triaxial tests on dens sands. In G. Gudehus, F. Darve, & I. Vardoulakis, *Constitutive relations for soils* (pp. 11-54). Rotterdam: Balkema.

Heyman, J. (1966, 4 1). The stone skeleton. *International Journal of Solids and Structures, 2*(2), pp. 249-256.

Hooke, R. (1676). *A description of helioscopes, and some other instruments.* London, UK: T.R.

Janbu, N. (1963). Soil compressibility as determined by oedometer and triaxial tests. *Proceedings of the 3rd European Conference on Soil Mechanics and Foundation Engineering* (pp. 19-25). Wiesbaden: Deutsche Gesellschaft für Erd- und Grundbau.

Liberatore, D., Marotta, A., & Sorrentino, L. (2014). Estimation of clay-brick unreinforced masonry compressive. *9th International masonry conference* (pp. 5-7). Quimarães, Portugal: International Masonry Society.

LimitState. (2020, 2 1). *Ring Documentation.* Retrieved from LimitState: https://www.limitstate.com/ring-documentation

Liu, B., Feng, X., & Zhang, S.-M. (2009, 10). The effective Young's modulus of composites beyond the Voigt estimation. *Composites Science and Technology, 69*(13), pp. 2198-2204.

Loarenço, P. (1996). *Computational strategies for masonry structures.* Delft: Delft University Press.

Lourenço, P. (1994). *ANALYSIS OF MASONRY STRUCTURES: Theory and application.* Delft: TNO Building and Construction Research.

Lourenço, P., Rots, J., & Blaauwendraad, J. (1995). Two approaches for the analysis of. *HERON, 40*, pp. 313-340.

McNary, W. S., & Abrams, D. P. (1985, 4 4). Mechanica of Masonry in Compression. *Journal of Structural Engineering, 111*(4), pp. 857-870.

Ohde, J. (1939). Zur theorie der druckverteilung im baugrund. *Der Bauingenieur, 20*, 451-459.

Pippard, A., & Ashby, R. (1939). An Experimental Study of the Voussoir Arch. *Journal of the Intitution of Civil Engineers, 10*(3), pp. 383-404.

Pluijm, R. v. (1992). Material properties of masonry and its components under tension and shear. *Proceedings 6th Canadian Masonry Symposium* (pp. 675-686). Saskatoon, Canada: University os Saskatchewan.

Pluijm, R. v. (1993). Shear behaviour of bed joints. In A. A. Hamid, & H. G. Harris (Ed.), *6th North American Masonry Conference* (pp. 125-136). Philadelphia, Pennsylvania, USA: Technomic Publ. Co.

Rota, M., Bolognini, D., Pecker, A., & Pinho, R. (2005). A methodology for seismic vulnerability of masonry arch bridge walls. *Journal of Earthquake Engineering*, 331-353.

Schanz, T., Vermeer, P., & Bonnier, P. (1999). The hardening soil model: Formulation and verification. In R. B. Brinkgreve, *Beyond 2000 in Computational Geotechnics* (pp. 281-296). London: Routledge.

Stichting Koninklijk Nederlands Normalisatie Instituut. (2020). *NPR 9998:2020.* Delft: Stichting Koninklijk Nederlands Normalisatie Instituut www.nen.nl.

Turnšek, V., & Čačovič, F. (1971). Some experimental results on the strength of brick masonry walls. *2nd International Brick Masonry Conference* (pp. 149-156). Stoke-on-Trent: British Ceramic Research Association.

Witteveen+Bos Raadgevende ingenieurs B.V. (2019, October 10). Deelopdracht 02 - KW1116 Welfbrug Nieuwstraat - Onderzoek Constructieve veiligheid - Fase 2: Vooronderzoek Validatie VK proeven.

Zampieri, P., Cavalagli, N., Gusella, V., & Pellegrino, C. (2018). Collapse displacements of masonry arch with geometrical incertainties on spreading supports. *Computers & Structures, 208*, pp. 118-129.

Appendix A. Macro model variations Salford test (full MC)

In the figures below, the results of the parametric study for the model presented in Section 5.4.1.1 are given. This study was performed to determine whether the local failure of the backfill just below the point load, was actually the occurring failure mode. To be able to determine this, multiple variations in masonry and soil properties were performed.

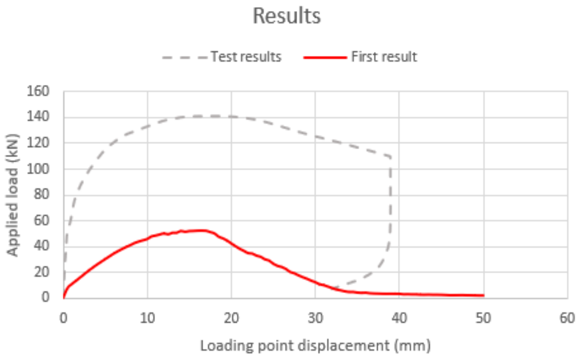

Figure A.1: First results, Salford test

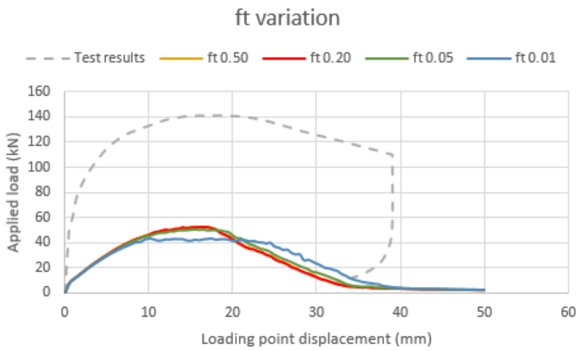

Figure A.2: Tensile strength variation, Salford test

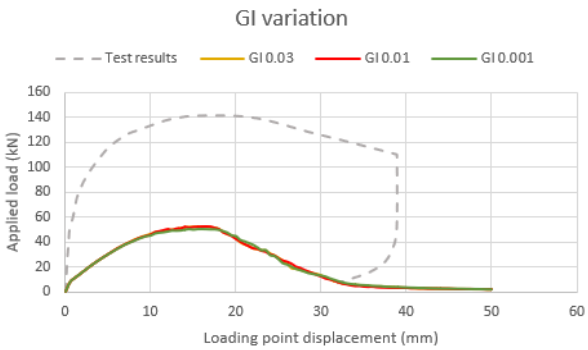

Figure A.3: Tensile fracture energy variation, Salford test

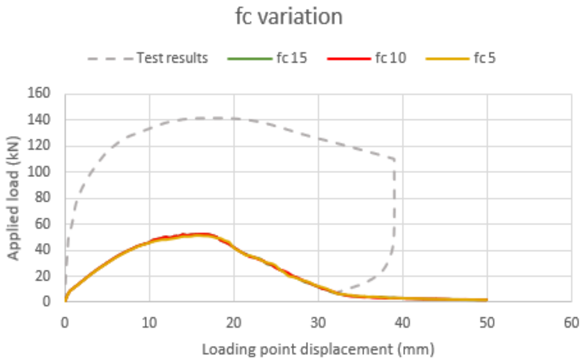

Figure A.4: Compressive strength variation, Salford test

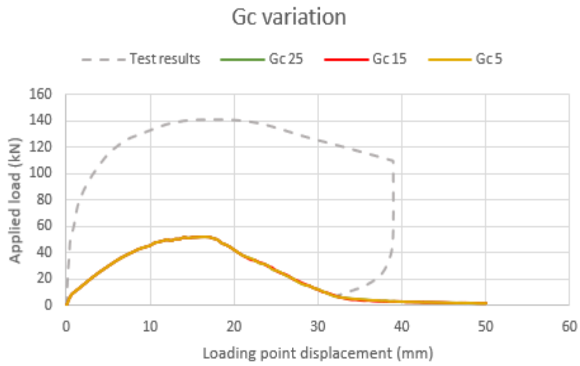

Figure A.5: Compressive fracture energy variation, Salford test

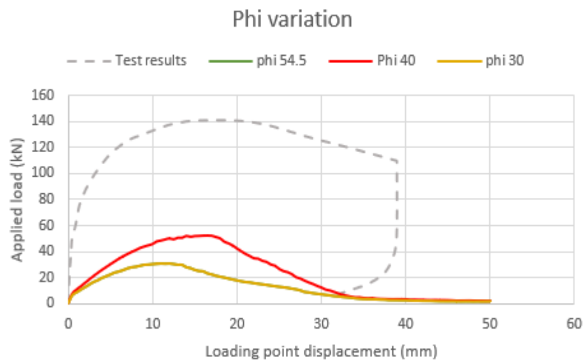

Figure A.6: friction angle variation, Salford test

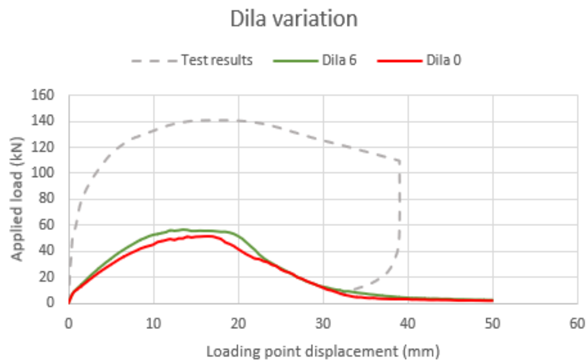

Figure A.7: Dilatation angle variation, Salford test

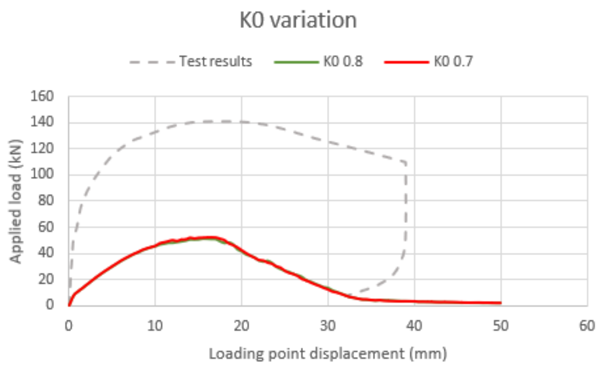

Figure A.8: Initial stiffness variation, Salford test

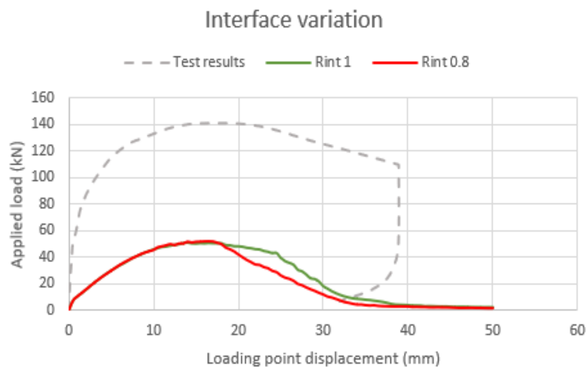

Figure A.9: Soil-structure interface variation, Salford test

Appendix B. Adapted macro model variations Salford test (MC)

The parametric study performed on the adapted Salford geometry are presented in the following figures. The study was performed for three different values of the Young's modulus for the backfill, starting with $E = 20.83\ MPa$, followed by $E = 40\ MPa$ and $E = 80\ MPa$.

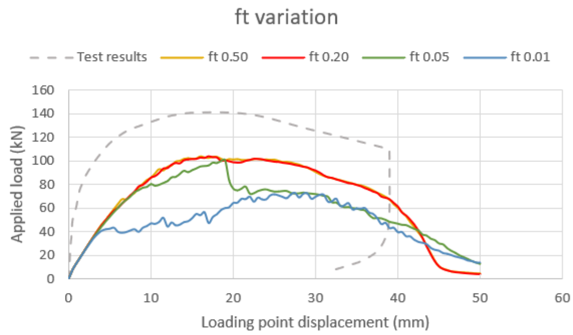

Figure B.1: ft variation, E20

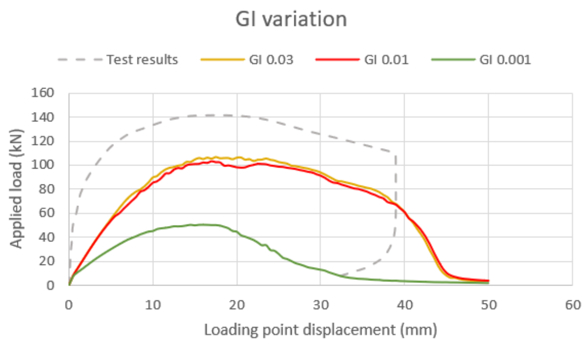

Figure B.2: GI variation E20

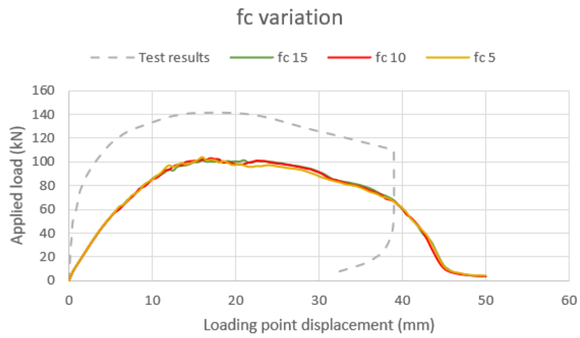

Figure B.3: fc variation, E20

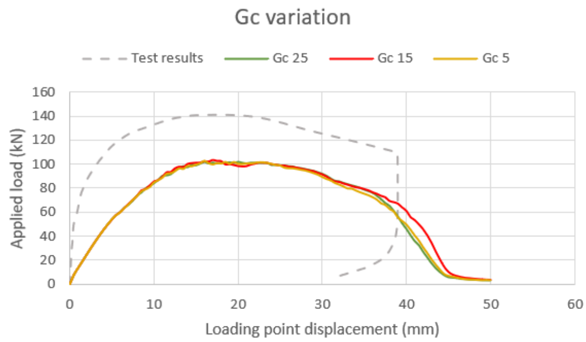

Figure B.4: GI variation, E20

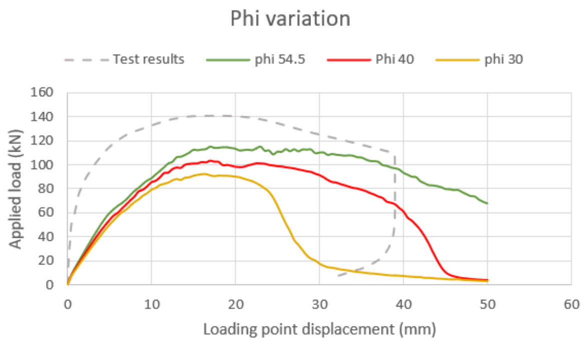

Figure B.5: Phi variation, E20

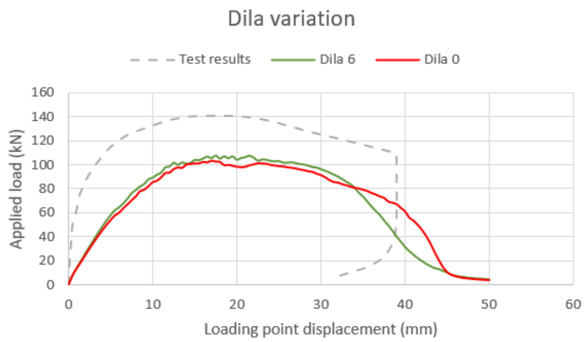

Figure B.6: Dilatation variation, E20

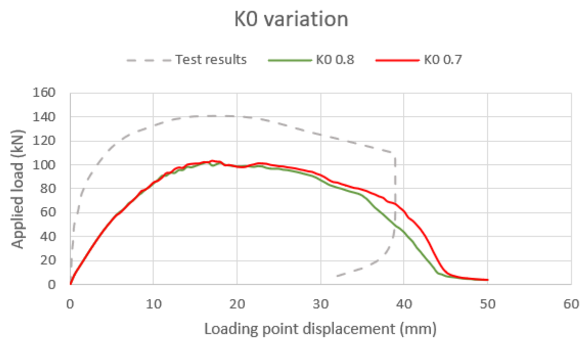

Figure B.7: K0 variation, E20

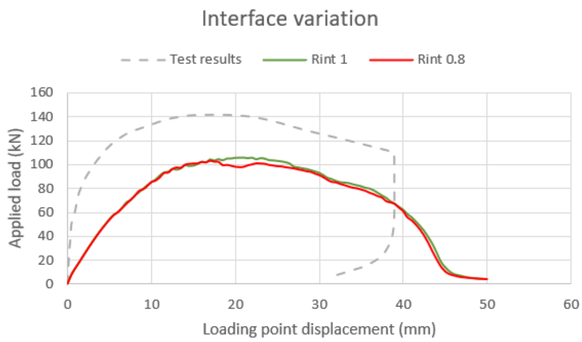

Figure B.8: Interface variation, E20

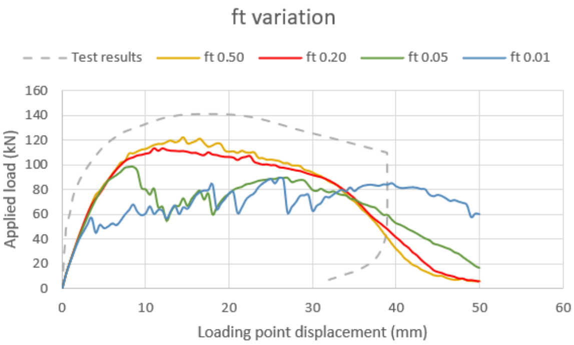

Figure B.9: ft variation, E40

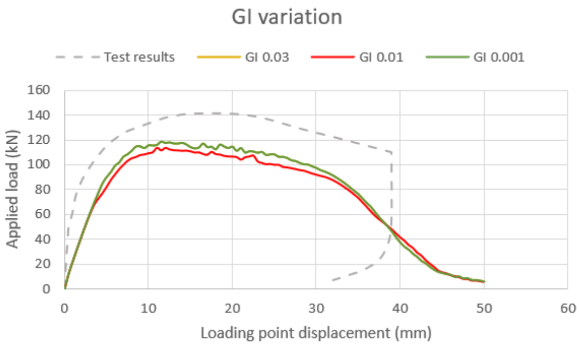

Figure B.10: GI variation, E40

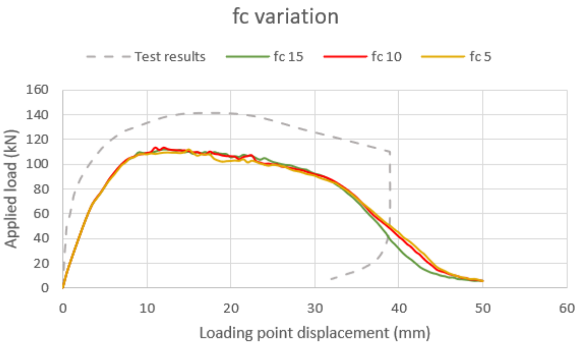

Figure B.11: fc variation, E40

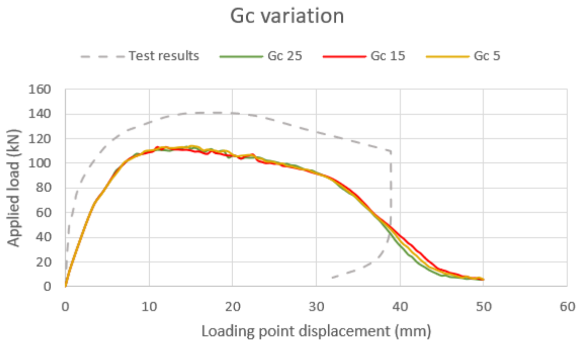

Figure B.12: Gc variation, E40

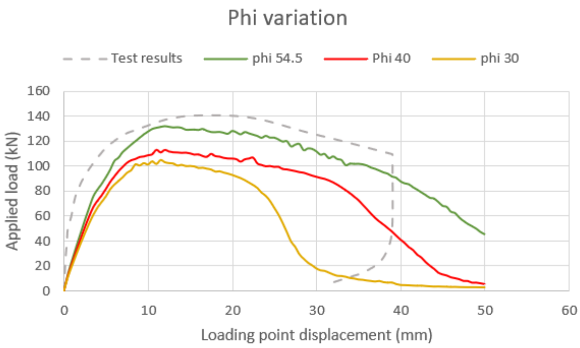

Figure B.13: Phi variation, E40

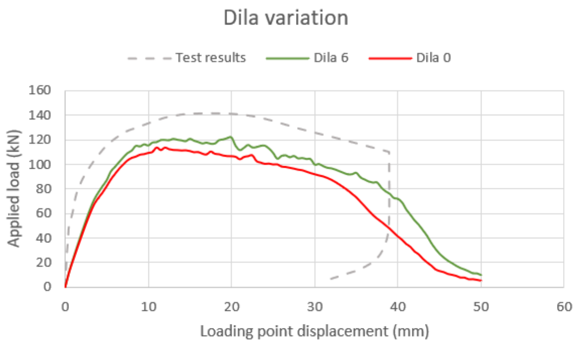

Figure B.14: Dilatation variation, E40

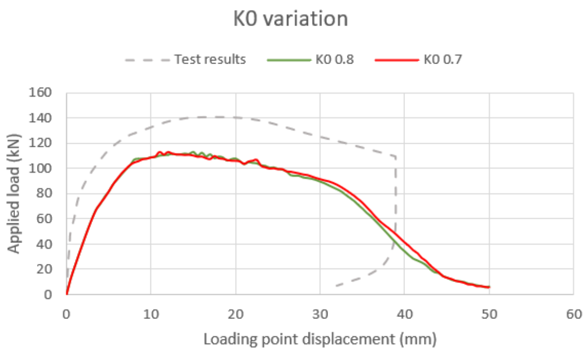

Figure B.15: K0 variation, E40

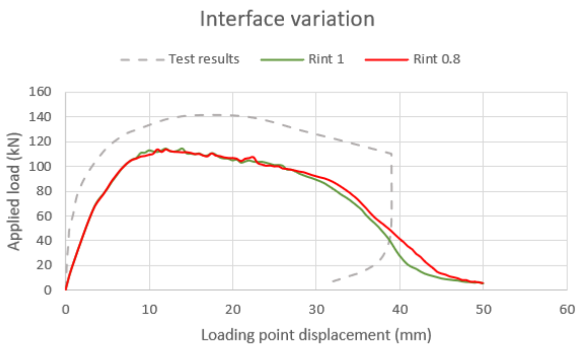

Figure B.16: Interface variation, E40

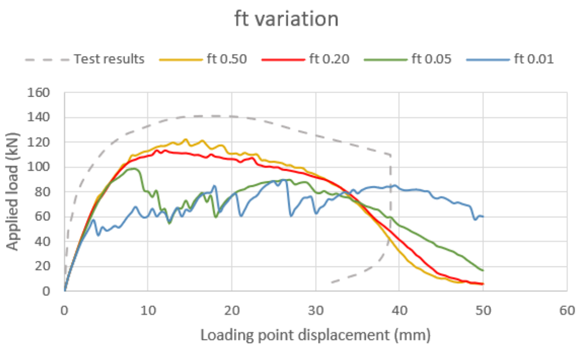

Figure B.17: ft variation, E80

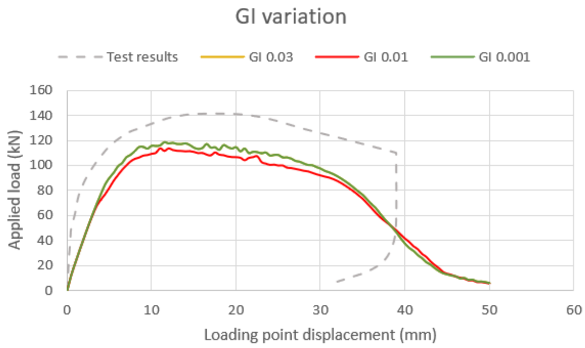

Figure B.18: GI variation, E80

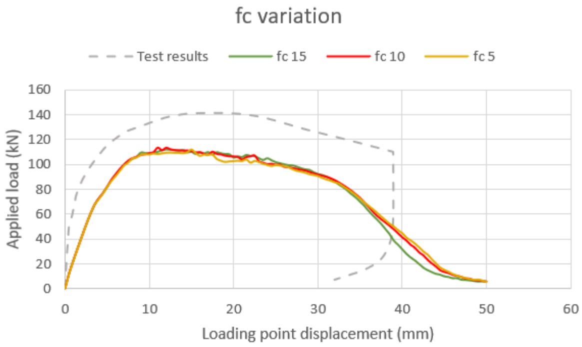

Figure B.19: fc variation, E80

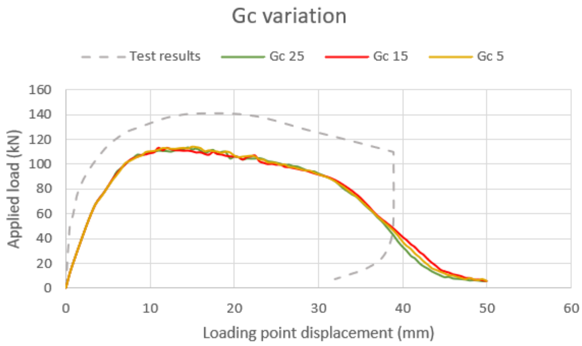

Figure B.20: Gc variation, E80

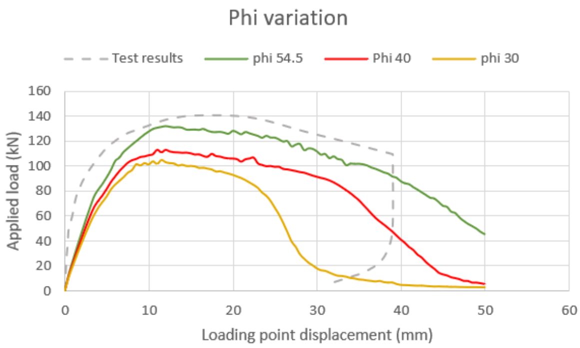

Figure B.21: Phi variation, E80

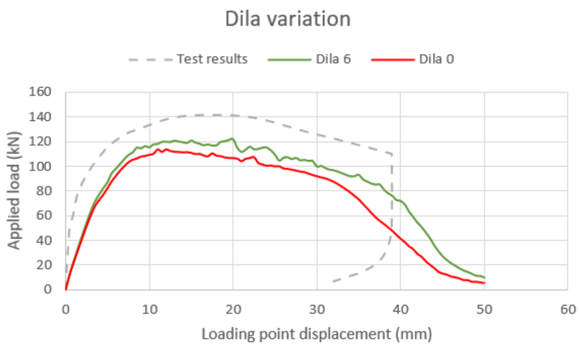

Figure B.22: Dilatation variation, E80

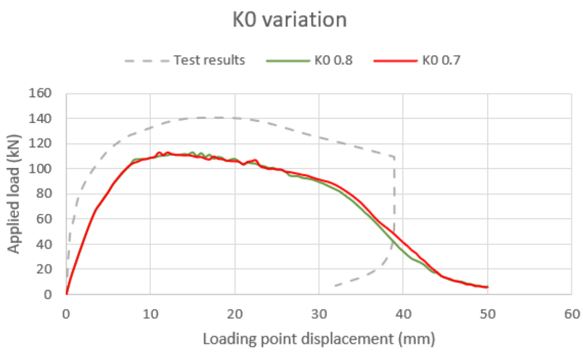

Figure B.23: K0 variation, E80

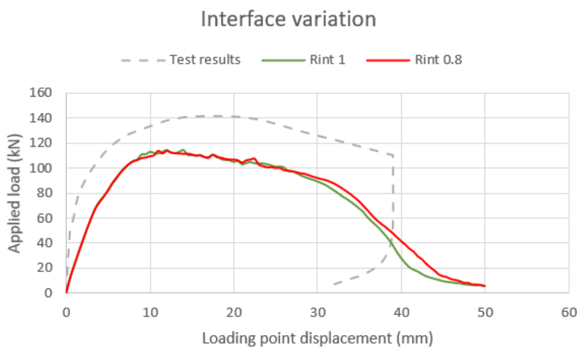

Figure B.24: Interface variation, E80

Appendix C. Hardening soil model variations, Salford test

In the figures below the resulting force-displacement curves of the parametric study performed on the model presented in Section 5.4.1.10 are given.

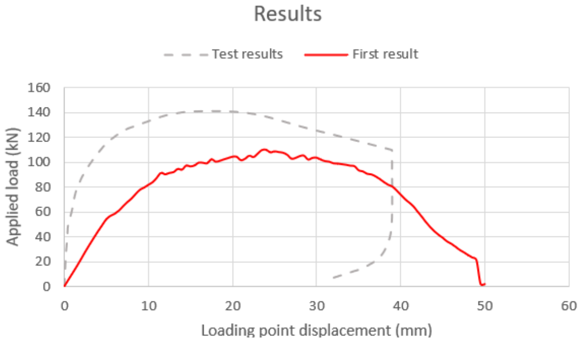

Figure C.1: First results, hardening soil model

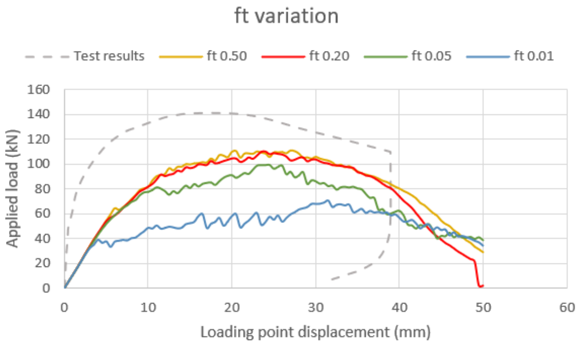

Figure C.2: ft variation HS model

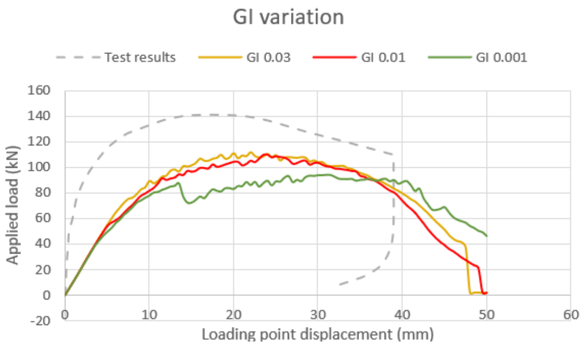

Figure C.3: Gl variation, HS model

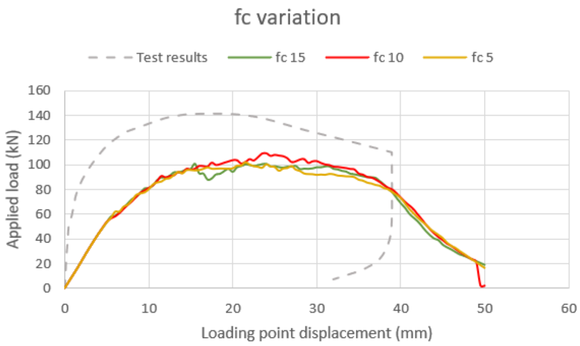

Figure C.4: fc variation, HS model

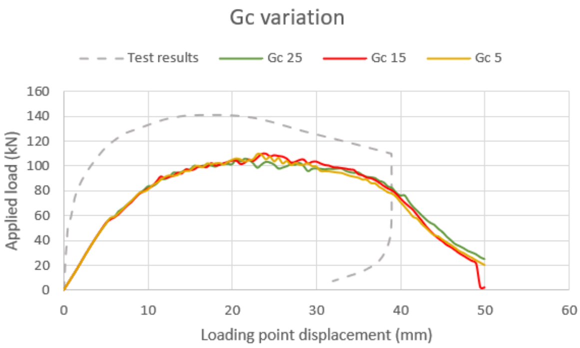

Figure C.5: Gc variation, HS model

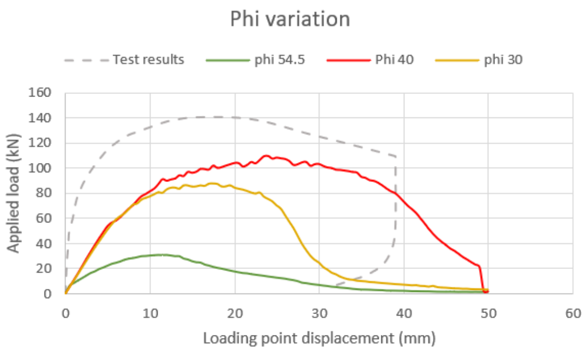

Figure C.6: Phi variation, HS model

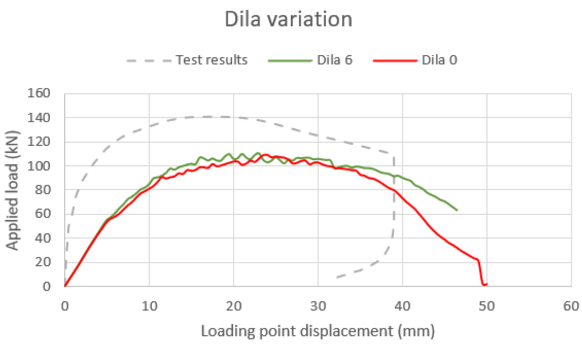

Figure C.7: Dilatation variation, HS model

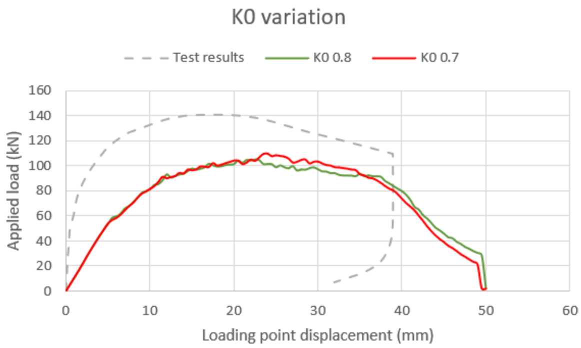

Figure C.8: K0 variation, HS model

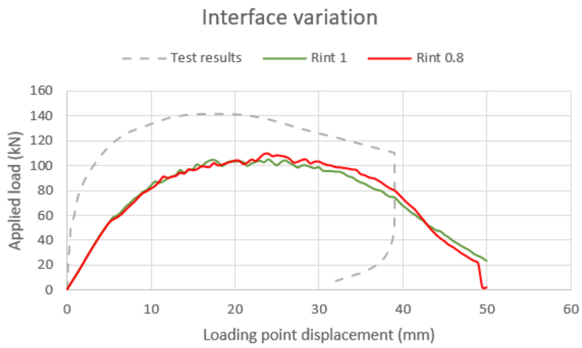

Figure C.9: Interface variation, HS model

Appendix D. MC vs HS Full comparison, Salford test

In the following figure a full comparison of the Salford test modelled with the Mohr-Coulomb and Hardening soil is shown.

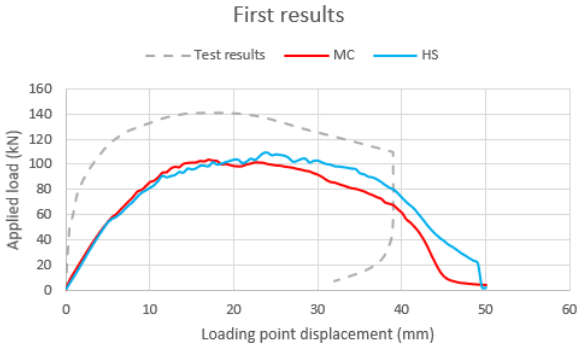

Figure D.1: MC vs HS, first results

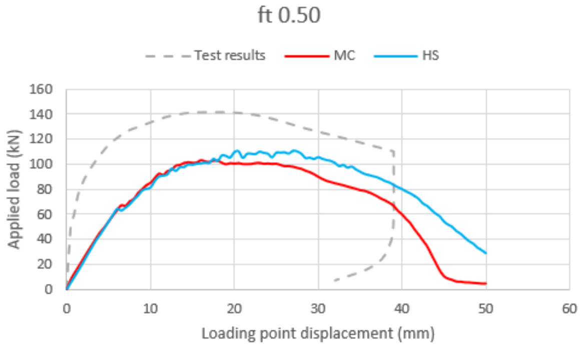

Figure D.2: MC vs HS, ft 0.50

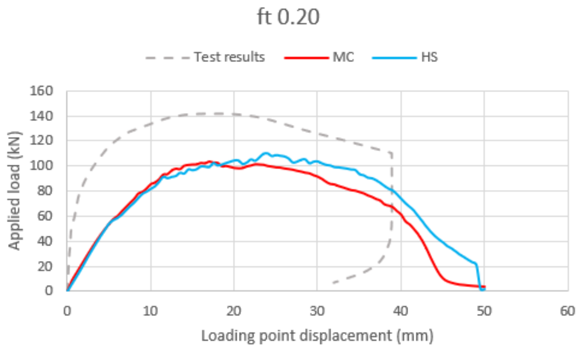

Figure D.3: MC vs HS, ft 0.20

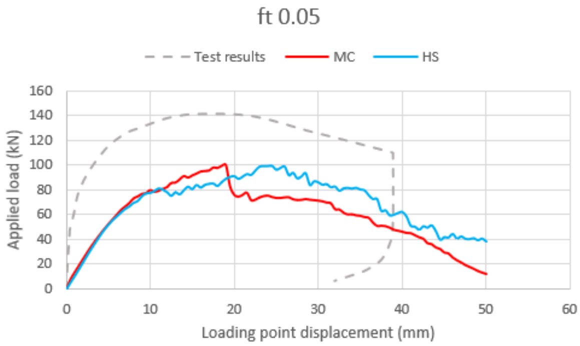

Figure D.4: MC vs HS, ft 0.05

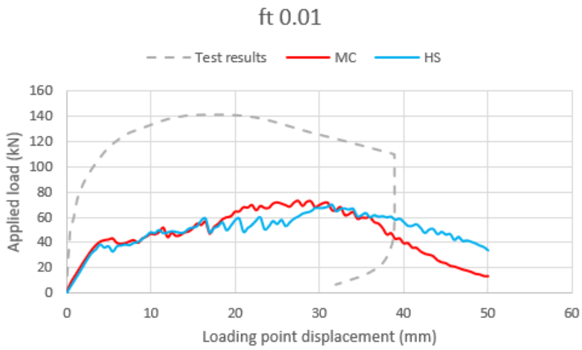

Figure D.5: MC vs HS, ft 0.01

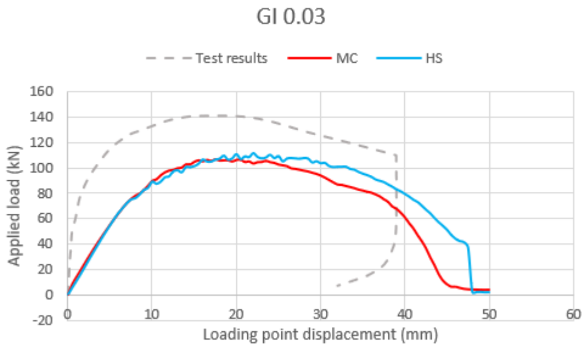

Figure D.6: MC vs HS, GI 0.03

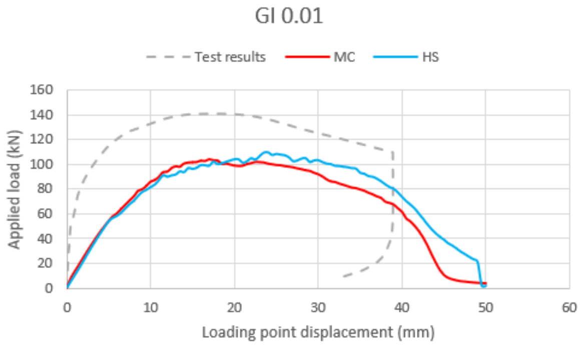

Figure D.7: MC vs HS, GI 0.01

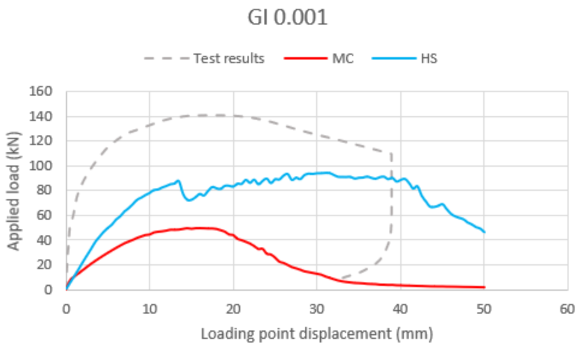

Figure D.8: MC vs HS, GI 0.001

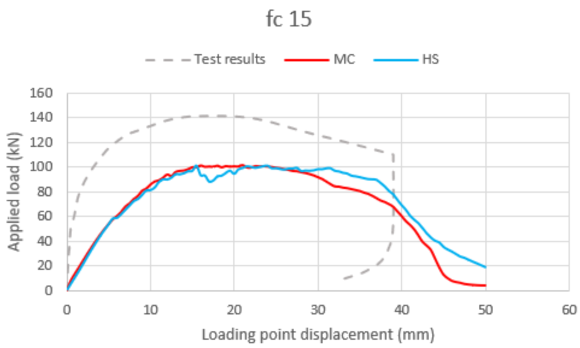

Figure D.9: MC vs HS, fc 15

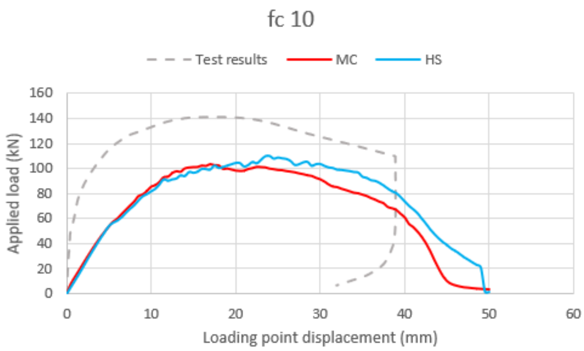

Figure D.10: MC vs HS, fc 10

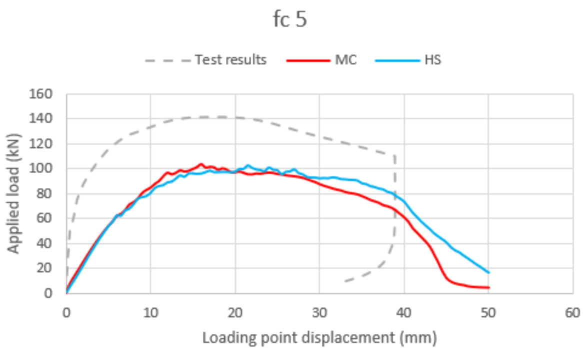

Figure D.11: MC vs HS, fc 5

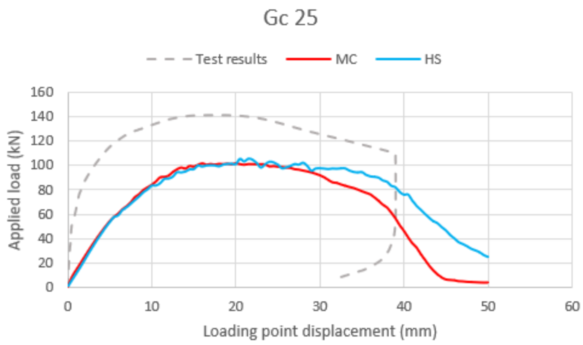

Figure D.12: MC vs HS, Gc 25

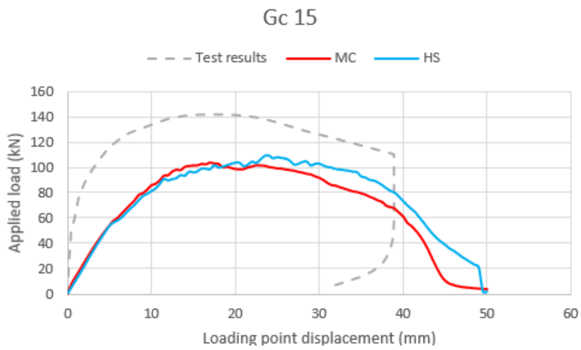

Figure D.13: MC vs HS, Gc 15

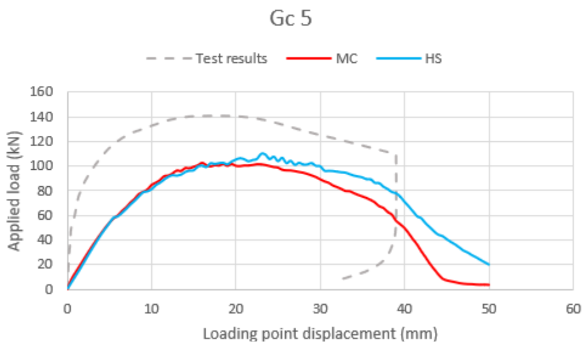

Figure D.14: MC vs HS, Gc 5

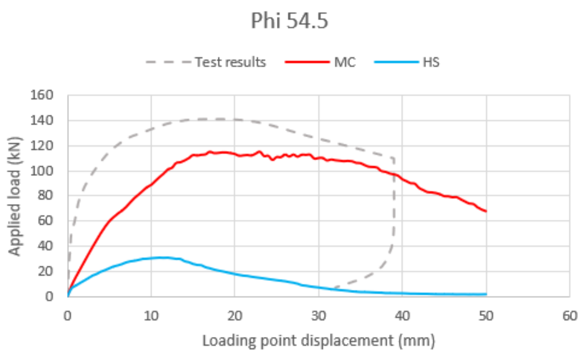

Figure D.15: MC vs HS, Phi 54.5

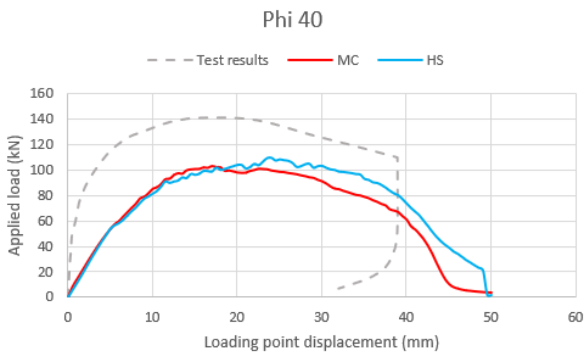

Figure D.16: MC vs HS, Phi 40

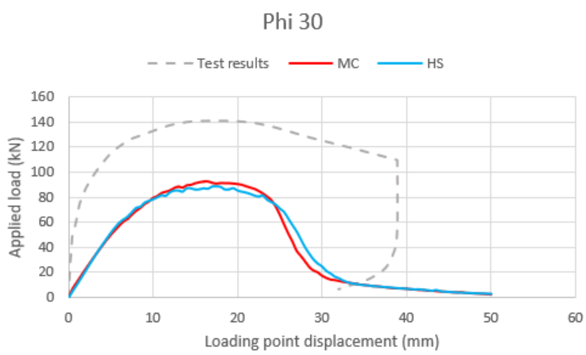

Figure D.17: MC vs HS, Phi 30

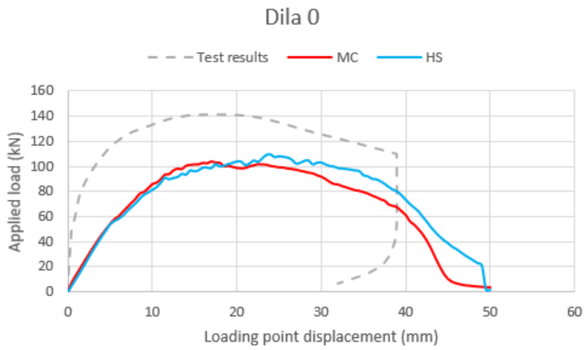

Figure D.18: MC vs HS, Dila 0

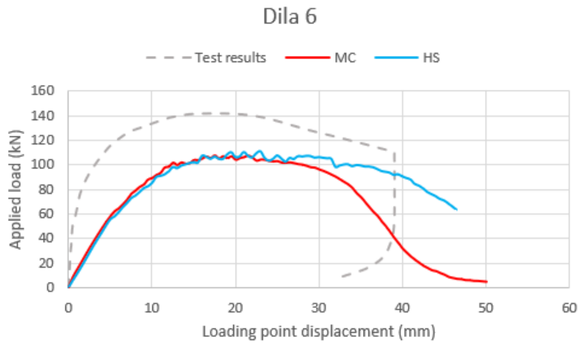

Figure D.19: MC vs HS, Dila 6

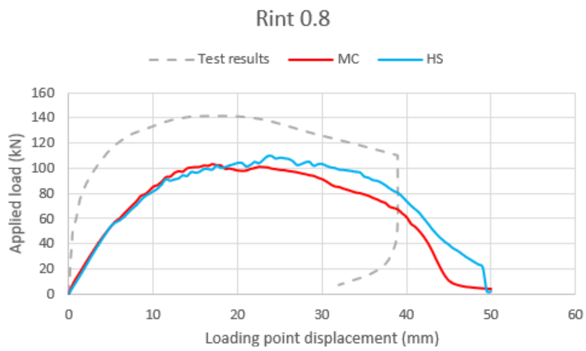

Figure D.20: MC vs HS, Rint 0.8

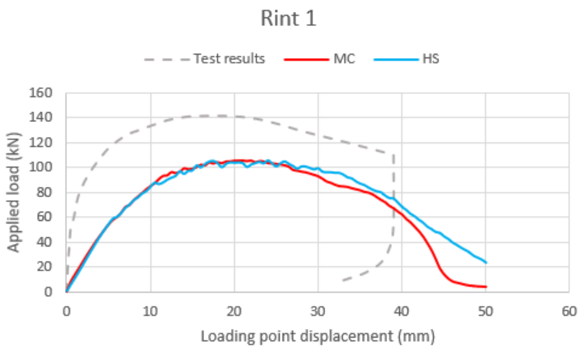

Figure D.21: MC vs HS, Rint 1

Appendix E. Micro model variations, Salford test

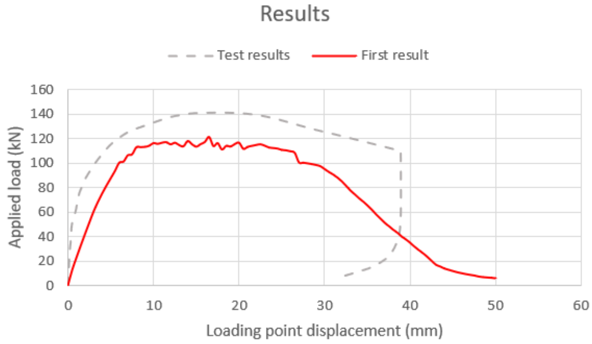

Figure E.1: First results, Salford test

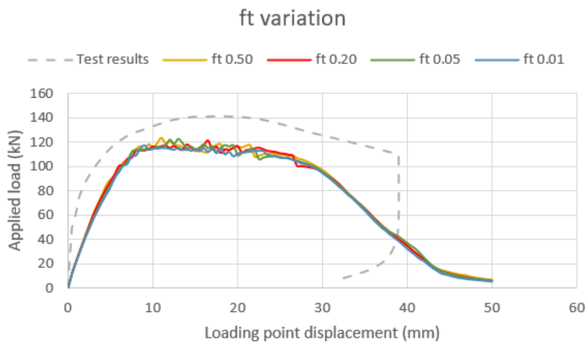

Figure E.2: Tensile strength variation, Salford test

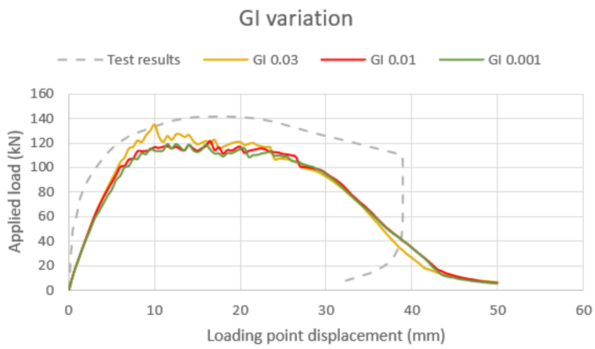

Figure E.3: Tensile fracture energy variation, Salford test

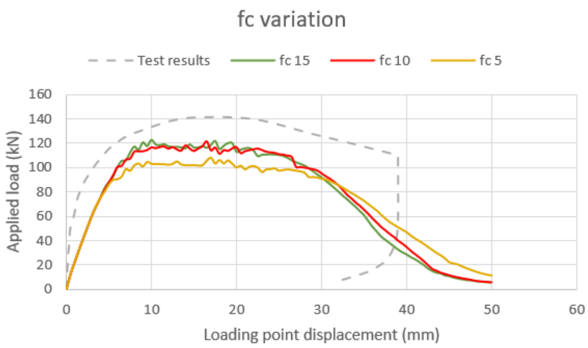

Figure E.4: Compressive strength variation, Salford test

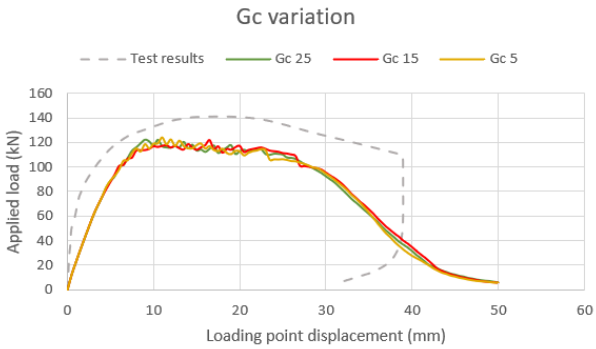

Figure E.5: Compressive fracture energy variation

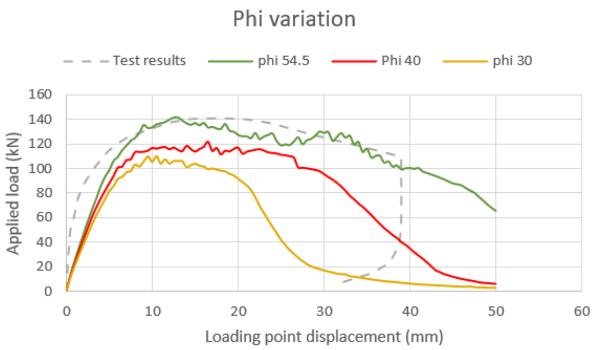

Figure E.6: Friction angle variation, Salford test

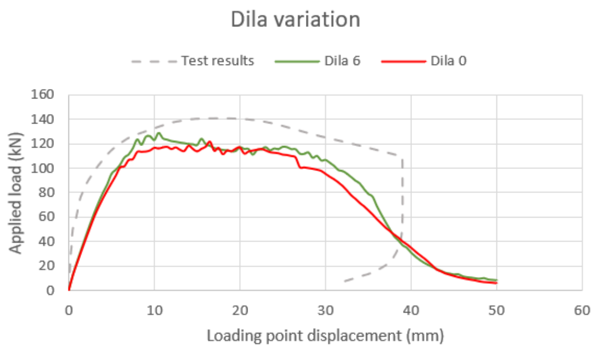

Figure E.7: Dilatancy variation, Salford test

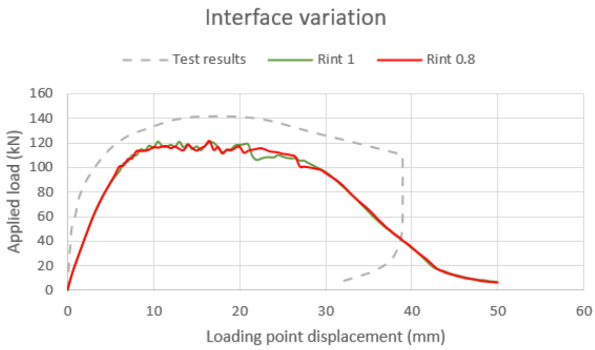

Figure E.8: Soil-structure interface variation

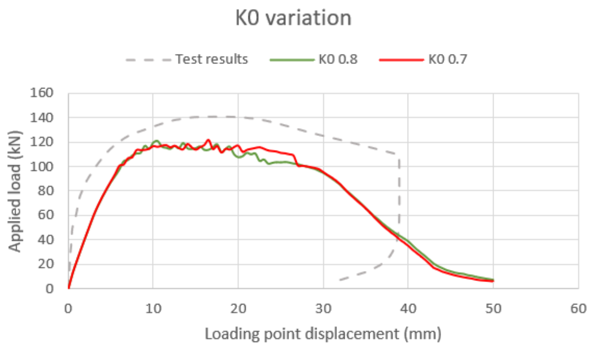

Figure E.9: K0 variation, Salford test

Appendix F. Micro vs. Macro, Salford test

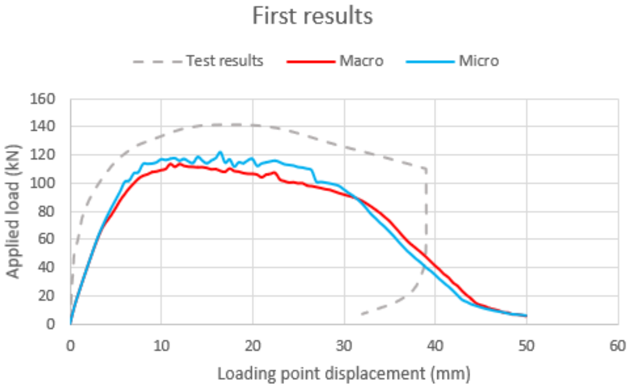

Figure F.1: Micro vs Macro, first results

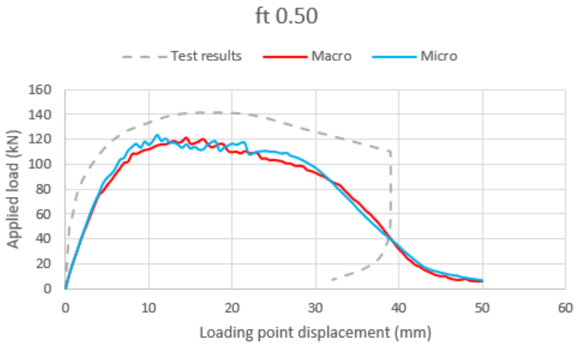

Figure F.2: Micro vs Macro, ft 0.50

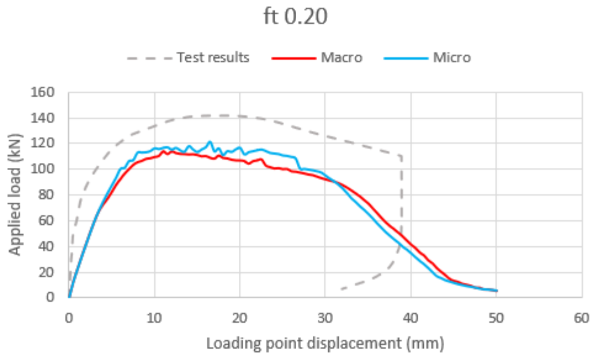

Figure F.3: Micro vs Macro, ft 0.20

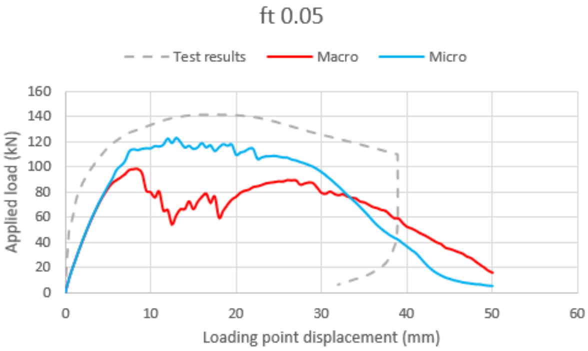

Figure F.4: Micro vs Macro, ft 0.05

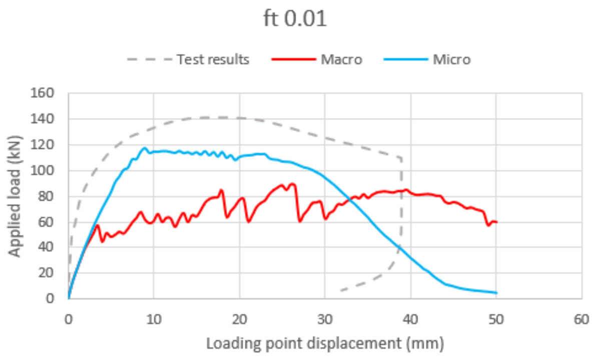

Figure F.5: Micro vs Macro, ft 0.01

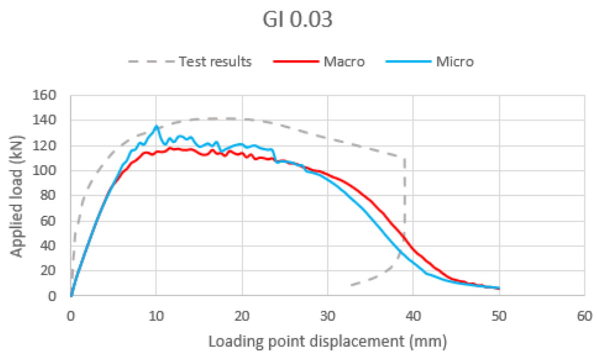

Figure F.6: Micro vs Macro, G^I 0.03

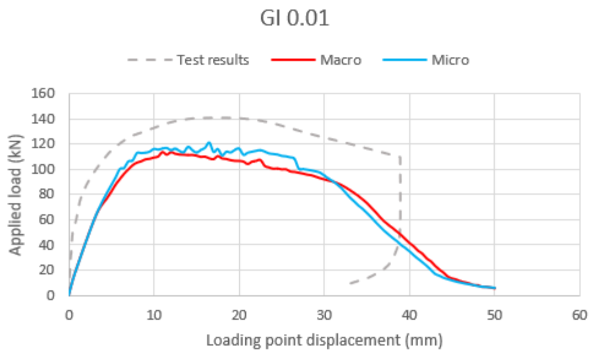

Figure F.7: Micro vs Macro, G^I 0.01

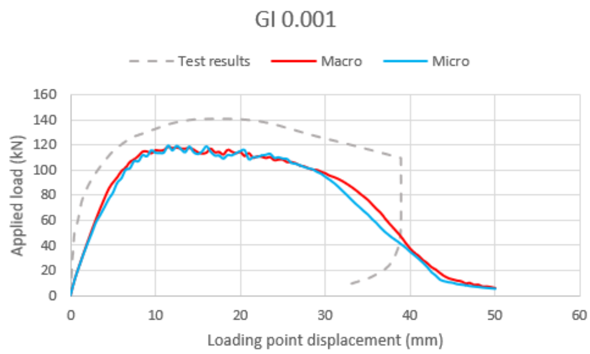

Figure F.8: Micro vs Macro, G^I 0.001

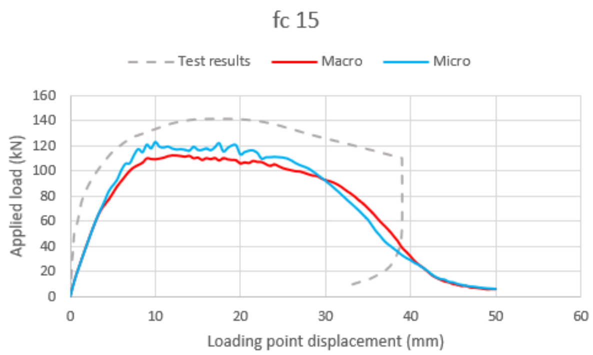

Figure F.9: Micro vs Macro, fc 15

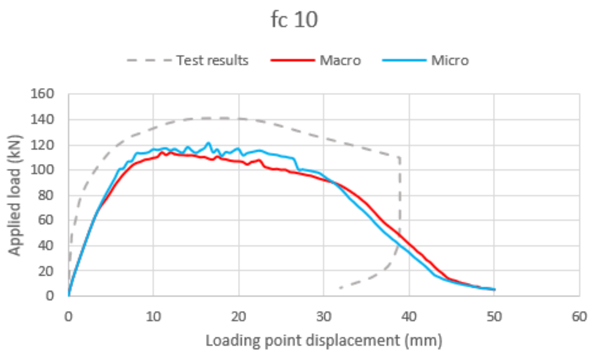

Figure F.10: Micro vs Macro, fc 10

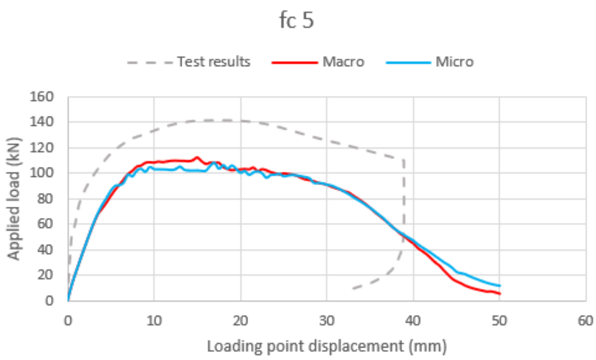

Figure F.11: Micro vs Macro, fc 5

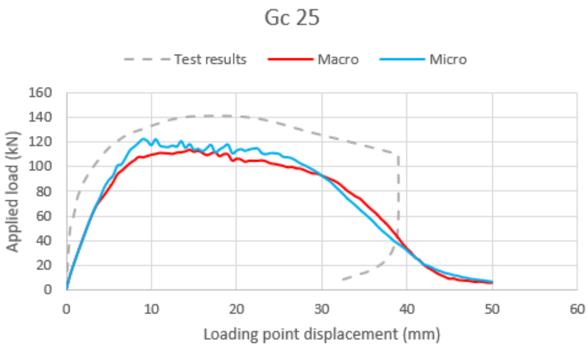

Figure F.12: Micro vs Macro, Gc 25

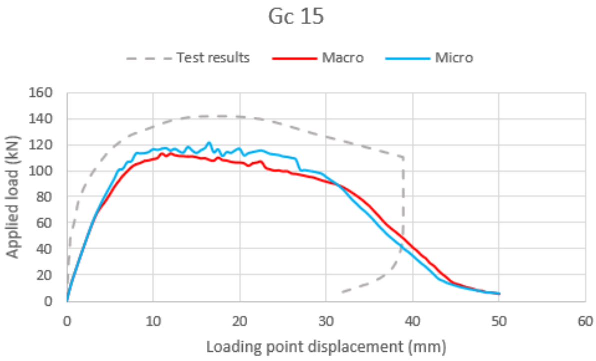

Figure F.13: Micro vs Macro Gc 15

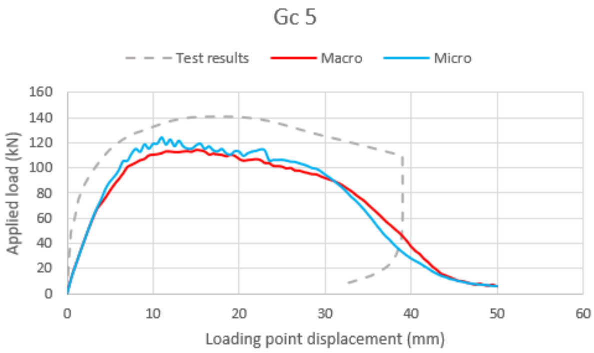

Figure F.14: Micro vs Macro, Gc 5

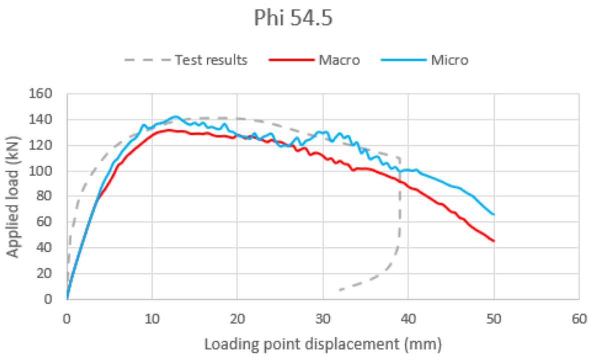

Figure F.15: Micro vs Macro, Friction angle 54.5

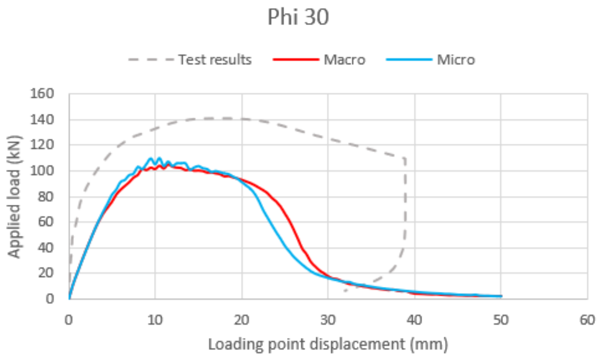

Figure F.16: Micro vs Macro, Friction angle 30

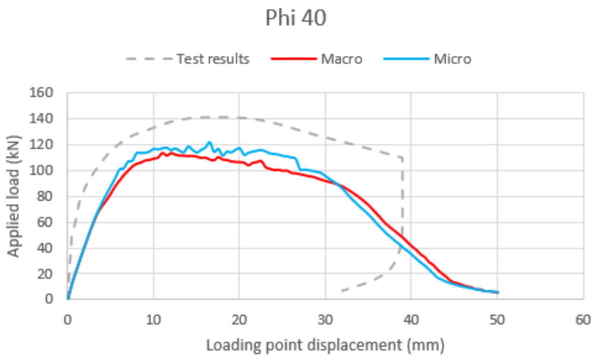

Figure F.17: Micro vs Macro, Friction angle 40

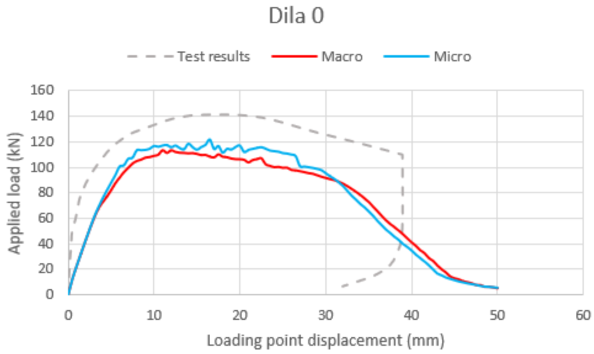

Figure F.18: Micro vs Macro, Dilatancy 0

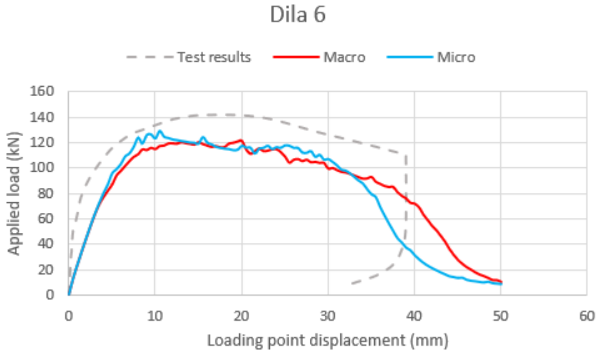

Figure F.19: Micro vs Macro, Dilatancy 6

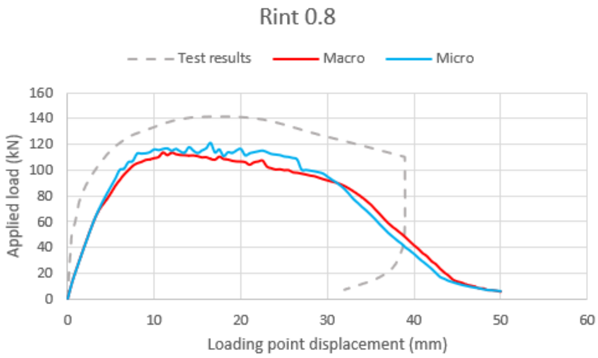

Figure F.20: Micro vs Marco, soil structure interface 0.8

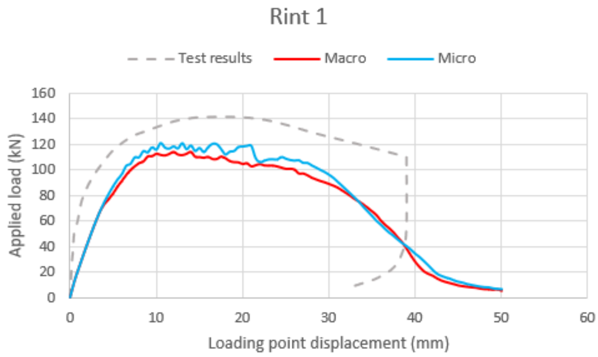

Figure F.21: Micro vs Marco, Soil-Structure interface 1.0